ENGINEERING RESIDUAL STRESS INTO THE WORKPIECE

THROUGH

THE DESIGN OF MACHINING PROCESS PARAMETERS

A Dissertation
Presented to
The Academic Faculty

by

Carl R. Hanna

In Partial Fulfillment
of the Requirements for the Degree
of Doctor of Philosophy in the
George W. Woodruff School of Mechanical Engineering

Georgia Institute of Technology
December 2007

ENGINEERING RESIDUAL STRESS INTO THE WORKPIECE

THROUGH

THE DESIGN OF MACHINING PROCESS PARAMETERS

Approved by:

Dr. Steven Y. Liang, Co-Advisor
George W. Woodruff School of Mechanical Engineering
Georgia Institute of Technology

Dr. Richard W. Neu
George W. Woodruff School of Mechanical Engineering
Georgia Institute of Technology

Dr. Ru-Min Chao, Co-Advisor
Department of System and Naval Mechatronics Engineering
National Cheng Kung University, Tainan, Taiwan, ROC

Dr. Hamid Garmestani
School of Materials Science & Engineering
Georgia Institute of Technology

Dr. Shreyes Melkote
George W. Woodruff School of Mechanical Engineering
Georgia Institute of Technology

Dr. Paul Griffin
School of Industrial & Systems Engineering
Georgia Institute of Technology

Date Approved: July 16, 2007

ACKNOWLEDGEMENTS

I would like to thank the people and sponsors who made this research possible. First, I would like to thank Professor Steven Liang for giving me the opportunity to be part of this research effort, and also would like to thank him for his guidance and support. Further, I would like extend my gratitude to Dr. Ru-Min Chao for his support and advice. I would also like to thank the members of my committee, Professors Shreyes Melkote, Richard Neu, Hamid Garmestani, and Paul Griffin.

Appreciations are due to Morris M. Bryan, Jr. Professorship and Metal Industries Research and Development Center of Taiwan for the financial support during the period of the dissertation study. I also want to thank the Precision Machining Research Consortium (PMRC) support staff who has been very helpful since the first day I joined the group. I would like to thank both my past and present officemates for their friendships. I would like to thank also Dr. Jeffrey Donnell for proofreading all the documents I ever gave him throughout my 8 years at Georgia Tech.

I would like to thank all my friends here and abroad for their support. Last but not least, I want to thank my family, my mother, my father and my sister for their continuous support and encouragement throughout my stay at Georgia Tech.

TABLE OF CONTENTS

LIST OF TABLES

LIST OF FIGURES

LIST OF SYMBOLS

t	Uncut chip thickness or depth of cut
t_c	Chip thickness
w	Width of cut
F_C, F_T	Chip formation force in cut direction and thrust direction
F_R	Cutting force due to oblique angle
k_{AB}	Flow stress of material in shear zone
f	Shear angle
a	Tool rake angle
l	Friction angle in chip formation model
A, B, C, m, n	Johnson-Cook flow stress parameters
e_{AB}, $\dot{e}_{AB}$	Strain and strain rate in the shear zone
e_{int}, $\dot{e}_{int}$	Strain and strain rate between tool and chip
C_{Oxley}	Constant in Oxley's cutting force model
P_{cut}, P_{thrust}	Plowing force in cut direction and thrust direction
q_{shear}, $q_{rubbing}$	Heat intensities from shear zone and rubbing
q_{cool}	Heat loss intensity due to coolant
k_t, r_t, C_t	Thermal conductivity, density, and specific heat
V_{cut}	Cutting speed
$\bar{h}$	Overall heat transfer coefficient
S_{ij}	Deviatoric stresses
a_{ij}	Back stresses
R	Uniaxial yield stress of material
$\dot{e}_{ij}^{p}$	Plastic strain rate
n_{ij}	Direction of plastic strain rate
Y	Blending function used in rolling contact algorithm
k	Rolling contact algorithm constant
G	Elastic shear modulus
r	Corner radius or nose radius

r_e	Edge radius
$d_{c_{avg}}$	Average depth of cut given by the model
s_{ij}^{*}	Total Hertzian stress or elastic stress
$s_{ij}^{*,sharp}$	Herztian stress due to sharp tool condtions
$s_{ij}^{*,plow}$	Hertzian stress due to the roundness of the tool edge
F_c	Total force in the cut direction
F_t	Total force in the thrust direction

SUMMARY

The surface integrity of a machined component that meets the demands of a specific application requirement is defined by several characteristics. The residual stress profile into the component is often considered as the critical characteristics as it carries a direct effect on the fatigue life of a machined component.

A significant amount of effort has been dedicated by researchers to predict post process stress in a workpiece using analytical, experimental, and numerical modeling methods. Nonetheless, no methodology is available that can express the cutting process parameters and tool geometry parameters as functions of machined residual stress profile to allow process planning in achieving desired residual stress profile.

This research seeks to fill that void by developing a novel approach to enable the extraction of cutting process and tool geometry parameters from a desired or required residual stress profile. More specifically, the model consists in determining the depth of cut, the tool edge radius and the cutting forces needed to obtain a prescribed residual stress profile for an orthogonal machining operation. The model is based on the inverse solution of a physics-based modeling approach of the orthogonal machining operation and the inverse solution of the residual stress prediction from Hertzian stresses. Experimental and modeling data are used to validate the developed model. The work constitutes a novel approach in engineering residual stress in a machined component.

CHAPTER 1

INTRODUCTION

1.1 Overview and Motivation

With the increasing demand for high quality, highly reliable, and economical machined components, the manufacturing industry must find innovative methods for producing precision components. To meet such demand, manufacturers are seeking ways to improve the process planning methodologies. Currently, the process planning methods do not address directly the issues of part performance and functionality. Tremendous improvement of the overall manufacturing process of precision products could be achieved if the parts performance and functionality could be at the center of the planning process.

Machine parts produced with hardened steel are usually high performance components that are frequently loaded to their physical limits [1]. During use severe failures produced by fatigue, creep, and corrosion cracking start at the surface of these components. Thus, the functional behavior of these machined components is greatly dependent upon their surface integrity. Surface integrity is defined as the ability of a surface to meet the demands of specific application. Specifically, it is characterized by its mechanical, metallurgical, chemical and topological states of surface properties such as surface roughness, hardness variation, structural changes and residual stress [2].

Residual stress is defined as the stress state which exists in a body after all the external loads are removed. When assessing surface integrity, residual stress is often considered as one of the most critical parameters since it has a direct effect on the fatigue life of a machined component. The effects of residual stress could be both positive and detrimental on the deformation behavior, fatigue life, dynamic strength, chemical resistance and magnetic properties of machined components [3]. In machining, the sources of residual stress include plastic deformation of the material and high thermal gradients in the cutting zone. These two sources are complex and do affect each other. Plastic deformation occurs during chip formation when the material is being sheared in the cutting zone. Additional plasticity occurs due the rubbing contact between the tool and the newly machined surface. Thermal gradients are caused by plastic deformation and frictional heating. When the thermal gradients are sufficiently high, phase transformation at the surface or near sub-surface of the machined part will occur. Such change in material structure will alter the mechanical properties of the workpiece at the surface region. Consequently, the plastic deformation will be affected. Such complexity in the sources causing residual stress has made modeling the post-process stress in a machined part a challenging task. As can be probably deduced, the plastic deformation and the thermal gradient are directly dependent on how the cutting and tool geometry parameters, and the materials both for the tool and the workpiece were selected.

A tremendous amount of work has been done to characterize the effect of cutting parameters such as width and depth of cut, speed, and tool geometry (i.e. edge radius) on the residual stress that is produced during cutting. This work has included experimental, analytical & statistical, finite element and neural network modeling efforts, [4], [5], [6].

Overall, these models provide a methodology to predict the residual stress profile in a machined part from cutting conditions and tool geometry parameters. However, insight into the mechanisms of residual stress formation is hardly ever given explicitly. Most importantly, these models do not provide a methodology to specify either machining process or tool geometry parameters from a desired residual stress profile into the workpiece.

Being able to design around the residual stress desired or required in a machined component for a specific application is a much needed option. A methodology needs to be established that would allow residual stress to be truly engineered in a workpiece. This methodology would allow for the prediction of an optimal set of cutting process and tool geometry parameters using a desired or required residual stress profile as input. Many other benefits could be derived from such methodology:

- Achievement of a better control over the surface integrity of a part.
- Improvement of Hard Turning competitiveness in replacing multiple grinding processing steps.
- Reduction of trial-and-error tooling design cycle time since a tool geometry information can be extracted from residual stress profile requirement

1.2 Research Goals and Objectives

Currently, no method exists that will help in making recommendation on the cutting and tool geometry parameters if a desired residual stress profile is needed in machined components after the cutting operation. Such method is crucial if the

functionality and performance needs to be truly designed into the machined part. The objectives of this current research are: (1) develop a methodology to predict the depth of cut, the tool edge radius, and the cutting force required from the surface residual stress needed in a machined component and (2) validate the methodology with experimental data.

1.3 Overview of the thesis

In the following chapter, a review of the past and current work on machining induced residual stress will be provided. Further, a summary of the work done in the area of solving inverse problems is given. Chapter 3 will cover the physics-based modeling approach to orthogonal machining. Methods in determining cutting forces, stress state of the workpiece during the cutting action and the resulting residual stresses are presented. Chapter 4 will present in detail a novel inverse methodology that will allow for the prediction of the depth of cut, edge radius and force required to achieve the desired or required residual stress profile in the workpiece. The validation procedure of this new approach will be covered in chapter 5. Conclusions and recommendations for future work will be given in chapter 6.

****

CHAPTER 2

LITERATURE REVIEW

Residual stresses in a machined part have a significant effect on the performance of the part. Since the 1950's, researchers have done work in the prediction of residual stress. Research efforts have been composed of experimental findings, analytical modeling, finite element, neural network and various combinations of these efforts. This chapter will present a review of the previous modeling work in residual stresses produced by machining. Further, a review of the work done in solving inverse problems is given.

2.1 Review on Machining Induced Residual Stress

2.1.1 Experimental Efforts in Residual Stress Modeling

One of the earliest efforts to determine the effect of machining on residual stress was done experimentally around 1950 by Henriksen [4]. The study was conducted on low carbon steel orthogonally machined. Henriksen established that both mechanical and thermal effects played a role in the development of residual stresses, but that mechanical influence dominated.

Liu and Barash work focused on uncovering how different aspects of the machining process affect the residual stress produced [7]. They found that for orthogonal cutting, four variables uniquely determine the pattern of the residual stress on a machined surface. These variables include the length of the shear plane, tool flank wear, the shape

of the cutting edge, and the depth of cut. The shape of the cutting edge was found to govern the residual stress near the machined surface. The length of the shear plane affected the bulk distribution of the stress. The tool flank wear increased the cutting temperature. In addition, a smaller depth of cut was not found to necessarily produce low subsurface stresses. They also concluded that a lower degree of constraint in the deformation process produces a lower level of residual stress.

Sadat[8] looked at the residual stress distribution into the surface of the workpiece for turned AISI 4340 steel. The residual stress distribution was measured using a deflection etching technique. It was found that the absolute value of the residual stresses at the machined surface were low, but increased with increasing depth into the workpiece to a maximum value. After reaching this value, the residual stress value would decrease close to zero with increasing depth. Furthermore, the peak residual stresses and depth of the stressed region increased with an increase in feed rate and depth of cut, but decreased with an increase in cutting speed.

Sadat[9] also experimented with the orthogonal cutting of Inconel-718 nickel-base superalloy. The surface integrity at the workpiece at various cutting speeds, depths of cut and chip-tool contact lengths was investigated. The experimental work involved the determination of residual stress, plastic strain and micro-hardness distributions in the surface region. Both residual stresses and plastic strains decreased and the quality of the machined surface improved with an increase in cutting speed, a decrease in depth of cut and with tools having controlled chip-tool contact lengths.

Schlauer[10] examined the near-surface residual stress distributions that originate during turning in the nickel-based super-alloy Inconel 718. The turning process that was

used in the experiments was a face grooving process which gives quasi-orthogonal cutting conditions. The effects of the cutting speed and feed on the residual stress distribution measured using an optical, and a transmission electron microscopes, were investigated. The work showed that tensile surface residual stresses were due to nano-sized grains while shear bands in the subsurface corresponded to compressive stresses.

Jang[2] studied the surface residual stresses as a function of machining speed, feed rate, depth of cut, and tool geometry and coating for turning of AISI 304 stainless steel. The residual stress tensors were determined using X-ray diffraction. The surface of the workpiece was in state of plane stress with the principal axes directions close to the hoop and axial directions. Additionally, the tool sharpness was found to have the largest effect on residual stress.

With the potential of hard turning as an alternative to grinding[11],[12], significant findings in terms of machining and residual stresses have been made. Hard turning refers to the process of cutting hardened steels with a hardness from 45 to 68 HRC, using a variety of tipped or solid cutting inserts, to final form and finish [13].

Efforts have been made also to characterize the effect of hardness on surface integrity characteristics [3],[14]. Wu and Matsumoto show that material hardness has a significant effect on the pattern of residual stress which remains in machined steel parts. From the experimental evidence presented, the shear angle is found to increase with material hardness. Furthermore, the average stress ratio in the primary deformation zone decreases as hardness increases. This effect leads to a more tensile residual stress in the workpiece. Thus, it was deduced that for machining various hardnesses of work-material

the change in residual stress pattern is mainly caused by the change of the shear angle in the chip formation process.

Jacobson[12] conducted hard turning experiments on hardened M50 steel (61HRC). Tests were conducted using different tools while also varying the depth of cut during turning. Hard-turned M50 steel consistently showed compressive stress at the surface. The effective rake angle and nose radius of the tool affected the amount of residual stress generated in hard turning. Higher negative rake angle and smaller nose radius created a more compressive residual stress profile. The work also showed that the depth of cut did not affect the amount of residual stress generated.

Thiele & Melkote[15],[16] conducted an experimental study to uncover the effect of tool cutting edge geometry on the workpiece subsurface deformation and through-thickness residual stresses for finish hard turning of AISI 52100 steel. Polycrystalline cubic boron nitride (PCBN) inserts with edge hones and chamfers were used as the cutting tools. The inspection of the through thickness residual stresses reveals that large edge hone tools produce deeper and more compressive residual stresses than small edge hone tools or chamfered tools.

2.1.2 Analytical and Statistical Efforts in Modeling Residual Stress

Analytical and statistical modeling offers a clear advantage over pure experimental methods. It allows the quantitative prediction of the effect of cutting parameters on machining induced residual stresses. This section covers the research that has been done in this area of modeling of machining processes.

One of the earliest studies was done in 1975 by Tsuchida et al. [6]. They investigated the effect of cutting conditions on the residual stress distribution obtained in

a turning operation. Cutting conditions such as the speed, the feed and the depth of cut were varied during the study. Several interesting results emerged from this investigation. A decrease of cutting speed decreases the tensile residual stress near the surface and increases the depth of the residual stress layer. An increase of feed shifts the surface residual stress toward tension side while increasing the depth of the residual stress layer. However, an increase in depth of cut did not affect the residual stress distributions. An empirical formula for the surface residual stress was produced from their experiments. Most significantly, it was found that the peak residual stresses can exist beneath the surface of machined components.

Hardness is proved experimentally to have a significant effect on the residual stress formation. The work by Wu and Matsumoto[3] sought to understand the mechanism of residual stress formation during the orthogonal machining of AISI 4340, and to explain the effect of hardness on it. In an effort to model residual stress formation, they employed the idea of a passing load over a point in the workpiece to mimic the cutting process. They assumed that all the points in the workpiece experience the same stress history which subsequently influences residual stress. An integration of the Boussinesq equation is employed to predict the stresses experienced in the subsurface due to the passing load. The analysis is based on the existence of several measurable factors that influence the stress field in the work-material during the cutting process. The sensitivity of these factors to hardness allows establishment of relationships between the hardness and the material loading cycle. The results of the analysis indicate that the residual stress pattern is correlated most strongly to the orientation of the primary deformation zone in metal cutting.

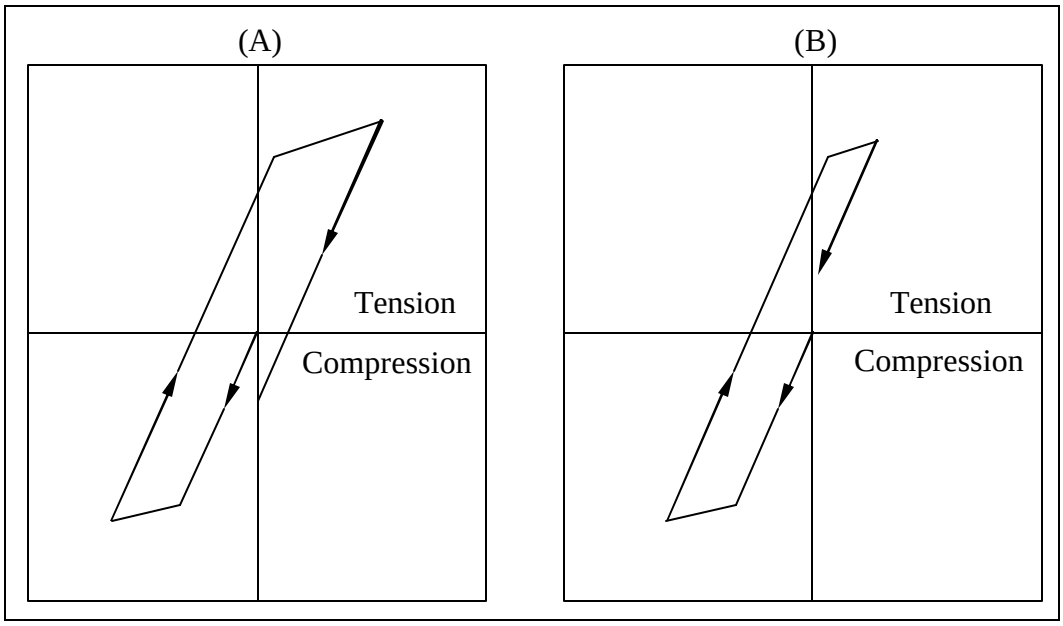

Figure 2-1 Residual stress formation for (A) predominantly tensile loading and (B) predominantly compressive loading [3].

Fuh[17] developed a mathematical model for predicting the residual stresses generated during end-milling of 2014-T6 alloy. Cutting conditions such as the cutting speed, the feed, and the cutting depth, along with the tool geometries (tool nose radius, flank wear), are incorporated in the model. To reduce the number of experiments required for building the model, the Response Surface Methodology coupled with the Takushi method were used. The relationships between the residual stress and the cutting parameters were established through curve fitting. Even though good correlations between the experimental and predicted results were found, the model provided little insight into the physical relationship between the cutting parameters and the residual stress.

Jacobus[18] developed a predictive model for evaluating residual stresses in orthogonal and controlled oblique machining. Based on the experimentally determined flow fields of Enaharo and Oxley[19], the deformation fields were developed for material

points passing beneath the cutting tool. Using these fields, the residual stresses were obtained through an incremental plasticity technique of Merwin and Johnson[20]. The deformation parameters were treated as function of the edge radius and the depth of cut. They were calibrated using experimental tests and optimization procedure. The research provided a rationale for the effect of thermal and mechanical loads on the shape of the residual stress profile. Although the work provided a sound fundamental basis for residual stress modeling, it was still largely dependent on curve fitting for the optimization of critical parameters.

El-Axir[21] used Mittal and Liu's[22] assumptions in an effort to develop a comprehensive experimental model of residual stress. The profile of the residual stress along the depth is assumed to be a polynomial functions of the depth. The coefficients of the polynomial are individual function of the machining parameters. Five different metals were machined by turning. The residual stress distribution in the machined surface region was determined using a deflection-etching technique. The tensile strength of these materials, and both the cutting speed and feed rates were considered as three input parameters affecting residual stress distribution. The model was able to predict both the locations and depth of the maximum residual stress.

Cappello[23] tries to clarify the mechanism of residual stress generation during turning by developing an empirical relationship between residual stresses and process parameters. Three different metals were used in the study. It was found that the feed rate, the tool nose radius and to a minor extent the entrance angle influence the residual stress distribution. The material used only affected the mean level of residual stresses. Thus, the relationship between the most relevant process parameters and the residual stresses was

the same for all investigated material. The author concluded that there exists a common mechanism of residual generation that does not depend on the mechanical properties of the material.

Many of these efforts in modeling residual stresses from machining have focused on a blend of empirical and analytical modeling, with more emphasis on the empirical aspect. This results in models that are very dependent on the material and the process used. Little to no insight into the physical relationship between the cutting parameters and the residual stress is usually given by these models.

Su produced a comprehensive and thorough model for predicting residual stresses from machining process parameters and tool geometry information[24]. The prediction is based on first principles. Machining process output parameters such as cutting forces and cutting temperature were predicted as part of the overall modeling effort. These output parameters were used as the basis for determining the loads which generate residual stresses due to machining. The techniques used differed from previous efforts like that used by Jacobus in that extensive parameter calibration will be unnecessary because the loading inputs are determined from process output parameters such as cutting forces.

2.1.3 Finite Element Modeling of Residual Stress

With more affordable computer resources and modeling capabilities, some researchers have been focusing on the use of finite element as a method for predicting residual stress during machining. The first significant Finite Element Modeling (FEM) analysis was done by Okushima & Kakino[5]. The residual stresses caused by the mechanical effect of the ploughing force which exists at the tool edge and by the thermal effect of the temperature distribution produced in orthogonal cutting process, are

modeled. The model is validated using residual stresses data obtained from X-ray diffraction experiment. Their findings showed that thermal effects lead to tensile residual stresses, and that mechanical effects produced compressive residual stresses. It was found also that in most cases of practical cutting, tensile residual stresses are produced on the machined surface.

Mishra [25] developed an analytical model based on FEM to predict the residual stresses of thermal and mechanical origin due to surface grinding process. The temperature field within the workpiece is determined by considering that the temperature distribution is due to a moving heat source. In order to simulate the motion of the grinding wheel, an iterative procedure is employed to evaluate the effect of the step by step motion of the temperature field and the force. The influence of the magnitude of the mechanical force, the rate of heat input, and the speed of workpiece movement on the residual stresses generated were discussed.

Lin et al. [26] analyzed the combined the effect of thermal and mechanical loads on the residual stress of a machined workpiece. A thermo-elasto-plactic finite element model was used to determine the strain field in the workpiece. From the strain history, the concept of particle flow was used to determine the stress history of the material. The calculated residual displacement was compared with experimental results.

Shih[27] developed a large-strain finite element simulation for the numerical analysis of orthogonal cutting of AISI 1020 using a perfectly sharp cutting tool. The modeling of the work material was very extensive and included the effects of large strain, temperature and strain rate. Distributions of normal and shear stresses, contours, and distributions of parameters along the contact zone, shear zone and under the cut surface

were presented. Furthermore, the distributions of residual stresses under the cut surface were compared with data obtained from X-ray diffraction measurements. Unfortunately like others, the model did not quite give good insight into the mechanisms of residual stress formation.

Hua, Shivpuri et al. [28], used FEM (DEFORM_2D)model which employs a hardness-based flow stress to predict the residual stresses profile during hard turning of AISI 52100 under various conditions. The effects of cutting edge geometry and workpiece hardness as well as cutting conditions, such as feed rate and cutting speed on the residual stresses are investigated. These predictions are validated by face turning experiments which were conducted using a chamfer with hone cutting edge for different material hardness and cutting parameters. A comparative study showed a reasonable agreement between the model predictions and experimental data.

Liu and Guo[29] developed a thermo-elastic-viscoplastic model using the explicit finite element code Abaqus to investigate the effect of sequential cuts and tool-chip friction on residual stresses in a machined layer of AISI 304 stainless steel. They found that the affected layer from the first cut has a significant effect on the residual stress distribution produced by the second cut. The characteristics of the residual stress distribution can be controlled by optimizing the second cut. For example, tensile residual stress on the machined surface in the first cut may be changed to compressive by optimizing the second cut. Furthermore, the residual stress is sensitive to friction condition of the tool-chip interface.

In more recent work by Liu and Guo[30], the same finite element model was used to investigate further what parameters affect the residual distribution in the workpiece. It

was found that cutting forces are dominant factors on the residual stress distribution. For large uncut chip thickness, thermal unloading has an appreciable effect on the residual stress on the machined surface, while its effect on the machined layer is slight; also, cutting force unloading has appreciable effect on the residual stress distribution. For small uncut chip thickness, clamping forces have the largest effect on the residual stress distribution on the machined surface and in the machined layer; cutting force unloading has a slight effect, while thermal unloading has little effect.

Salio et al.[31] developed a two-dimensional finite element model to predict the residual stress distribution during orthogonal cutting. The numerical solution was implemented through the implicit FEM code MSC.Marc. Continuous adaptive remeshing was performed in the simulation. Thermal effect and material work hardening were taken into account. The model results were compared with results from analytical models and with experimental data. In all cases, the FEM-predicted results were found to be in good agreement. Furthermore, the model gave interesting indications on how to select the values of depth of cut in order to reduce tensile residual stresses.

An arbitrary-Lagrangian-Eulerian finite element model is developed by Nasr[32] to simulate the effects of cutting-edge radius on residual stress during orthogonal cutting of austenitic stainless steel AISI 316L. Residual stress profiles started with surface tensile stresses then turned to be compressive at about 140μm from the surface; the same trend was found experimentally. It was also deduced from the model that a larger edge radius induced higher residual stresses in both the tensile and compressive regions, while it had almost no effect on the thickness of the tensile layer. Further, a larger edge radius caused the maximum compressive residual stresses to be pushed deeper into the workpiece. A

stagnation zone was clearly observed when using non-sharp tools, and its size increased with edge radius.

All the finite element studies previously mentioned were done in 2D. Guo and Liu[33] developed recently an explicit 3D finite element analysis model to analyze the turning process of AISI 52100 steels using a PCBN cutting tool. The model incorporated the thermo-elastic-plastic properties of the work material. An improved friction model has been proposed to characterize tool-chip interaction with the friction coefficient and shear flow stresses determined by force calibration and material tests. The finite element model predictions had reasonable accuracy for residual stresses.

Finite element modeling methods have been able to predict the residual stresses due to cutting from process parameters. Although these predictions can be quite accurate, they do not provide a way to reverse the methodology since they don't give good insights on the mechanisms which give rise to machining-induced residual stresses. Furthermore, FEM limits itself from use in an industrial environment due to sizeable computational expense. Any changes in the cutting conditions require re-computing the model which itself is time prohibitive. Consequentially, the use of FEM as a means for production guidance has been restricted.

2.1.4 Neural Network Effort in Modeling Residual Stress

Since the residual stresses at the surface region of a machined part are affected by several parameters such as cutting tool geometry, materials properties and cutting conditions, the methods presented earlier tend to fall a bit short when it comes to an accurate prediction of residual stresses. Researchers have started looking at artificial

neural networks, since they are very useful in applications where conventional analytical or numerical models are either not available or are too complex and difficult to solve.

Artificial Neural Networks are the one of the most powerful computer analysis techniques based on statistical approaches. They are non-linear mapping systems that consist of simple processors, which are called neurons, linked by weight connections. Each neuron has inputs and generates an output that can be seen as the reflection of local information that is stored in connections. The output signal of a neuron is sent to other neurons as input signals via interconnections. Since the capability of a single neuron is limited, complex function can be realized by connecting many neurons. The neural network often consists of at least three layers namely input, hidden, and output layers and the back-propagation training methodology. It is widely reported that the structure of the neural network, representation of data, normalization of inputs-outputs and appropriate selection of activation functions have a strong influence on the effectiveness and performance of the trained neural network. In recent years, ANNs have been extensively applied in the modeling of many metal cutting operations such as turning, milling and drilling.

Liu et al.[34] developed a neural network to detect wear of the drill bit during drilling. The input vector comprised of drill size, feed rate, spindle speed, and eight features obtained by processing the thrust and torque signals. These features were: average thrust, average torque, peak thrust, peak torque, RMS thrust, RMS torque, area under thrust vs. time curve, and area under torque vs time curve. The output was the drill wear state which was either usable or failure. Drilling experiments with various drill sizes, feed rates and spindle speeds were carried out. The learning process was performed

effectively by utilizing back-propagation with smoothing and an activation function slope. The on-line detection of drill wear states was 100% reliable even when the drill size, feed rate and spindle speed were changed.

Dimla and Lister[35] built a neural network to asses the tool state during a turning operation. The test cuts were conducted on EN24 alloy steel using P15 and P25 coated cemented carbide inserts, and online cutting forces and vibration data acquired. Simultaneously the wear lengths on the cutting edges were measured, and these together with the processed data were fed to the neural network trained to distinguish tool-state. The developed system was tested for a variety of cutting conditions, and its ability to distinguish changes in tooling material and cutting conditions from those arising from tool wear was assessed. The system was found to be capable of accurate tool state classification in excess of 90% accuracy but deteriorated when the cutting conditions were significantly changed.

Besides tool wear monitoring, other applications include the used of ANN approaches to determine the optimal cutting conditions for efficient and economic production and the investigation of surface roughness.

The work by Zuperl et al.[36] proposed a new hybrid optimization technique for complex optimization of cutting parameters. The developed approach is based on the maximum production rate criterion and incorporates 10 technological constraints. The multi-objective technique of optimization of cutting conditions is achieved by means of artificial neural network and OPTIS routine which take into consideration the technological, economic and organizational limitations. Experimental results show that the proposed optimization algorithm for solving the nonlinear-constrained programming

problems is both effective and efficient, and can be integrated into an intelligent manufacturing system for solving complex machining optimization problems.

An artificial neural network model was developed by Ezugwu et al. for the analysis and prediction of the relationship between cutting and process parameters during high-speed turning of nickel-based, Inconel 718. The input parameters of the ANN model were the cutting parameters: speed, feed rate, depth of cut, cutting time, and coolant pressure. The output parameters of the model are seven process parameters measured during the machining trials: tangential force, axial force, spindle motor power consumption, machined surface roughness, average flank wear, maximum flank wear and nose wear. The model consists of a three-layered feed forward backpropagation neural network. The network is trained with pairs of inputs/outputs data sets generated when machining Inconel 718 alloy with triple (TiCN/Al2O3/TiN) PVD-coated carbide inserts. A very good performance of the neural network, in terms of agreement with experimental data, was achieved.

Recently, Umbrello et al.[37]made use of an artificial neural network to predict subsurface residual stresses in hard machining for different combinations of material properties, cutting tool geometries and cutting conditions. The three layer neural network was trained on selected data from chosen experiments on hard machining of 52100 bearing steel, and then validated by comparing with data from numerical investigations, and empirical data from published literature. Predictions errors ranged between 4 and 10% for the whole data set. The authors claimed that the model developed could be used to predict process parameters from residual stresses.

As mentioned, residual stress at the surface region of the workpiece is affected by several parameters. At a first glance, an artificial neural network seems to be a great method to use to predict accurately and efficiently the residual stresses from cutting process parameters. According to Shick[38], who conducted a review of more that a decade of research, ANN is not marketable right now and has yet to been in industry[39],[40]. The reasons are due to the insufficient generalization capabilities, as the use is restricted to a specific machine tool, only a small range of cutting conditions is allowed or time consuming "teach-in" cycles are needed.

2.2 Literature Review on Inverse Method Modeling.

The concept of the inverse problem has been applied in a wide range of scientific and engineering disciplines in recent years. It usually implies identification of inputs from outputs, or determination of unknown causes from known consequences. Some examples include reconstruction of a topographic image from X-ray shadow pictures, inverse scattering for detecting defects of materials, determination of mass distribution of mechanical structures by their natural frequencies, estimation of the properties of the earth, identification of heat conductivity from boundary conditions and determination of boundary tractions from stress data [41].

In general, a mathematical model is used to describe the objective revolution process of a physical phenomenon and it fully reflects the phenomenon. Initial and boundary conditions are given later. Approaching a problem in such a direction normally leads to a well-posed solution which refers to the presence of a unique and continuous solution to a mathematical equation. For a mathematical equation without sufficient

constraints the solution is rarely unique; with too many constraints, the solution will not exist.

In an inverse problem, some of the conditions are known while the others are unknown, making a gray system. Such a problem usually generates an improperly posed or ill-posed solution which makes it difficult to derive the representation of the solution. Numerical methods tend to be used to solve inverse problems. However, there are too many iteration calculations to handle, and such methods are prone to solution instability[42].

Tikhonov and Arsenin [43] proposed a concept of solving problems with an ill-posed solution in the field of engineering. They suggested that solution of an inverse problem included the analysis and optimization processes. During the analysis process, the unknown conditions are first replaced by assumptions; then a finite element method or finite difference method must be used to solve the problem generating a set of numerical solutions. The results need to be compared with measured (experimental) data to obtain residual values. During the optimization process, a regularization item is added to form a non linear problem. An acceptable estimated value can be derived from a non-linear problem by means of numerical optimization methods such as the conjugate gradient method or Gauss-Newton method

The engineering inverse problem was first used in the problem of unknown heat source. Sparrow et al.[44] used the differential method and Laplace transform to inversely derived the temperature and heat flux at surface of a solid when only the temperature at the interior location is prescribed. Trujillo[45] used a dynamic

programming method and generalized cross validation (GCV), plus the L-curve, to solve the inverse heat transfer problem, structural and vibration problems.

Garo and Mura [41] have used the residual surface displacements to determine the residual stress field in the vicinity of the damage domain caused by a series of unknown loading. It has been shown that the equivalent plastic strains, though different from actual ones, induce the actual stresses outside of the equivalent damage domain. They claimed that the results presented could be extended to the inversion of residual stresses caused by cracks and inhomogeneities. Beck[46] adopted the sensitivity concept to solve non-linear and multi-dimensional heat transfer of the inverse heat conduction problem.

Yeih and Koya[47],[48] presented a theoretical approach of solving an inverse elasticity problem with partially over-prescribed boundary conditions. The regularization method, which has been employed by Gao and Mura, is used to solve the problem indirectly. Chao et al.[49]studied the two-dimensional elasticity problem an isotropic material, containing a centered-crack with unknown boundary traction using the inverse procedure. The goal of their work was to establish a frame work of solving the unknown traction problem of a complex marine structure. The conjugate gradient method and the regularization method are utilized during the inverse procedure. It was found that when the stress data is used in the inverse analysis, the predicted boundary traction is more accurate than those using displacement data.

In the manufacturing area, Huang et al. [50] used the conjugate gradient method to inversely solve the unknown contact convection value during metal casting. Using the conjugate gradient method, there was no need for the assumption of a specific functional form for the unknown quantity, since the solution automatically determines the functional

form over the domain specified. The method proved to be stable and converged over an order of magnitude faster than the least square method.

Lin et al.[51]developed an inverse calculation process for the upsetting process based on the combination of the axial symmetric thermo-elastic-plastic finite element method, the concept of inverse calculation and the Levenberg-Marguardt method plus a constraint function and the setting of a convergence criterion. The developed process was used to inversely solve for the variation of the friction coefficient during the upsetting process of mild steel by the experimented load.

Yvonnet and al.[52]developed an inverse procedure to determine the heat flux distribution flowing into the tool through the rake face and the heat transfer coefficient between the tool and the environment during a typical orthogonal cutting process. The procedure is based on integrations of numerical simulations, inverse approach algorithms and experimental tests. A finite element model is created to model the region of interest. A set of instrumented split-tools, characterized by embedded thermo-couples and properly designed tight slots filled with non-conductive material, are used to measure temperature at the tool tip during cutting. They assume that the real heat flux distribution could be approximated by a piecewise constant function. Using the measured temperatures, the average heat flux (Qi) was found by doing an iterative Newton-Raphson procedure to minimize an error term defined by the difference between the calculated and the experimental temperature history at a point of the tool.

2.3 Summary

In this chapter, a literature review of the modeling work done on machining induced residual stresses is given. A review of the work on solving inverse method is also given. As presented, no work exists in determining process parameters from a given residual stress profile, and most of them gave little insight into the mechanisms of residual stress formation. Nonetheless, the work done by Su based on first principles could help with the development of an inverse method in predicting process parameters. The review of the work done on inverse modeling reveals that a pure mathematical approach is impractical in developing an inverse method for this research in view of the fact that the boundary conditions such as length of the shear zone, the length of the contact between the tool and the newly generated surfaces, and the deformed surface geometry are all unknown.

The basic objectives of this research are (1) develop a methodology to predict the depth of cut, the tool edge radius, and the cutting forces required from the surface residual stress needed in a machined component and (2) validate the methodology with experimental data.

The research will fill in the void that exist in the area of machining induced residual stress by providing a method to extract machining process information from residual stresses. This methodology would allow for the prediction of an optimal set of cutting process and tool geometry parameters using a desired or required residual stress profile as input. Many other benefits could be derived from such methodology:

- Achievement of a better control over the surface integrity of a part.

- Improvement of Hard Turning competitiveness in replacing multiple grinding processing steps.
- Reduction of trial-and-error tooling design cycle time since a tool geometry information can be extracted from residual stress profile requirement

The methodology will consist in developing an analytical model based on developing inverse solutions to the physics-based description of an orthogonal cutting process.

****

CHAPTER 3

FIRST-PRINCIPLES BASED MODELING OF AN ORTHOGONAL CUTTING PROCESS.

Residual stress modeling in the area of machining has been the subject of research because of the direct effect of this type of stress on the performance of a machined part. As presented in the previous chapter, the modeling efforts have included experiments, analytical & statistical, finite element, and neural network methods. Throughout the previous research work, several parameters have been identified as having an effect on residual stress formation. Among these parameters are the tool geometry (hone radius, rake angle, flank wear), the cutting conditions (depth of cut, cutting speed) and the material behavior (hardness, flow stress). Even though these parameters have been recognized as being significant in residual stress formation, the previous research efforts do not provide a clear insight into the mechanisms of residual stress formation. The quantitative and qualitative effect of each parameter could be hard to determine.

In order to come up with an inverse methodology that enables the prediction of cutting conditions and tool geometry parameters from a desired residual stress profile, the mechanisms of residual stress formation have first to be clearly established. A first-principles based approach to machining coupled with stress prediction provides the means necessary to develop the inverse methodology sought after. The meaning of first-principles modeling or physics based modeling is that the forces generated during cutting will be determined from the cutting parameters using physics based relations. Then, using

these loads as input, the residual stress can be determined without the need for extensive parameters calibration.

In the next sections of the chapter, the physics based modeling approach to orthogonal machining is covered. The methods in determining the cutting forces, the stress state and the resulting residual stresses are presented.

3.1 Force Modeling

A lot of research work about forces estimation during machining has been done over the over the years. One of the earliest analyses of cutting forces was done by Merchant [53]. His work was based on the assumption that the shear angle adjusts itself to minimize the cutting force. Others have incorporated a slip line theory to predict the cutting forces in orthogonal cutting [54-56]. These forces consist of the "sharp tool" forces generated due to the chip formation and the ploughing forces due to the tool edge radius. In the next two sections, the work done by Oxley to estimate the "sharp tool" forces and the work done by Waldorf to model the ploughing forces will be presented.

3.1.1 Forces generated using a sharp tool

The forces generated using a sharp tool are well captured by Oxley's work [54]. He developed a slip-line cutting force model derived from experimental observations in metal cutting. Plain strain, steady state conditions are assumed. The geometrical representation of the critical parameters of the models is provided in figure 3.1.

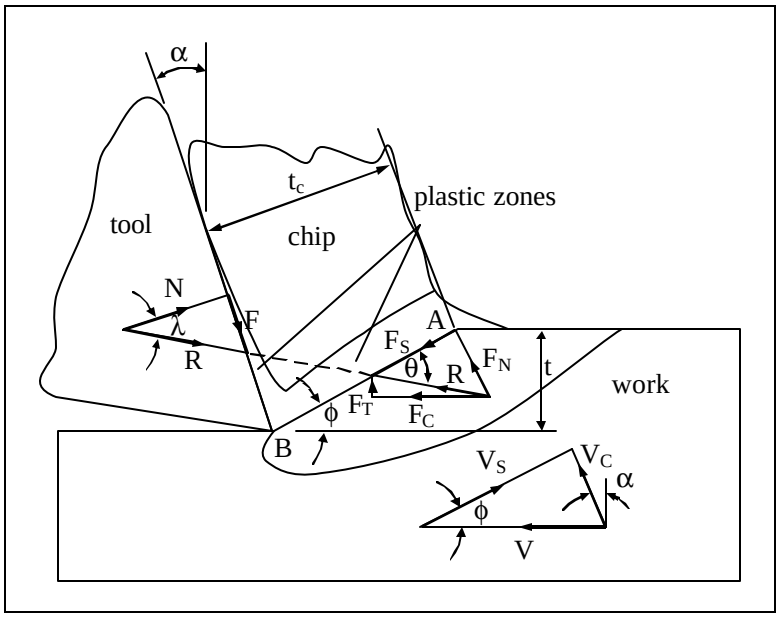

Figure 3-1. Model of chip formation used in Oxley's analysis

The most critical parameter, the shear angle f, is selected so that the resultant forces transmitted by the shear plane AB and the tool-chip interface are in equilibrium. The Oxley's approach to finding the appropriate shear angle is calculated iteratively. Once the shear angle is defined, other parameters (i.e. chip thickness) are determined.

Oxley in his work assumed that the material flow stress is a constant once the material is specified. However, during the cutting process, high strain, strain rates, and temperatures are generated in the cutting zone. Therefore, the material flow stress as a function of strain, strain rate, and temperature needs to be incorporated in the original Oxley's shear angle estimation. The Johnson-Cook flow stress equation is used to model the material flow stress[57].

$$s = \left(A + Be_p^{\,n}\right)\left(1 + C\ln\frac{\dot{e}_p}{\dot{e}_0}\right)\left(1 - \left(\frac{T - T_0}{T_m - T_0}\right)^m\right) \qquad \textbf{Eq. 3-1}$$

where s is the effective stress, e_p is the effective plastic strain, $\dot{e}_p$ is the effective plastic strain rate, T is the temperature of the material, T_m is the melting point of the material,

and T_0 is a reference temperature; the terms A, B, C, m, n, and $\dot{e}_0$ are material constants. The following is a simplified flowchart of Oxley's cutting force Model.

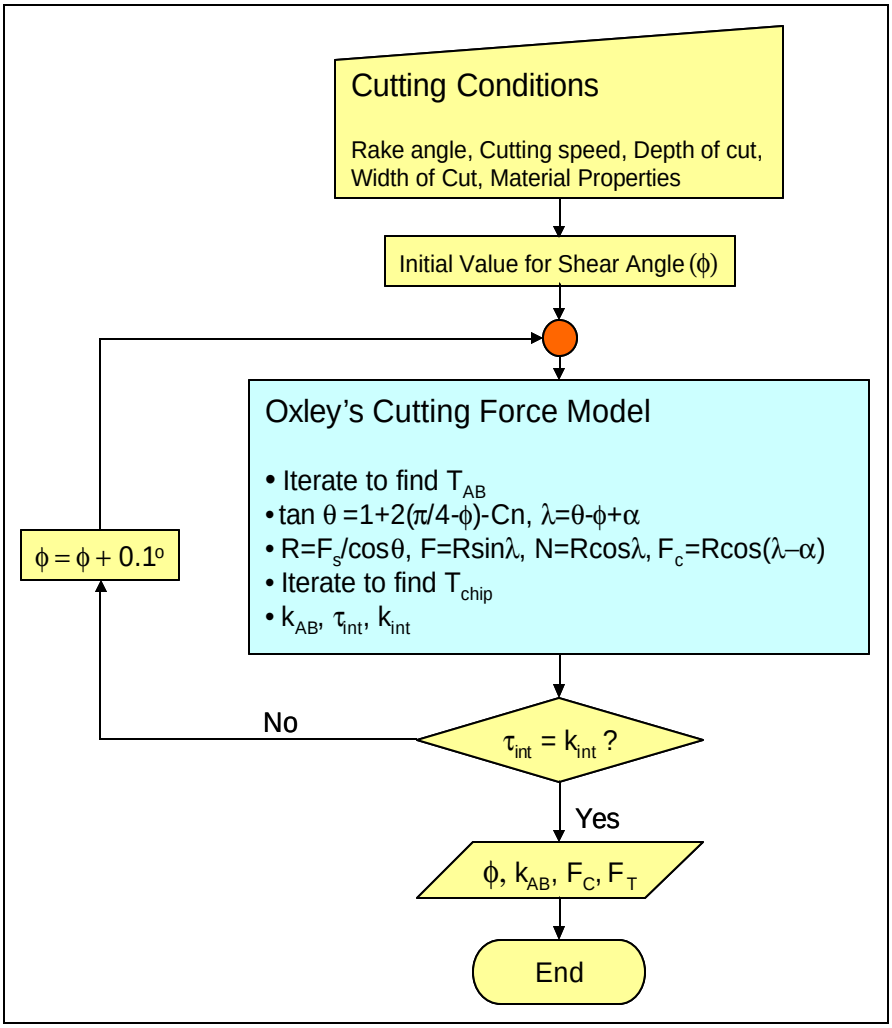

Figure 3-2 Simplified flowchart of Oxley's cutting force model

From an initial value for the shear angle based on cutting conditions, the temperature rise in region AB is computed in order to predict the flow stress k_{AB} in AB. The strain along AB is given by

$$e_{AB} = \frac{1}{2\sqrt{3}} \frac{\cos a}{\sin f \cos(f - a)} \qquad \textbf{Eq. 3-2}$$

and the strain rate along *AB* is given by

$$\dot{e}_{AB} = \frac{C_{Oxley}}{\sqrt{3}} \frac{V_S}{l} \qquad \textbf{Eq. 3-3}$$

The flow stress along *AB* is then given by

$$k_{AB} = \frac{1}{\sqrt{3}} \left(A + B e_{AB}^{\ n} \right) \left(1 + C \ln \frac{\dot{e}_{AB}}{\dot{e}_0} \right) \left(1 - \left(\frac{T_{AB} - T_0}{T_m - T_0} \right)^m \right) \qquad \textbf{Eq. 3-4}$$

After the flow stress is determined, the cutting forces are computed using the following equation

$$\begin{aligned} t_C &= t \cos(f - a) / \sin f \\ F_C &= R \cos(l - a) \\ F_T &= R \sin(l - a) \\ F &= R \sin l \\ N &= R \cos l \\ R &= \frac{F_S}{\cos q} = \frac{k_{AB} t w}{\sin f \cos q} \end{aligned} \qquad \textbf{Eq. 3-5}$$

The friction angle λ is given by

$$l = q + a - f \qquad \textbf{Eq. 3-6}$$

where the inclination angle q of the resultant force is given by

$$\tan q = 1 + 2\left(\frac{p}{4} - f \right) - Cn \qquad \textbf{Eq. 3-7}$$

In the above equation, the term *Cn* used in the present application differs from the original definition in Oxley's model. The modified version allows the Johnson-Cook flow stress model to be incorporated into the cutting force model. The modified *Cn* term used is based on modifications to the original Oxley model presented by Wang [58]. It is defined by

$$Cn = C_{Oxley} n \frac{B e_{AB}^{n}}{A + B e_{AB}^{n}} \qquad \textbf{Eq. 3-8}$$

where *A*, *B*, and *n* are constants defined in the Johnson-Cook flow stress equation.

After the angles are determined, the tool-chip contact length is computed by

$$h = \frac{t_1 \sin q}{\cos l \, \sin f} \left\{ 1 + \frac{Cn}{3 \tan q} \right\} \qquad \textbf{Eq. 3-9}$$

Assuming the stress distribution along the tool chip contact length is constant, the shear stress along the tool chip interface is given by

$$t_{int} = \frac{F}{hw} \qquad \textbf{Eq. 3-10}$$

The temperature rise in the chip is then computed based on the method described by Oxley [54]. The resulting expression for the average flow stress in the chip is given by:

$$k_{chip} = \frac{1}{\sqrt{3}} \left(A + B e_{int}^{n} \right) \left(1 + C \ln \frac{\dot{e}_{int}}{\dot{e}_0} \right) \left(1 - \left(\frac{T_{int} - T_0}{T_m - T_0} \right)^m \right) \qquad \textbf{Eq. 3-11}$$

The average value of strain in the chip is approximated by [59] as

$$e_{int} = 2 e_{AB} + \frac{1}{\sqrt{3}} \frac{h}{d t_2} \qquad \textbf{Eq. 3-12}$$

and the strain rate in the chip by

$$\dot{e}_{int} = \frac{1}{\sqrt{3}} \frac{V_C}{d t_2} \qquad \textbf{Eq. 3-13}$$

For each shear angle f increment, all of the computations are made to determine t_{int} and k_{chip}. The highest value of f at which $t_{int} = k_{chip}$ is chosen as the shear angle for the process. The outputs of the model include the shear angle f, flow stress, cutting force F_{cut} and thrust force F_{thrust}.

3.1.2 Tool with edge radius

The model proposed by Oxley predicts the cutting force components for a perfectly sharp tool (edge radius = 0). However, the tools are never perfectly sharp. In order to instill strength and roughness in the cutting edge, a hone or chamfer is usually added to the tool geometry.

In 1960, the studies of ploughing in metal cutting were first attempted to explain why the apparent coefficient of friction between the rake face of the tool and the chip varied with rake angle; a finite radius on the cutting edge was believed to be responsible by contributing additional force on the material downward below the edge and pressing into the workpiece [60]. Since then, a significant amount of work has been done regarding the contribution of the hone radius to the overall force required during machining [61-66].

Among the different models to capture the ploughing forces due to tool edge roundness[67], [68],[69] the model developed by Waldorf [56, 66] provides a reasonable method for predicting the ploughing forces and decomposing a measured force into shearing and ploughing components. The new slip-line model incorporates the observed phenomena of a small build up edge of material adhering to the edge and a raised prow of material forming ahead of the edge. The geometrical representation of the cutting zone is shown in figure 3.3.

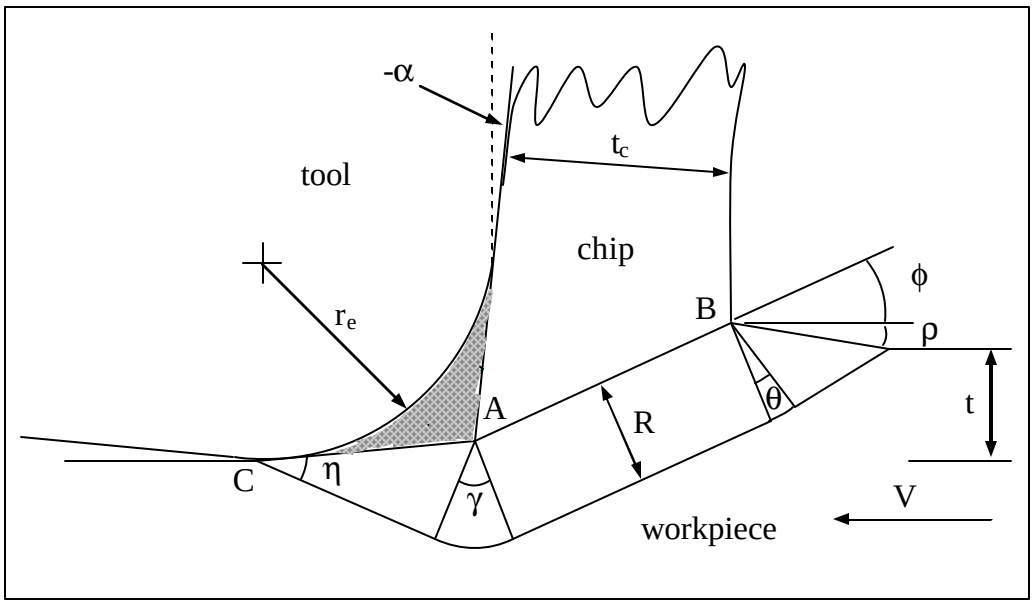

Figure 3-3. Waldorf's slipline field for ploughing [56]

In the above figure, r_e is the edge radius, a is the rake angle, f is the shear angle, r is the prow angle, R is the radius of the circular fan field centered at *A*, and t is the depth of cut.

The stable build-up region is shown shaded with point A at the point of material separation. *AB* essentially represents the traditional shear plane inclined at the shear angle f. The prow is inclined at angle r with respect to the uncut workpiece surface. The vertical distance between the uncut workpiece surface and the machined workpiece surface is the uncut chip thickness t_c.

The remainder of the field below *AB* can be determined from frictional and geometric considerations. Due the high normal stresses on the lower interface between the tool (build-up region) and the workpiece *CA*, a constant frictional stress t is assumed proportional to the material shear flow stress as described by the following equation:

$$t = m * k \qquad \textbf{Eq. 3-14}$$

where m is the friction factor, and k is the flow stress of the material.

According the governing rules of slip-line field theory[70], slip-line meets the bottom surface of the built-up region at angles h and $p/2-h$ according to

$$h = 0.5\cos^{-1}(m) \qquad \textbf{Eq. 3-15}$$

The fan field angles q and g are found from geometrical considerations to be

$$q = \frac{p}{4} - r - f \qquad \textbf{Eq. 3-16}$$

and

$$g = h + f - \sin^{-1}\left(\sqrt{2}\sin(r)\sin(h)\right) \qquad \textbf{Eq. 3-17}$$

R, the radius of the circular fan field centered at A, is found by using the following equation

$$R = \sin(h)\sqrt{\left(r_e \tan\left(\frac{p}{4}+\frac{a}{2}\right)+\frac{\sqrt{2}R\sin(r)}{\tan\left(\frac{p}{2}+a\right)}\right)^2 + 2\left(R\sin(r)\right)^2} \qquad \textbf{Eq. 3-18}$$

The shear angle f is found from measurement of the cut chip thickness t according to

$$\tan(f) = \frac{\frac{t_c}{t}\cos(a)}{1-\frac{t_c}{t}\sin(a)} \qquad \textbf{Eq. 3-19}$$

With a correct estimation of the flow stress of the material, the ploughing forces can be determined by the following set of equations:

$$\begin{aligned} P_{cut} &= k \cdot w \begin{bmatrix} \cos(2h)\cos(f-g+h)+ \\ \left(1+2q+2g+\sin(2h)\right)\sin(f-g+h) \end{bmatrix} \cdot CA \\ P_{thrust} &= k \cdot w \begin{bmatrix} \left(1+2q+2g+\sin(2h)\right)\cos(f-g+h)- \\ \cos(2h)\sin(f-g+h) \end{bmatrix} \cdot CA \end{aligned} \qquad \textbf{Eq. 3-20}$$

where the length of the build up region $CA = \frac{R}{\sin h}$

3.1.3 Average angle

The last two sections dealt with estimating the ploughing forces due to roundness of the tool edge and the forces due to a sharp tool. In these modeling efforts, the rake angle used was assumed to be equal to the nominal rake angle of the tool. However, due to the roundness of the tool, the effective rake angle will undoubtedly vary with the depth of cut as well as the size of the cutting edge. It has been shown that for a shallow depth of cut relative to the radius of the cutting edge, the effective rake angle will become more negative compared to the nominal rake angle.

Manjunathaiah [71] developed a model to estimate the effective rake angle necessary for force modeling. The essential elements of his model are depicted in the figure 3.4. The average rake angle, a_{avg}, will depend on the uncut chip thickness t, the edge radius r_e, the separation or stagnation point angle q, and the nominal rake angle of the tool a. Material above the separation point P goes to the chip while the material below will be part of the workpiece. The separation angle has been known to play an important part and it has been studied previously by some researchers [61, 72, 73]. Basuray [61] derived the value for the separation angle by an approximate energy analysis. The value was found to be approximately 37.6°.

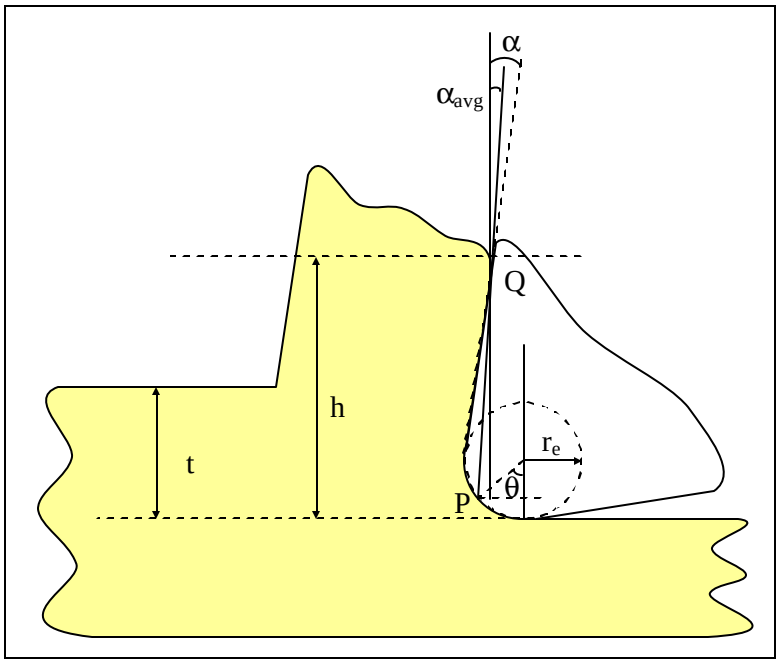

Figure 3-4 Adapted from Manjunathaiah [71]. Schematic for computing the average rake angle

If the tool geometry and cutting conditions are known, then there are two possibilities for the average rake angle. For the case where the uncut chip thickness is less than the radius of the cutting tool, the average rake angle is given by

$$a_{avg} = \begin{cases} \tan^{-1}\left(-\dfrac{\sqrt{\left(2 - h/r_e\right) h/r_e} - \sin q}{h/r_e - 1 + \cos q} \right) & when \;\; h/r_e \le 1 + \sin a \\ \tan^{-1}\left(\dfrac{\left(h/r_e - 1\right)\tan a - \sec a + \sin q}{h/r_e - 1 + \cos q} \right) & when \;\; h/r_e > 1 + \sin a \end{cases} \qquad \textbf{Eq. 3-21}$$

If the uncut chip thickness is greater than the edge radius then the average rake angle is given by

$$\alpha_{avg} = \begin{cases} \tan^{-1}\left(-\dfrac{2\sqrt{\left(1 - h/r_e\right) h/r_e} - \sin\theta}{2h/r_e - 1 + \cos\theta} \right) & when \;\; h/r_e \le \dfrac{1+\sin\alpha}{2} \\ \tan^{-1}\left(\dfrac{\left(2h/r_e - 1\right)\tan\alpha - \sec\alpha + \sin\theta}{2h/r_e - 1 + \cos\theta} \right) & when \;\; h/r_e > \dfrac{1+\sin\alpha}{2} \end{cases} \quad \textbf{Eq. 3-22}$$

3.2 Temperature Modeling

The thermal effects due to the cutting process can have a significant effect on the residual stresses produced. Researchers have shown that increased cutting temperatures result in greater tensile residual stress on the surface of a machined component [4, 26]. Jaeger [74] developed a method of determining the temperature rise due to moving heat sources. Extensions of his method have been used extensively in the literature to determine the temperature rise due to cutting [75-77].

3.2.1 Modeling Workpiece Temperature Rise

In modeling the workpiece temperatures, two heat sources are assumed to exist. The first is the primary heat source generated from the shear zone. The second heat source is a result of rubbing between the tool and the workpiece. The workpiece surface is considered to be insulated in this study as illustrated in figure 3.5. To satisfy the adiabatic condition at the workpiece boundary, an imaginary heat source is used [75].

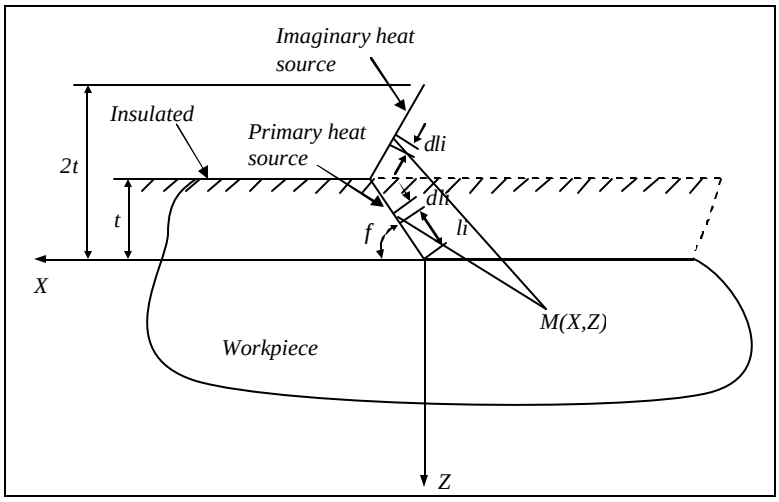

Figure 3-5 Adapted from [78]. Heat transfer model of primary source relative to workpiece

The temperature rise at a point *M(X, Z)* is the combination of the primary and imaginary heat sources. The total temperature rise at any point *M(X, Z)* due to the oblique moving heat source and the imaginary heat source is given by:

$$q_{workpiece-shear}(X,Z) = \frac{q_{shear}}{2p\,k_{workpiece}} \int_0^L e^{-\frac{(X - l_i \sin j)V_{cut}}{2a_{workpiece}}} \left\{ K_0\left[\frac{V_{cut}}{2a_{workpiece}} \sqrt{(X - l_i \sin j)^2 + (Z - l_i \cos j)^2} \right] \right. \quad \textbf{,Eq. 3-23}$$
$$\left. + K_0\left[\frac{V_{cut}}{2a_{workpiece}} \sqrt{(X - l_i \sin j)^2 + (Z + l_i \cos j)^2} \right] \right\} dl_i$$

where $j = \left(f - \frac{p}{2} \right)$ and $L = \frac{t}{\sin f}$.

A similar application of the moving heat source is used to determine the temperature rise due to rubbing between the cutting edge and the workpiece. The rubbing between the tool edge and the workpiece is treated as a moving band heat source. Since the workpiece surface is considered insulated, an imaginary heat source coincident with the original rubbing heat source is used to model the temperature rise. The moving

band heat sources are shown in figure 3.6. The temperature rise in the workpiece due to rubbing is given by equation 3-24

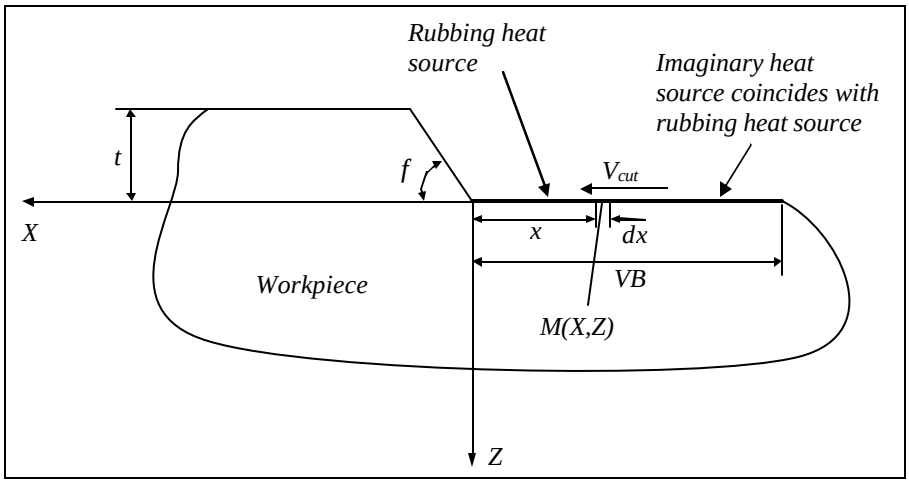

Figure 3-6 Adapted from [78]. Heat transfer model of rubbing heat source relative to workpiece

$$q_{workpiece-rubbing}(X,Z) = \frac{1}{p\,k_{workpiece}} \int_0^{VB} g \cdot q_{rubbing}(x) e^{-\frac{(X-x)V_{cut}}{2a_{workpiece}}} K_0 \left[\frac{V_{cut}}{2a_{workpiece}} \sqrt{(X-x)^2 + (Z)^2} \right] dx \quad \textbf{Eq. 3-24}$$

g in the equation is a partition of heat transferred into the workpiece during cutting. An approximate value for the partition ratio based on material properties of the tool and the workpiece is given as

$$g = \frac{\sqrt{krC}}{\sqrt{krC} + \sqrt{k_t r_t C_t}} \quad \textbf{Eq. 3-25}$$

where k, r, C, k_t, r_t, *and* C_t, are the thermal conductivity, density, and specific heat of the workpiece and tool, respectively [79].

The heat sources q_{shear} and $q_{rubbing}$ are determined from the cutting parameters and the cutting force models described in the previous section. The resulting expressions for the shear plane heat source and the rubbing heat source are given by equations 3-26 and 3-27, respectively.

$$q_{shear} = \frac{(F_c \cos f - F_t \sin f)(V_{cut} \cos a / \cos(f - a))}{(t)(w)\csc f} \quad \textbf{Eq. 3-26}$$

$$q_{rubbing} = \frac{P_{cut} V_{cut}}{(w)VB} \quad \textbf{Eq. 3-27}$$

3.3 Stress Modeling

3.3.1 Elastic Stress Field

Capturing the stress history experienced by the workpiece during cutting is necessary to predict residual stresses. To obtain the stress history, a rolling/sliding approach that can model the cutting operation is used. In this approach, the contact between the tool and the workpiece is represented by a cylinder rolling on a semi-infinite plane, as shown by figure 3.7. The point A seen in this figure represents an arbitrary point in the workpiece. The load exerted by the tool on the workpiece is given by the overall cutting force estimated in the previous section. As a reminder, the cutting force consists of the force components from both the sharp and rounded edge tools.

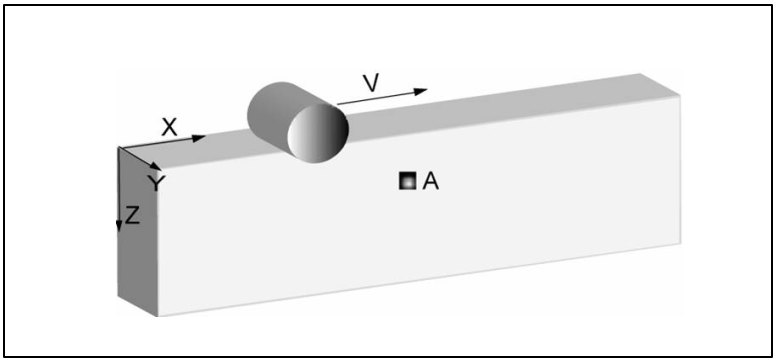

Figure 3-7 3D representation of an orthogonal cutting process

The 3D model depicted in figure 3.7 can be further simplified geometrically down to a 2D problem by assuming a plain strain condition (the deformation into the page is

negligible). The load distribution experienced by the semi-infinite plane due to contact by the cylinder is derived from classical Hertz theory[20].

Given a normal load P_{normal}, the shear load Q_{normal} is obtained using equation 3-28 where m is the coefficient of friction. By using this relationship between the two loads, the cylinder is considered to be sliding and not rolling on the surface of the semi-infinite plane or workpiece[80]. Further, this relation helps truly characterize an orthogonal machining operation where a tool is sliding, as opposed to rolling on the workpiece.

$$Q_{normal} = mP_{normal} \quad \textbf{Eq. 3-28}$$

Since the theory deals with a line contact, the force per unit width is calculated:

$$P = \frac{P_{normal}}{w} \quad \textbf{Eq. 3-29}$$

The Hertzian pressure p_o is obtained from the following equation:

$$p_0 = \frac{2P}{pa} \quad \textbf{Eq. 3-30}$$

The distance a is the contact half width which is expressed as

$$a = \sqrt{\frac{4P}{p}\left(\frac{1}{R_1}+\frac{1}{R_2}\right)^{-1}\left[\frac{1-u_1^2}{E_1}+\frac{1-u_2^2}{E_2}\right]} \quad \textbf{Eq. 3-31}$$

where R1 and R2 represent the radii of curvature of two cylinders, and E1, E2 and v1, v2 are the respective Young's moduli and Poisson's ratios. In the case of sliding on a flat half-space, R2 = ∞.

The semi elliptical distribution of the both normal and tangential pressure are given by the following equations and depicted in figure 3.8

$$p(s) = p_0\sqrt{1-\left(\frac{x}{a}\right)^2} \quad \textbf{Eq. 3-32}$$

$$q(s) = m\, p_0 \sqrt{1 - \left(\frac{x}{a}\right)^2} \qquad \textbf{Eq. 3-33}$$

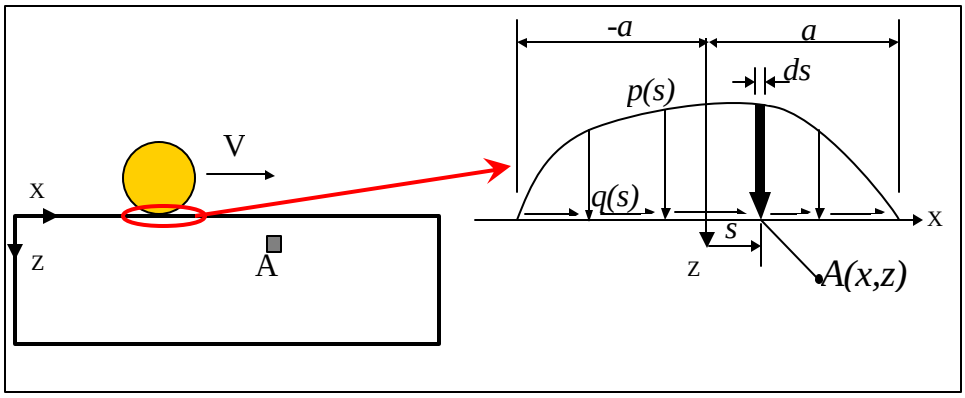

Figure 3-8. 2D representation of contact load during an orthogonal cutting process.

In an orthogonal machining process, there are two load sources. One sources due to shearing action during cutting (sharp) and the other is due to the rubbing of the tool on the newly generated surface because of the tool roundness. These two sources are depicted in figure 3.9

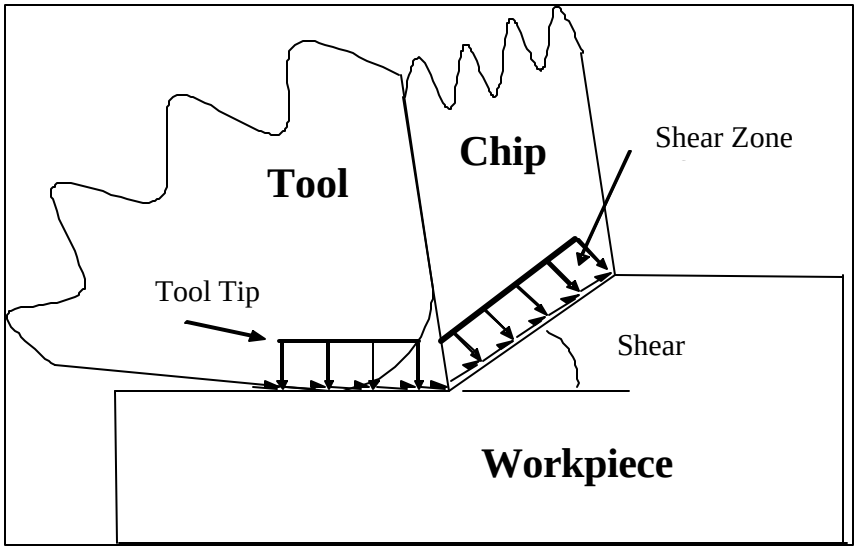

Figure 3-9. Loads due to the shearing action and the roundness of the tool tip

In his work on residual stress modeling, Su shows that no significant loss in accuracy occurs by assuming that the normal pressure and tangential pressure are

uniformly distributed for both regions [24]. From the force components obtained from shearing action (sharp tool) conditions, the p_0^{sharp} and q_o^{sharp} are obtained as follows

$$p_0^{sharp} = \frac{F_{cut}\sin(f) + F_{thrust}\cos(f)}{w(AB)} \quad \textbf{Eq. 3-34}$$

$$q_0^{sharp} = -flowstress \quad \textbf{Eq. 3-35}$$

From extra force components (plouging forces) due to rubbing of the tool of newly generated surface, the p_0^{plow} and q_o^{plow} are obtained as follows

$$p_0^{plow} = \frac{P_{thrust}}{w(CA)} \quad \textbf{Eq. 3-36}$$

$$q_0^{plow} = m\frac{P_{cut}}{w(CA)} \quad \textbf{Eq. 3-37}$$

From the normal and tangential pressure on the surface of the semi-infinite plane or workpiece, many researchers like Smith and Liu have developed analytical expressions of the stress field inside the semi-infinite plane[81]. Wu and Matsumoto used a similar method to determine the stress fields due to shear loads in a cutting operation[3]. The stress components at a point A into the workpiece, while the tool is sliding over the surface can be determined analytically.

For every step of the cylinder at the surface of the workpiece, the expressions for the stress components at point A due to the edge radius are determined by the following set of equations:

$$s_{xx}^{*,plow} = -\frac{2z}{p}\int_{-CA/2}^{CA/2}\frac{p_0^{plow}(x-s)^2}{\left[(x-s)^2+z^2\right]^2}ds - \frac{2}{p}\int_{-CA/2}^{CA/2}\frac{q_0^{plow}(x-s)^3}{\left[(x-s)^2+z^2\right]^2}ds$$

$$s_{zz}^{*,plow} = -\frac{2z^3}{p}\int_{-CA/2}^{CA/2}\frac{p_0^{plow}}{\left[(x-s)^2+z^2\right]^2}ds - \frac{2z^2}{p}\int_{-CA/2}^{CA/2}\frac{q_0^{plow}(x-s)}{\left[(x-s)^2+z^2\right]^2}ds \qquad \textbf{Eq. 3-38}$$

$$t_{xz}^{*,plow} = -\frac{2z^2}{p}\int_{-CA/2}^{CA/2}\frac{p_0^{plow}(x-s)}{\left[(x-s)^2+z^2\right]^2}ds - \frac{2z}{p}\int_{-CA/2}^{CA/2}\frac{q_0^{plow}(x-s)^2}{\left[(x-s)^2+z^2\right]^2}ds$$

The stress components due to the shear zone are computed using the following set of equations.

$$s_{xx}^{*,sharp} = -\frac{2z}{p}\int_{-AB/2}^{AB/2}\frac{p_0^{sharp}(x'-s)^2}{\left[(x'-s)^2+z'^2\right]^2}ds - \frac{2}{p}\int_{-AB/2}^{AB/2}\frac{q_0^{sharp}(x'-s)^3}{\left[(x'-s)^2+z'^2\right]^2}ds$$

$$s_{zz}^{*,sharp} = -\frac{2z^3}{p}\int_{-AB/2}^{AB/2}\frac{p_0^{sharp}}{\left[(x'-s)^2+z'^2\right]^2}ds - \frac{2z^2}{p}\int_{-AB/2}^{AB/2}\frac{q_0^{sharp}(x'-s)}{\left[(x'-s)^2+z'^2\right]^2}ds \qquad \textbf{Eq. 3-39}$$

$$t_{xz}^{*,sharp} = -\frac{2z^2}{p}\int_{-AB/2}^{AB/2}\frac{p_0^{sharp}(x'-s)}{\left[(x'-s)^2+z'^2\right]^2}ds - \frac{2z}{p}\int_{-AB/2}^{AB/2}\frac{q_0^{sharp}(x'-s)^2}{\left[(x'-s)^2+z'^2\right]^2}ds$$

It should be noticed that a different coordinate system is used (X', Z'). The coordinate system corresponds to the shear zone coordinate system as depicted in figure 3-10. In order to determine the total stress in the workpiece, the stress components with respect to the workpiece coordinates must be found (X, Z) in order to combine with the stresses due to the edge radius.

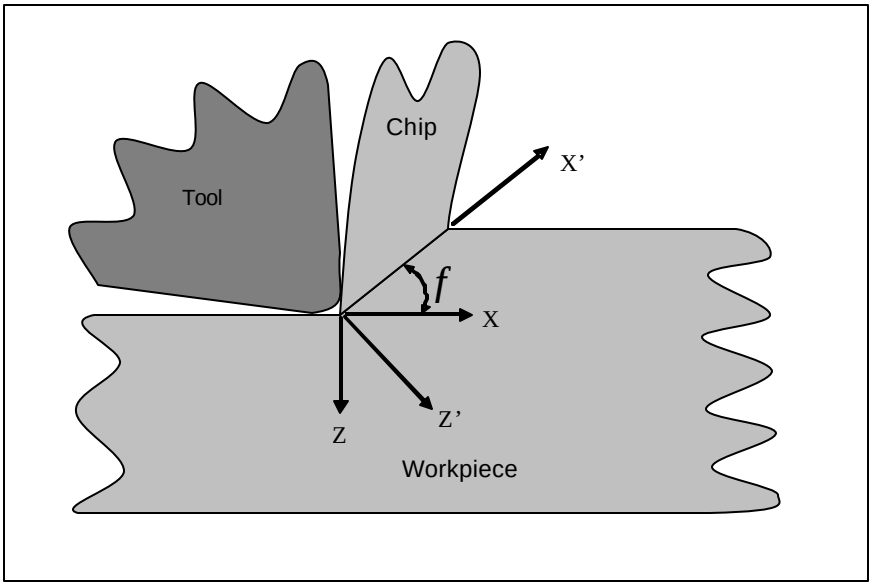

Figure 3-10 Coordinate system of the shear plane with respect to the workpiece

To do so, a rotation matrix is used to transform the stresses in the (X', Z') coordinate system to the (X-Z) coordinate system. The rotation matrix, Q, is given by:

$$[Q] = \begin{bmatrix} \cos f & \sin f \\ -\sin f & \cos f \end{bmatrix} \qquad \textbf{Eq. 3-40}$$

The stresses components from the shear zone expressed in the workpiece coordinate system are given by

$$\left[s_{shear\_X-Z} \right] = [Q] \begin{bmatrix} s_{X'} & t_{X'Z'} \\ t_{X'Z'} & s_{Z'} \end{bmatrix} \left[Q^T \right] \qquad \textbf{Eq. 3-41}$$

Using the principle of superposition, the stress history experienced by the workpiece due to a sliding cylinder is captured. A closer look at equations 3-38 and 3-39 reveals a singularity at the surface (z = 0). This singularity is dealt with by assuming that the stress field in the workpiece is continuous and that the stress field at the surface is the same at a depth dz into the workpiece. dz is equal to 0.1 micron.

3.3.2 Yield Surface and Plastic Strains

After determining the elastic stresses, the plastic stresses components need to be determined. First, the stress state at which plastic deformation or yielding at a point will occur needs to be established. The von Mises criterion will be used to establish the yield surface. Assuming an isotropic and homogeneous material, the yield function can be written mathematically in the form

$$F(s_{ij}) = J_2^{'} - R^2 = 0 \qquad \textbf{Eq. 3-42}$$

where $J_2^{'} = \frac{S_{ij}S_{ij}}{2}$ is the second invariant of the deviatoric stress tensor S_{ij}, and R is the uniaxial normalized radius of the yield surface.

In the case of elastic deformation, the following condition needs to be true: $F(s_{ij}) < 0$; during plastic deformation, $F(s_{ij}) \geq 0$ needs to hold true.

Including the kinematic hardening effect, the yield surface can be rewritten as follows

$$F = \frac{3}{2}\left(S_{ij} - a_{ij}\right)\left(S_{ij} - a_{ij}\right) - R^2 \qquad \textbf{Eq. 3-43}$$

where $S_{ij} = s_{ij} - \left(s_{kk}/3\right)d_{ij}$ is the deviatoric stress tensor, a_{ij} is the backstress tensor which geometrically represents the center of the yield surface.

After establishing the yield surface, the plastic strains need to be found. As it has been established, plastic deformation is associated with the dissipation of energy so that it is irreversible, and the deformation process is history or path dependent. Due to its path dependent nature, the constitutive equations for plastic deformation must be in

differential equation or incremental form. The incremental plastic strains throughout the deformation history have to be calculated and accumulated to determine the total plastic strains[82].

Researchers have developed constitutive equations or plastic flow rule to determine plastic deformation[82]. The plastic flow rule considered in this work is given by the following equation

$$\dot{e}_{ij}^{p} = \frac{1}{h}\left\langle \dot{S}_{mn} n_{mn} \right\rangle n_{ij} \qquad \textbf{Eq. 3-44}$$

with $n_{ij} = \sqrt{(3/2)\left(S_{ij} - a_{ij}\right)/R}$ which are non-zero components of the unit vector in the plastic strain rate direction; h is the plastic modulus which determines the rate of material hardening; the bracket used in equation 3-44 is the MacCauley bracket defined as $\langle x \rangle = 0.5(x + |x|)$.

3.4 Residual stress modeling

Now that the plastic strains are found with the previous equations, the plastic stresses and ultimately the residual stresses need to be determined. The hybrid algorithm proposed by McDowell [83] is well suited to predicting residual stresses from the elastic stress fields generated through rolling or sliding contact. This algorithm combines attractive features of previous rolling/sliding contact models [84], [85], enabling a stable prediction of residual stresses and subsurface plasticity over a range of loading conditions ranging from small to large plastic-strain ranges. This fusion of these models is done by using a blending function Y. The mathematical expression for this function is as follows

$$\Psi = 1 - \exp\left(- k \frac{3}{2} \frac{h}{G} \right) \qquad \textbf{Eq. 3-45}$$

where G=E/(2(1+v)) is the elastic shear modulus; k is a constant.

Y approaches zero as h approaches zero in the case of perfectly plastic behavior of the material. Y tends toward unity as h approaches infinity in the case of initial yielding.

For this hybrid algorithm neither the assumption of zero strain rate in the cutting direction $\dot{e}_{xx} = 0$ [86] nor the assumption of elastic stress in the cutting direction $\dot{s}_{xx} = \dot{s}^{*}_{xx}$ [84] are assumed during plastic flow. The blending function is used to impose a sliding/cutting direction strain rate according to

$$\begin{aligned} \dot{e}_{xx} &= \frac{1}{E}\left[\dot{s}_{xx} - n\left(\dot{s}_{yy} + \dot{s}^{*}_{zz} \right) \right] + a\Delta T + \frac{1}{h}\left(\dot{s}_{xx} n_{xx} + \dot{s}_{yy} n_{yy} + \dot{s}^{*}_{zz} n_{zz} + 2\dot{t}^{*}_{xz} n_{xz} \right) n_{xx} \\ &= \Psi\left(\frac{1}{E}\left[\dot{s}^{*}_{xx} - n\left(\dot{s}_{yy} + \dot{s}^{*}_{zz} \right) \right] + a\Delta T + \frac{1}{h}\left(\dot{s}^{*}_{xx} n_{xx} + \dot{s}_{yy} n_{yy} + \dot{s}^{*}_{zz} n_{zz} + 2\dot{t}^{*}_{xz} n_{xz} \right) n_{xx} \right) \end{aligned} \qquad \textbf{Eq. 3-46}$$

The plane-strain condition assumed requires the strain rate in the transverse direction to be equal to zero. This condition is represented by the following equation:

$$\dot{e}_{yy} = \frac{1}{E}\left[\dot{s}_{yy} - n\left(\dot{s}_{xx} + \dot{s}^{*}_{zz} \right) \right] + a\Delta T + \frac{1}{h}\left(\dot{s}_{xx} n_{xx} + \dot{s}_{yy} n_{yy} + \dot{s}^{*}_{zz} n_{zz} + 2\dot{t}^{*}_{xz} n_{xz} \right) n_{yy} = 0 \qquad \textbf{Eq. 3-47}$$

The above expressions are solved simultaneously for plastic stress increments in the sliding/cutting and the transverse directions, $\dot{s}_{xx}, \dot{s}_{yy}$.

For the elastic case, $\dot{s}_{xx} = \dot{s}^{*}_{xx}; \dot{s}_{yy} = u\left(\dot{s}^{*}_{xx} + \dot{s}^{*}_{zz} \right)$, are employed as consistent limiting cases of the two previous equations as $h \to \infty$ in agreement with the elastic Hertzian solution for plane-strain conditions.

As the cylinder slides over the semi infinite plane, no effort is made to maintain equilibrium. After the passage of the cylinder, a relaxation scheme is introduced in order for the residual stresses and strains to satisfy the boundary conditions prescribed by Mervin and Johnson[20]. These conditions are presented in following set of equations

$$\begin{array}{cccc} (e_{xx})_r = 0 & (s_{xx})_r = f_1(z) & (e_{yy})_r = 0 & (s_{yy})_r = f_2(z) \\ (e_{zz})_r = f_3(z) & (s_{zz})_r = 0 & (g_{xz})_r = f_4(z) & (t_{xz})_r = 0 \end{array} \qquad \textbf{Eq. 3-48}$$

Any non-zero components s_{zz}^R, t_{xz}^R, e_{xx}^R, and T^R are incrementally relaxed until the boundary conditions are met. If M steps are used for the relaxation process, then the stress increments are

$$\Delta s_{zz} = -\frac{s_{zz}^R}{M}, \qquad \Delta t_{xz} = -\frac{t_{xz}^R}{M}, \qquad \Delta e_{xx} = -\frac{e_{xx}^R}{M}, \qquad \Delta T = -\frac{T^R}{M} \quad .$$

At the end of the relaxation procedure, both s_{xx} and s_{yy} will be non-zero. These values are the true residual stresses that remain in the body.

During relaxation, there are two possibilities for material behavior: purely elastic relaxation and elastic-plastic relaxation. For purely elastic relaxation, $F < 0$. The elastic relaxation increments for s_{xx} and s_{yy} are given by equation 3-49

$$\begin{aligned} \Delta s_{xx} &= \frac{-\left(\frac{s_{zz}^R}{M}\right)u(1+u) - E\left(\frac{e_{xx}^R}{M}\right)}{(1-n^2)} \\ \Delta s_{yy} &= u\Delta s_{xx} - u\left(\frac{s_{zz}^R}{M}\right) \end{aligned} \qquad \textbf{Eq. 3-49}$$

For elastic-plastic relaxation $F = 0$ and $dS_{ij}n_{ij} \geq 0$, the plastic relaxation increments are given by

$$\Delta s_{yy} = \frac{\left(-\frac{u}{E} + \frac{n_{xx} n_{yy}}{h}\right) C - \left(\frac{1}{E} + \frac{n_{xx}^2}{h}\right) D}{\left[\left(-\frac{u}{E} + \frac{n_{xx} n_{yy}}{h}\right)^2 - \left(\frac{1}{E} + \frac{n_{xx}^2}{h}\right)\left(\frac{1}{E} + \frac{n_{yy}^2}{h}\right)\right]}$$

Eq. 3-50

$$\Delta s_{xx} = \frac{D - \left(\frac{1}{E} + \frac{n_{yy}^2}{h}\right) \Delta s_{yy}}{\left(-\frac{u}{E} + n_{xx} \frac{n_{yy}}{h}\right)}$$

Where C and D are given by the following expressions

$$C = -\frac{e_{xx}^R}{M} - \frac{s_{zz}^R}{M} \frac{u}{E} + \frac{1}{h} \frac{s_{zz}^R}{M} n_{zz} n_{xx} + \frac{2}{h} \frac{t_{xz}^R}{M} n_{xz} n_{xx}$$

Eq. 3-51

$$D = \frac{-u}{E} \frac{s_{zz}^R}{M} + \frac{1}{h} \frac{s_{zz}^R}{M} n_{yy} n_{zz} + \frac{2}{h} \frac{t_{xz}^R}{M} n_{xz} n_{yy}$$

3.5 Summary

In this chapter, a first principle based model of cutting force and an analytical approach to estimating residual stresses during machining were presented. These methods constitute the base for developing an inverse method to estimate cutting and tool geometry parameters from desired or required residual stresses in a machined component

****

CHAPTER 4

REVERSE METHODOLOGY

The reverse methodology in this work will consist of obtaining the depth of cut and edge radius of the tool from a given or required surface residual stresses in a workpiece. The inverse solutions to the methods presented thus far for modeling residual stress in the workpiece will be developed.

The following figure shows the flowchart of the methodology. The inputs to the model are the residual stress information at the surface and the tool & workpiece material properties. Using these inputs, the tractions that would have led to the input residual stresses are calculated. The method that enables such calculation will be discussed in section 4.2. From the stresses calculated, the depth of cut is estimated using the method that will be presented in section 4.3. In section 4.4, the shear zone characteristics are found through an inverse method based on force equilibrium. Utilizing the depth of cut and the shear zone charateristics, the hone radius is estimated through an inverse method based on the slip-line model. This will be discussed in section 4.5.

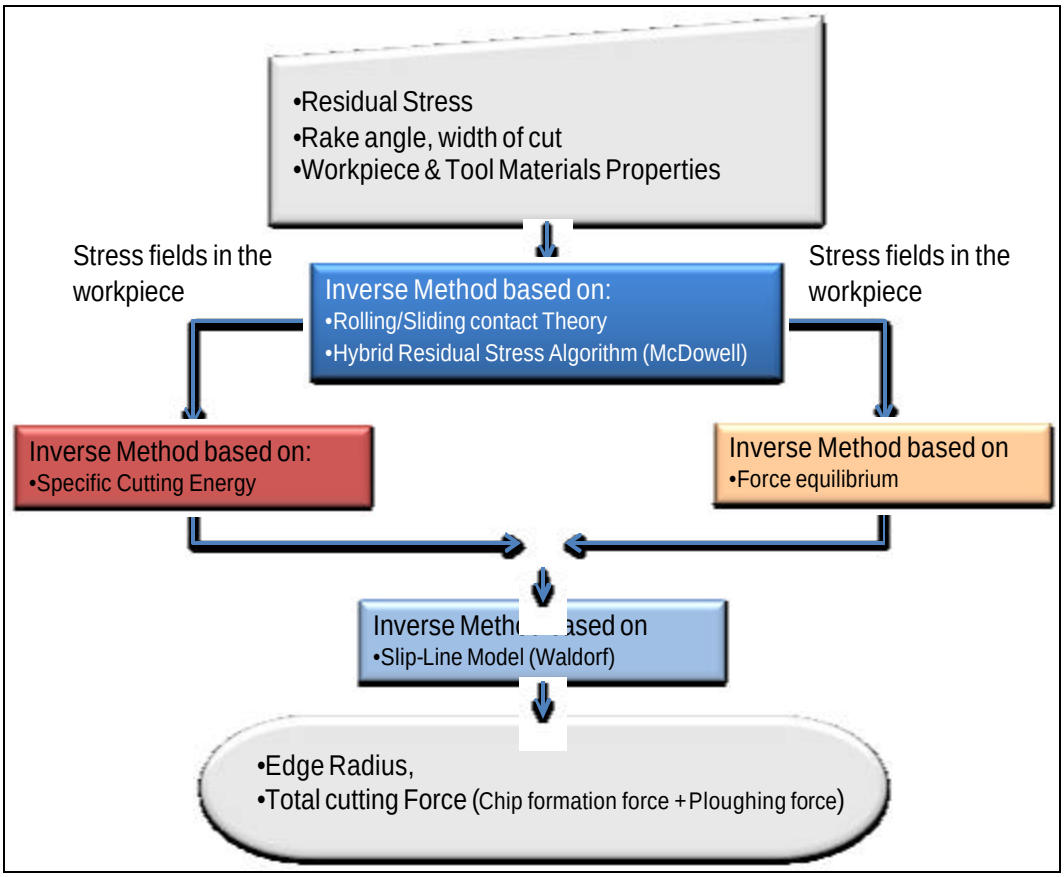

Figure 4-1 Reverse Methodology to estimate process parameters from residual stress

4.1 Interpretation of the Residual Stress Profile

Before explaining the methodology where residual stresses are used to predict process parameters, interpretation of the residual stress profile is presented in this section. As mentioned previously, Jacobus [18] presented an approach to understanding the residual stress profile produced in machining. An overview of Jacobus's descriptive model is provided for that purpose. Further, the model will help explain some the assumptions and reasoning behind the reverse model developed.

Jacobus suggested that the workpiece is comprised of distinct layers as shown in figure 4.2. Layer *S* corresponds to the surface and near-surface layers of the workpiece where both thermal and mechanical effects are significant. Layer *D* represents the region

where only mechanical loads are significant. Layer *B* represents the remainder of the workpiece where residual stress magnitudes are negligible.

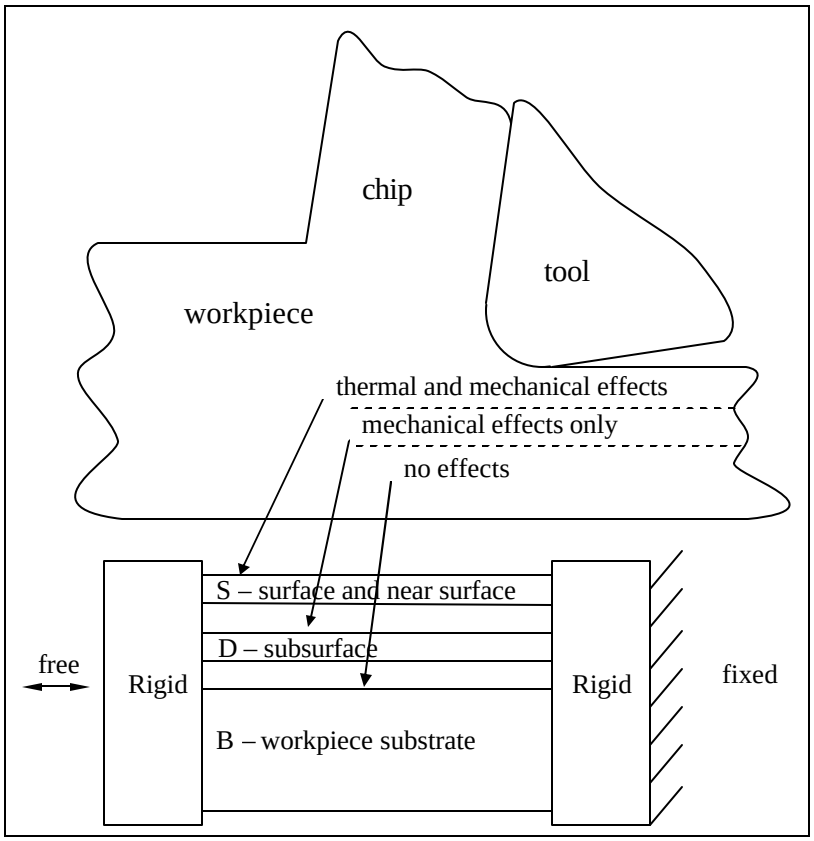

Figure 4-2 Adapted from Jacobus [18]. Schematic for development of machining-induced residual stress

In modeling the elastic constraint imposed on each layer by its neighbors, rigid supports are fixed to the end of each of the layers, with one rigid support fixed and the other free to translate. The total strain in the *S* layer is the sum of elastic strain e_S^E, plastic strain e_S^P, and thermal strain e_S^T.

$$e_S = e_S^E + e_S^P + e_S^T \qquad \textbf{Eq. 4-1}$$

In a similar vein, the total strain in layer *D* where only mechanical effects are significant may be written as the sum of elastic and plastic components.

$$e_D = e_D^E + e_D^P \qquad \textbf{Eq. 4-2}$$

The strain in the workpiece substrate is purely elastic and is given by:

$$e_B = e_B^E \qquad \textbf{Eq. 4-3}$$

The constraints require that the total strains be equal in each of the layers.

$$e_S = e_D = e_B \qquad \textbf{Eq. 4-4}$$

Equilibrium of the structure without external loading is given by

$$s_S d_S + s_D d_D + s_B d_B = 0 \qquad \textbf{Eq. 4-5}$$

where d_S is the thickness of the surface/near-surface layer, d_D is the thickness of the sub-surface layer, and d_B is the thickness of the bulk of the workpiece. After the workpiece has cooled, the thermal strain e_S^T will be zero. Equation 4-4 can then be re-written as

$$\frac{s_S^r}{E} + e_S^P = \frac{s_D^r}{E} + e_D^P = \frac{s_B^r}{E} \qquad \textbf{Eq. 4-6}$$

where the superscript r indicates residual stresses. Simultaneous consideration of compatibility and equilibrium results in the expression for residual stresses in the surface/near-surface layer.

$$s_S^r = -Ee_S^P \frac{d_D + d_B}{d_S + d_D + d_B} + Ee_D^P \frac{d_D}{d_S + d_D + d_B} \qquad \textbf{Eq. 4-7}$$

For conditions where the bulk of the workpiece is much larger than the residual stressed zones, ($d_S << d_B$ and $d_D << d_B$), Equation 4-7 can be approximated by

$$s_S^r \approx -Ee_S^P \qquad \textbf{Eq. 4-8}$$

Similarly, expressions for residual stresses in the sub-surface and bulk layer are approximated by equation 4-9 and 4-10, respectively.

$$s_D^r \approx -Ee_D^P \qquad \textbf{Eq. 4-9}$$

$$s_B^r \approx 0 \qquad \textbf{Eq. 4-10}$$

During the cutting process, thermal and plastic strains exist in the surface/near-surface layer. If the elastic strains in the surface/near-surface and sub-surface layers are of similar value, then

$$e_S^P = e_D^P - e_S^T \qquad \textbf{Eq. 4-11}$$

Since the temperature always increases in the workpiece as a result of cutting, the thermal strains in the surface/near-surface layer are non-negative. Assuming the flow of material around the tool is continuous the far-field boundary conditions require that $\left|e_S^P\right| \geq \left|e_D^P\right| \geq 0$ in the absence of thermal effects. Another explanation for this condition is that the magnitude of the sub-surface plastic strain is always greater than or equal to that of the surface/near-surface plastic strain.

Jacobus proposed the following scenarios that are possible for machining-induced residual stress.

- Case 1: $e_D^P > e_S^T \geq 0$. From the compatibility condition in Equation 4.11 and considering thermal strains are non-negative, $e_S^P > 0$. Consequently, the surface/near-surface residual stress $s_S^r < 0$. For the sub-surface layer, the residual stress is $s_D^r < 0$. The results are shown in figure 4.3.
- Case 2: $e_S^T > e_D^P > 0$. From the compatibility condition, $e_S^P < 0$. Therefore, the surface/near-surface residual stress $s_S^r > 0$. The residual stress in the subsurface $s_D^r < 0$. This condition results in tensile residual stresses near the surface and compressive in the sub-surface. The residual stress profile is illustrated in figure 4.3.

- Case 3: $e_D^P < 0$. This condition results in $e_S^P \le e_D^P < 0$ and residual stresses $s_S^r \ge s_D^r > 0$. The residual stresses in all the layers are tensile. The profile is provided in figure 4.3

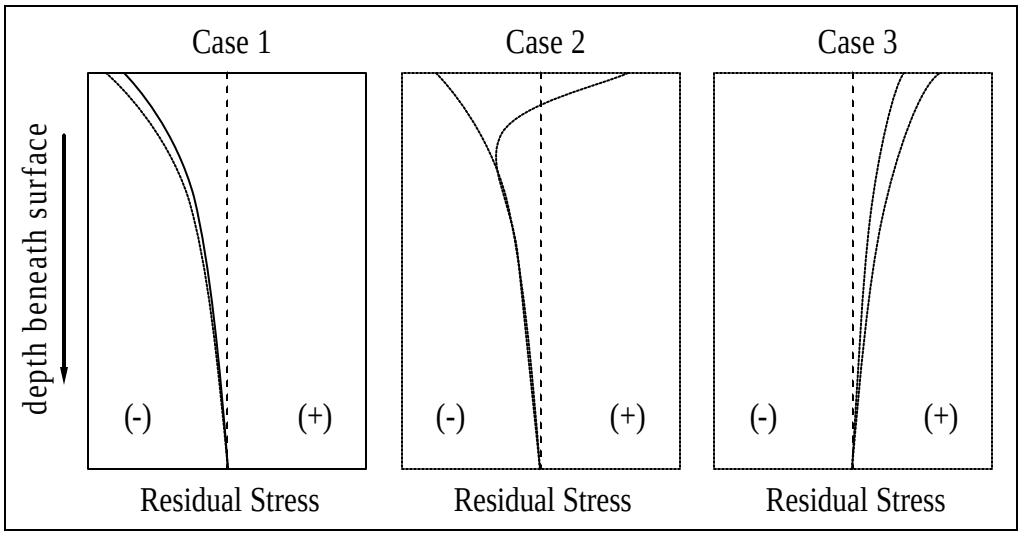

Figure 4-3 Adapted from Jacobus [18]. Possible residual stress fields from one-dimensional model. Dotted lines indicate residual stresses from purely mechanical loads. Solid lines indicate residual stresses from combined thermal and mechanical effects.

The modeling proposed by Jacobus and referenced here provides a quantitative rationale for the potential residual stress profiles generated by machining in the cutting direction. When coupling the effects of plastic and thermal strains, the temperature increases are shown to increase the tensile character of the residual stress profile, which is consistent with published experimental data.

4.2 Inverse method for stress history in the workpiece

Several challenges arise when dealing with residual stress which is caused mainly by plastic deformation. As mentioned, plastic deformation is associated with the dissipation of energy so that it is irreversible and the deformation process is history or

path dependent. Nonetheless, one needs to establish a procedure to recapture the stress history that would have led to the residual stress profile in the workpiece.

Looking at the preceding chapters, the task seems to be impossible if the strategy is to simply navigate back through the numerous equations presented. A lot of information is lost through maintaining equilibrium, boundary conditions and going through the relaxation procedure. In order to find a way to determine the stress history, the stress history dependence of residual stress needs to be explored a bit further.

4.2.1 Stress history dependence

Due the nature of plastic deformation, there will not be a one-to-one correspondence between stress and strain during plastic deformation. Figure 4-4 shows a stress-strain curve during uni-axial loading and unloading of material.

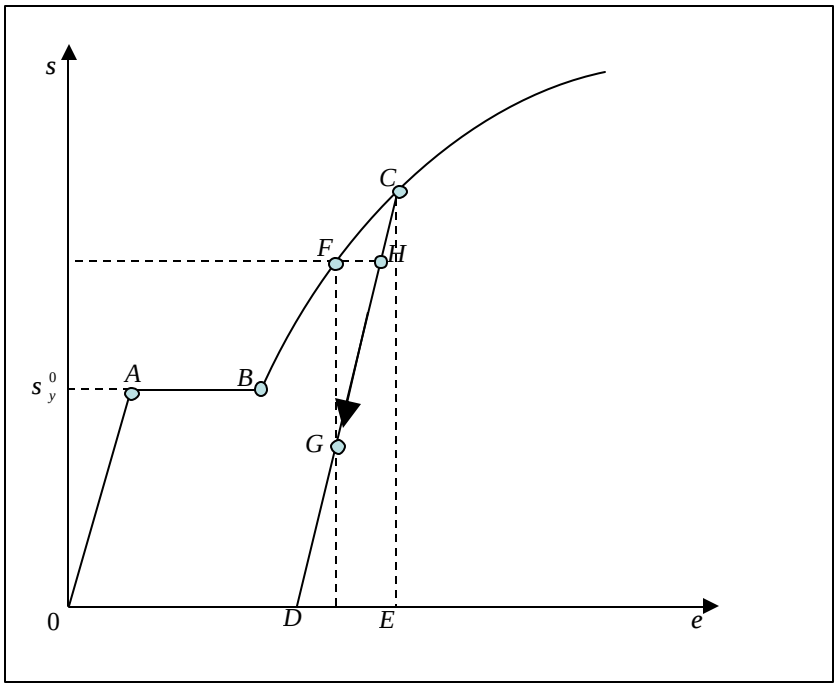

Figure 4-4 Uniaxial stress-strain curve

In this figure, the points F and H have the same stress level but different strains. On the other hand, the strains at points F and G are the same, but the stresses are different. Evidently, these differences result from different deformation histories or stress paths between points F and H, and F and G. To further explore the history dependent nature of plastic deformation, let us consider the following example taken from Khan[82]:

Suppose that a specimen is loaded with uniaxial tension in the x direction. It deforms elastically until the stress reaches point B on the initial yield surface shown in figure 4-5. If the stress is increased to point A, the material of the specimen will deform elasto-plastically, and the yield surface will expand to become the subsequent yield surface due to the hardening behavior of the materials.

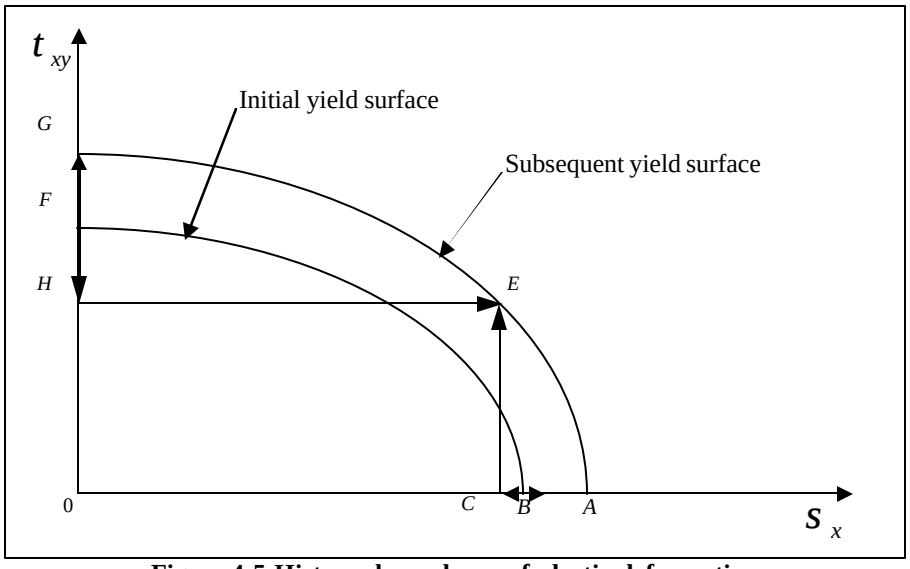

Figure 4-5 History dependence of plastic deformation

With the assumption of isotropic hardening, the strain state at point A is given by

$$e_{xx}^{p} = e^{p} \qquad \textbf{Eq. 4-12}$$

where e^p is the plastic strain along the x axis at point A. Due to the assumption of incompressibility of plastic deformation, it follows that

$$e_{yy}^p = e_{zz}^p = -\frac{1}{2}e^p \qquad \textbf{Eq. 4-13}$$

$$g_{xy}^p = g_{yz}^p = g_{zx}^p = 0 \qquad \textbf{Eq. 4-14}$$

where g_{ij} represents twice the shear component of the infinitesimal strain tensor e.

Now unload the specimen from point A to point C, keep the axial force constant, and apply the shear stress t_{xy} at the same time until point E is reached on the subsequent yield surface. During this process following the A-C-E, the material behaves elastically because this path is inside the subsequent yield surface which is also the current yield surface. Therefore no further plastic deformation occurs when the stress state of the specimen changes from A to E following A-C-E. The plastic strains at point E can still be represented by equations 4-12, 4-13, and 4-14.

Now consider another loading history. Let the specimen be loaded by pure shear with shear stress t_{xy}. The elastic deformation continues until the initial yielding at point F. Then plastic deformation will result with increasing t_{xy}. The yield surface will expand at the same time. Suppose that the shear stress t_{xy} is increased until point G on the subsequent yield surface, which also contains point A and E from the previous loading history. Denote the plastic shear strain at point G by g^p; then the plastic strains at point G are given by

$$g_{xy}^p = g^p \qquad \textbf{Eq. 4-15}$$

$$g_{yz}^p = g_{zx}^p = 0 \qquad \textbf{Eq. 4-16}$$

$$e_{xx}^{p} = e_{yy}^{p} = e_{zz}^{p} = 0 \qquad \textbf{Eq. 4-17}$$

The specimen is then unloaded from point G to point H, and the shear stress t_{xy} is kept constant while the axial load is applied and increased to bring the stress state of the specimen to point E on the subsequent yield surface. Since the path G-H-E is inside the current yield surface AEG, the material deforms elastically, and no additional plastic deformation occurs following the stress path G-H-E. The plastic strains at point E are also given by 4-15, 4-16, and 4-17. Obviously the plastic strains represented by the aforementioned equations, which are the results of the stress path O-G-H-E, are completely different from those given by equations 4-12 to 4-14, which are obtained by a different stress path O-A-C-E. Plastic deformation is indeed a history or path dependent process.

4.2.2 Inverse method based on rolling/sliding contact theory and McDowell algorithm: recapturing the stress field.

The path dependent nature of plastic deformation shows that there is more than one path that could lead to the same stress level. In other words, there is a family of loading paths or stress histories that would lead to the same amount of plastic deformation and residual stress. This non-uniqueness characteristic of the stress can help when the stress history needs to be recaptured. The term "recapturing" means finding one of the loading paths belonging to the family of solutions.

As discussed in chapter 3, the algorithm developed by McDowell is used to predict residual stresses from the stress history experienced by the workpiece. This hybrid algorithm combines attractive features of previous rolling/sliding models, enabling

a stable prediction of residual stresses and subsurface plasticity over a range of loading conditions ranging from small to large plastic strain ranges. The robustness of this algorithm makes it a useful tool to help determine a stress history that would have led to a predetermined residual stress profile.

As the cylinder slides on the surface of the workpiece, the stress components $s^*_{xx}(z_i), s^*_{zz}(z_i), t^*_{xz}(z_i), s^*_{yy}(z_i) = u\left(s^*_{xx}(z_i) + s^*_{zz}(z_i)\right)$ at point $A\left(x_j, z_i\right)$ of the workpiece will change as shown in figure 4-6 to 4-9. Theses stresses are due to the combination of the normal and shear load generated by the cylinder. To generate these plots a radius of 0.025mm was used. It should be noted that the similar stress profiles are obtained when the radius is changed. Further, these plots shown are a representation of the stress components history so and the stress values do not have a meaning here. The workpiece region of interest was discretized into a 2000 unit in the x-direction (cutting diretion) and 16 unit in the z-direction (ploughing direction). Thus, $j = 0....n, where n = 2000$ and $i = 0....m, where m = 16$.

Evidently, the stress components at every point with the same z coordinate will experience the same change in values. When the tool tip is far away from the point of interest, the stress components values are essentially zero. As the tool gets closer, the value of each component increases. For the normal stress components, $s^*_{xx}(z_i), s^*_{zz}(z_i)$ the stress values reach a maximum when the tool is directly under the point of interest. The shear component value changes from zero to positive maximum, then goes to a negative maximum as the tool is near the point of interest.

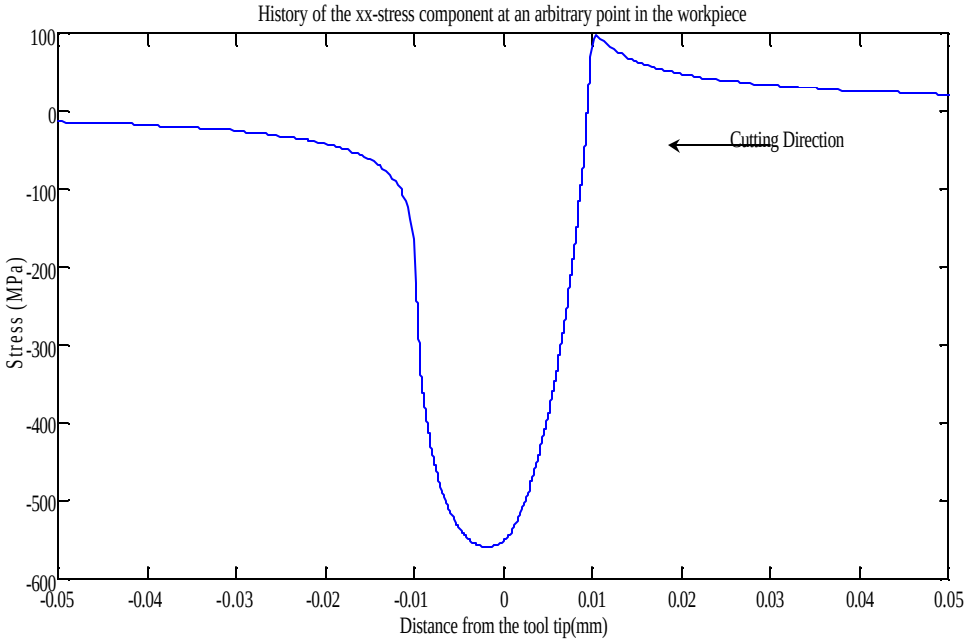

Figure 4-6 History of the normal stress component in the x-direction at an arbitrary point of the workpiece.

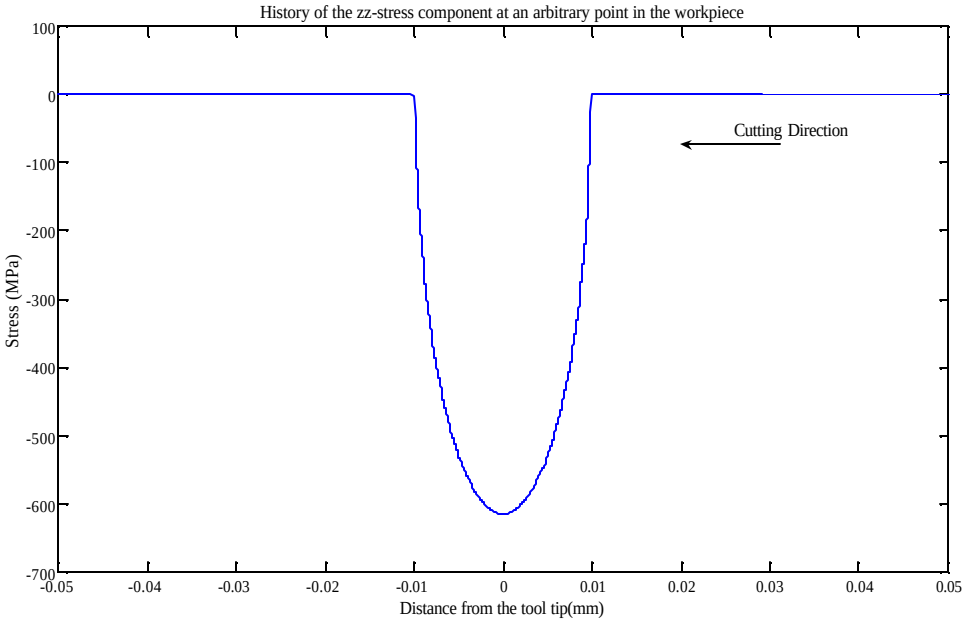

Figure 4-7 History of the normal stress component in the z direction at an arbitrary point of the workpiece

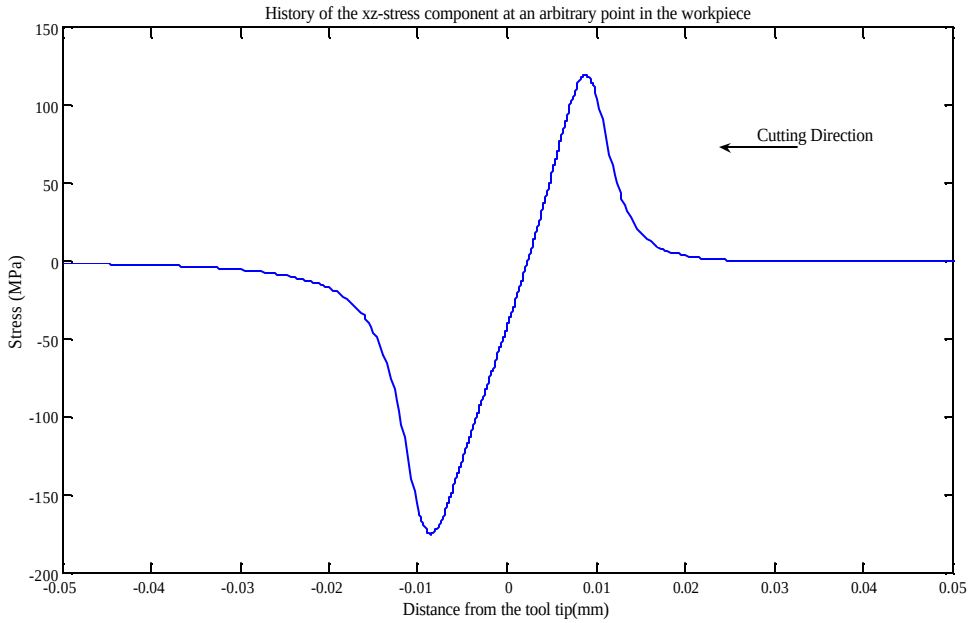

Figure 4-8 History of the shear stress component in the x-z direction at an arbitrary point of the workpiece

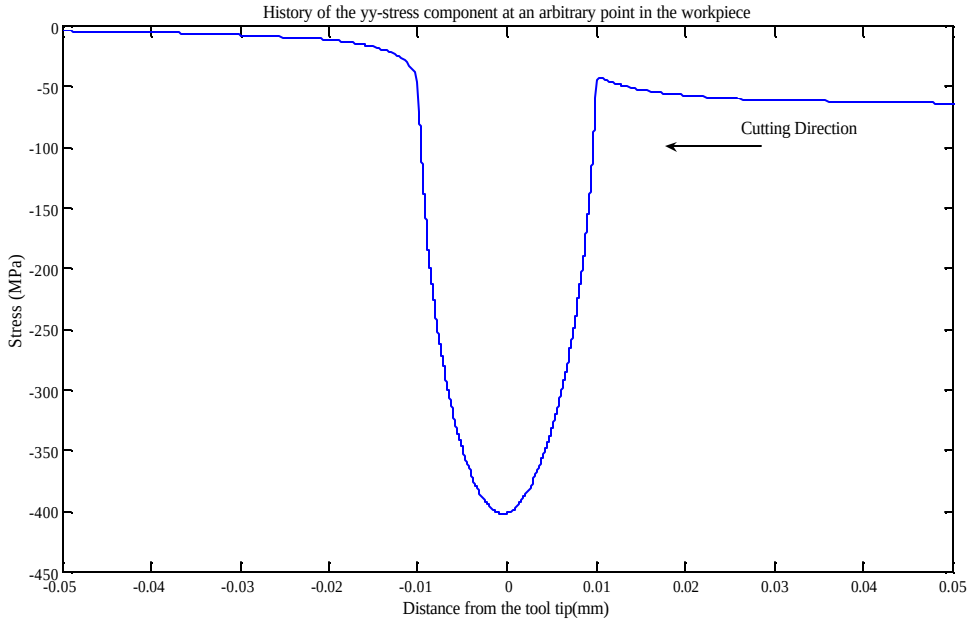

Figure 4-9 History of the normal stress component in the y direction at an arbitrary point of the workpiece

From the history of the stress components at each point $A_i(x_0, z_i), i = 0...n$ located along the depth of the workpiece, the residual stresses in the cutting and transverse directions are determined using the hybrid algorithm. The exact calculations were presented earlier in section 3-4. Figure 4-10 shows a typical plot of residual stress versus depth into the workpiece. The residual stress profiles in the cutting (xx) and transverse (yy) direction are shown. These curves follow the behavior of the residual stresses measured by Jacobus[18].

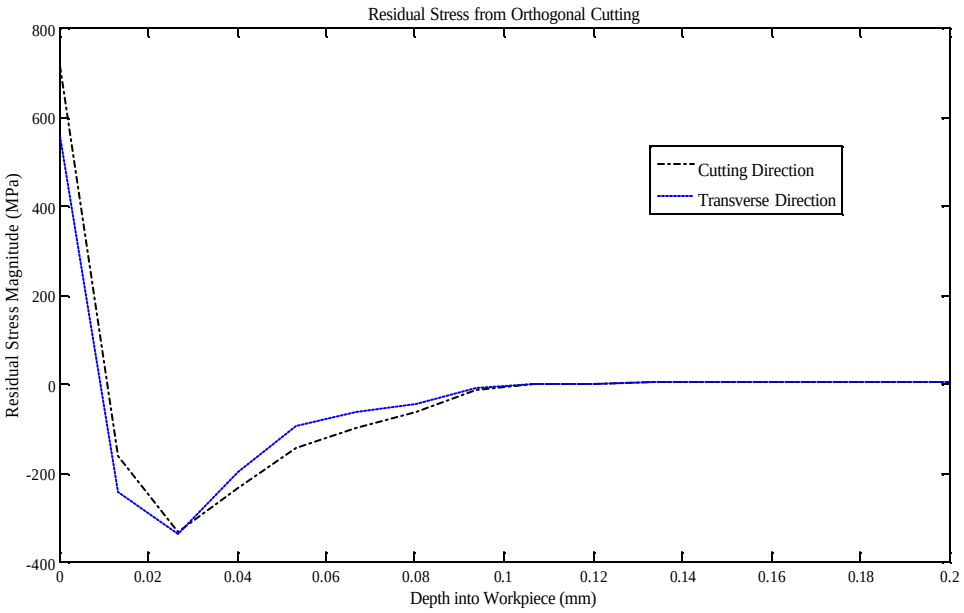

Figure 4-10 Typical residual stress plot for an orthogonal cutting operation

Figure 4.11 shows a simplified chart of the overall process in determining the residual stress from the history of the elastic or hertzian stress components at each point of the workpiece. As one can see, there are more inputs to the algorithm than there are outputs. Although four inputs and 2 outputs are shown, a closer look at the figure reveals that

there are more than four inputs. To estimate the residual stress components s^{r}_{xx}, s^{r}_{yy} at depth z_i, a total of 3*2000 data points need to be estimated to recapture the stress components $s^{*}_{xx}(z_i), s^{*}_{zz}(z_i), t^{*}_{xz}(z_i)$. This represents a major challenge

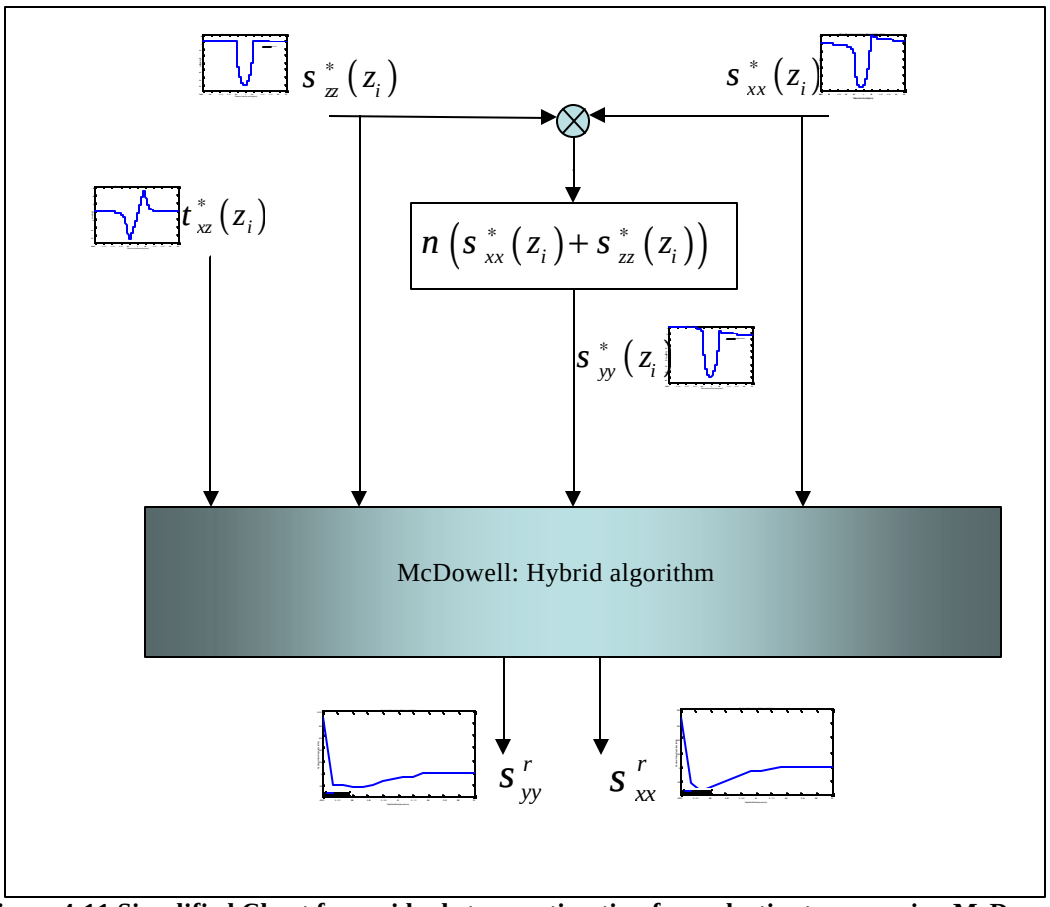

Figure 4-11 Simplified Chart for residual stress estimation from elastic stresses using McDowell algorithm.

To overcome this obstacle, simpler relations or correlations between critical features of the stress history and the residual stresses components need to be established. The contour plot of the second stress invariant $J_2^{'}$ of the stresses at point $A(x,z)$ for a typical orthogonal cutting process is shown in figure 4.12. Looking at the plot, the region of high deviatoric stresses or plastic stresses is in a small region near the tool tip and the near-surface region of the workpiece. Thus, a simpler correlation could be achieved

between the maximum values of the stress components and the residual stress at the surface.

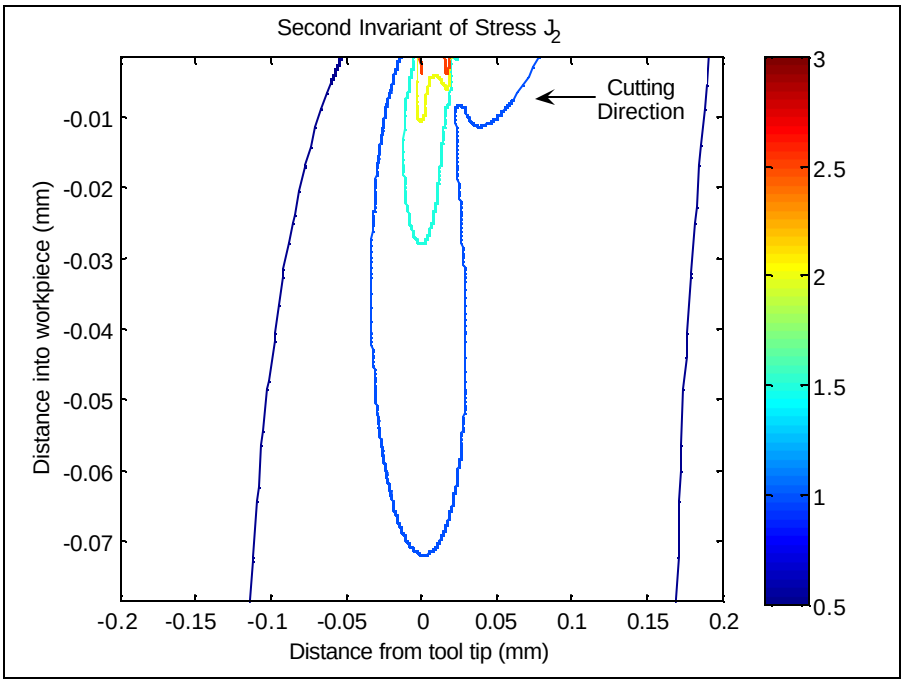

Figure 4-12 Contour plot of the second invariant of stresses (J2) for an orthogonal cutting process obtained using depth of cut of 0.1mm, edge radius of 0.025mm, width of cut of 3mm, speed of 5m/s

Furthermore, during an orthogonal machine operation, the bulk of the workpiece is much larger than the residual stressed zone. According to equation 4-8, a linear relationship between the residual stress and the plastic strain can be approximated at the surface and near surface region. By the same token, correlation between the residual stress and the maximum stresses will be assumed to be linear.

For a given workpiece and tool materials, 7 sets of elastic stress $s^*_{xx}(z_i), s^*_{zz}(z_i), t^*_{xz}(z_i), s^*_{yy}(z_i) = u\left(s^*_{xx}(z_i) + s^*_{zz}(z_i)\right)$ histories were used in order to obtain a variety of residual stress profile in a workpiece. These histories are similar to the profiles depicted in figures 4-6 to 4-9. The 7 sets are generated using the factor ? in

table 4-1. The first set was chosen to give a residual stress profile that would be seen due to an actual orthogonal cutting operation. The residual stress profile was matched to an experimental plot obtained by Jacobus after measuring residual stresses after an orthogonal machining operation [18].

Once this set is chosen, the other sets were generated by scaling the first set in order to generate residual stress profiles ranging from a constant zero value to an ever increasing value of residual stresses as the depth into the workpiece increases. The two extremes cases of residual stress profiles for an orthogonal cutting are depicted in figures 4-13 and 4-14 which correspond to sets 2 and 7. The residual stresses versus the depth into the workpiece in the cutting or x-direction and the transverse or y-direction are depicted in these figures.

Table 4-1 History of the stress components used to obtain residual stress profiles

Set #	Stress History all z values	Factor: ?
1	$\Lambda s^*_{xx}(z_i), \Lambda s^*_{zz}(z_i), \Lambda t^*_{xz}(z_i), \Lambda s^*_{yy}(z_i) = \Lambda u\left(s^*_{xx}(z_i) + s^*_{zz}(z_i)\right)$	1
2	$\Lambda s^*_{xx}(z_i), \Lambda s^*_{zz}(z_i), \Lambda t^*_{xz}(z_i), \Lambda s^*_{yy}(z_i) = \Lambda u\left(s^*_{xx}(z_i) + s^*_{zz}(z_i)\right)$	0.25
3	$\Lambda s^*_{xx}(z_i), \Lambda s^*_{zz}(z_i), \Lambda t^*_{xz}(z_i), \Lambda s^*_{yy}(z_i) = \Lambda u\left(s^*_{xx}(z_i) + s^*_{zz}(z_i)\right)$	0.5
4	$\Lambda s^*_{xx}(z_i), \Lambda s^*_{zz}(z_i), \Lambda t^*_{xz}(z_i), \Lambda s^*_{yy}(z_i) = \Lambda u\left(s^*_{xx}(z_i) + s^*_{zz}(z_i)\right)$	1.5
5	$\Lambda s^*_{xx}(z_i), \Lambda s^*_{zz}(z_i), \Lambda t^*_{xz}(z_i), \Lambda s^*_{yy}(z_i) = \Lambda u\left(s^*_{xx}(z_i) + s^*_{zz}(z_i)\right)$	2
6	$\Lambda s^*_{xx}(z_i), \Lambda s^*_{zz}(z_i), \Lambda t^*_{xz}(z_i), \Lambda s^*_{yy}(z_i) = \Lambda u\left(s^*_{xx}(z_i) + s^*_{zz}(z_i)\right)$	2.5
7	$\Lambda s^*_{xx}(z_i), \Lambda s^*_{zz}(z_i), \Lambda t^*_{xz}(z_i), \Lambda s^*_{yy}(z_i) = \Lambda u\left(s^*_{xx}(z_i) + s^*_{zz}(z_i)\right)$	3

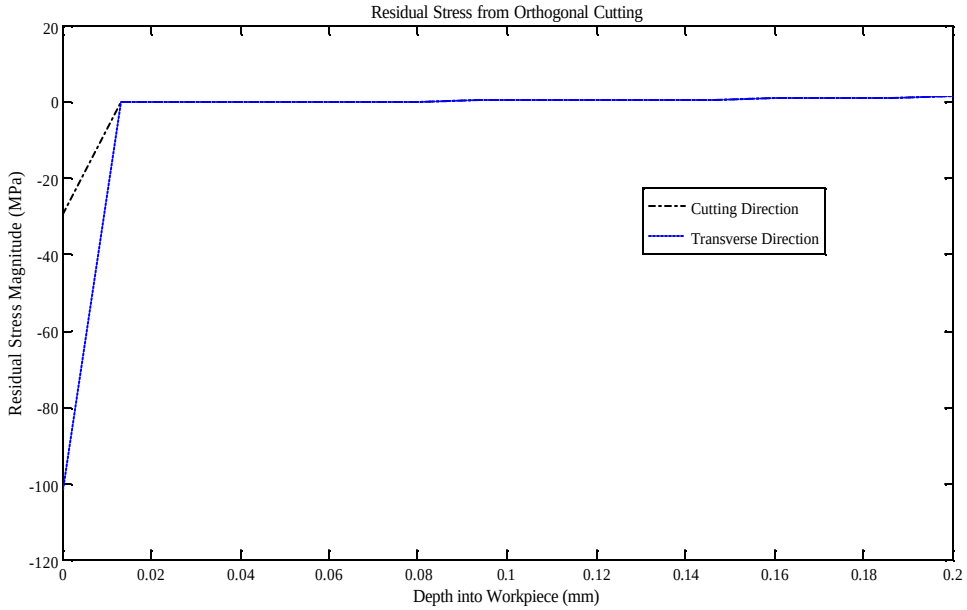

Figure 4-13 Residual stress profiles in the cutting and transverse directions for case 2

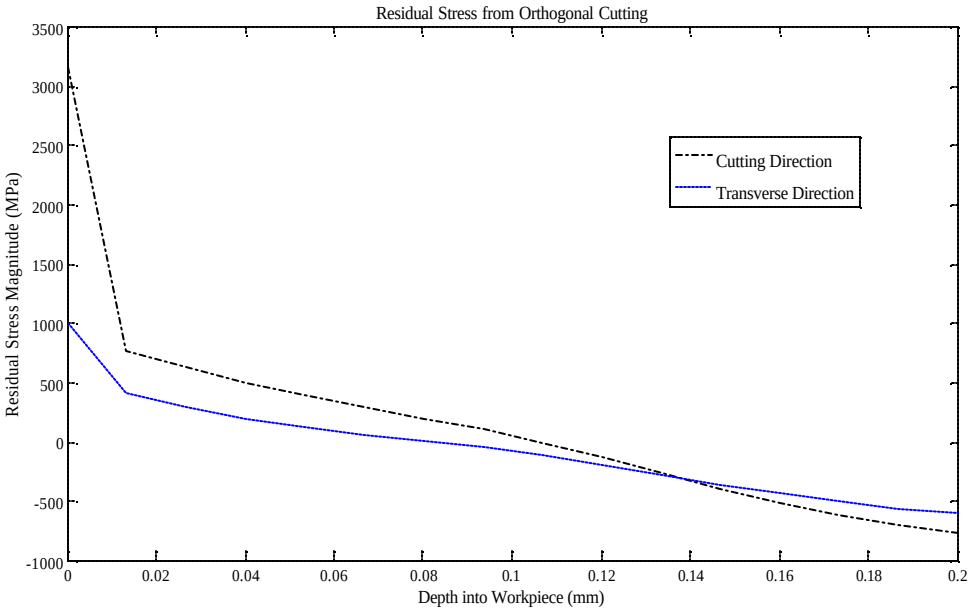

Figure 4-14 Residual stress profiles in the cutting and transverse directions for case 7

Using a commercial statistical software, MINITAB 14, a multiple regression is performed to obtain a relation between the residual stress components and the maximum elastic stress component values for each unit depth (z_i). The relations are expressed by the following equations:

$$s^{*}_{xx,\max}(z_i) = A_i + B_i s^{r}_{xx}(z_i) + C_i s^{r}_{yy}(z_i) \quad \textbf{Eq. 4-18}$$

$$s^{*}_{zz,\max}(z_i) = D_i + E_i s^{r}_{xx}(z_i) + F_i s^{r}_{yy}(z_i) \quad \textbf{Eq. 4-19}$$

$$t^{*}_{xz,\max}(z_i) = G_i + H_i s^{r}_{xx}(z_i) + L_i s^{r}_{yy}(z_i) \quad \textbf{Eq. 4-20}$$

$$s^{*}_{yy,\max}(z_i) = u(s^{*}_{xx,\max}(z_i) + s^{*}_{zz,\max}(z_i)) \quad \textbf{Eq. 4-21}$$

The elastic stresses in the y-direction or transverse direction are obtained from the plane strain assumption. The terms $A_i, B_i, C_i, D_i, E_i, F_i, G_i, H_i, L_i$ are constants obtained from the regression analysis. Evidently, a lot of relations were obtained since $i = 0...15$. However, the correlations between the surface components are emphasized since the performance of the part is directly affected by the residual stresses at the surface. These relations are given by

$$s^{*}_{xx,\max}(z_0) = A_0 + B_0 s^{r}_{xx}(z_0) + C_0 s^{r}_{yy}(z_0) \quad \textbf{Eq. 4-22}$$

$$s^{*}_{zz,\max}(z_0) = D_0 + E_0 s^{r}_{xx}(z_0) + F_0 s^{r}_{yy}(z_0) \quad \textbf{Eq. 4-23}$$

$$t^{*}_{xz,\max}(z_0) = G_0 + H_0 s^{r}_{xx}(z_0) + L_0 s^{r}_{yy}(z_0) \quad \textbf{Eq. 4-24}$$

$$s^{*}_{yy,\max}(z_0) = u(s^{*}_{xx,\max}(z_0) + s^{*}_{zz,\max}(z_0)) \quad \textbf{Eq. 4-25}$$

These sets of equations can be written in matrix form as follows

$$\begin{bmatrix} s^{*}_{xx,\max}(z_0) \\ s^{*}_{zz,\max}(z_0) \\ t^{*}_{xz,\max}(z_0) \end{bmatrix} = \begin{bmatrix} A_0 \\ D_0 \\ G_0 \end{bmatrix} + \begin{bmatrix} B_0 & C_0 \\ E_0 & F_0 \\ H_0 & L_0 \end{bmatrix} \begin{bmatrix} s^{r}_{xx}(z_0) \\ s^{r}_{yy}(z_0) \end{bmatrix} \quad \textbf{Eq. 4-26}$$

$$\left[s^{*}_{yy,\max}(z_0) \right] = [n][1\ 1] \begin{bmatrix} s^{*}_{xx,\max}(z_0) \\ s^{*}_{zz,\max}(z_0) \end{bmatrix} \qquad \textbf{Eq. 4-27}$$

Good correlations were obtained with R-squared of greater than 94. The statistical results for $s^{*}_{xx,\max}, s^{*}_{zz,\max}, t^{*}_{xz,\max}$ are plotted in the figure 4-15 to 4-17. The normal probability plot in each figure shows a straight line, and the residual versus fitted values plot shows a great level of randomness. Both of the observations are good indications of a good correlation between the maximum elastic stress value and residual stresses.

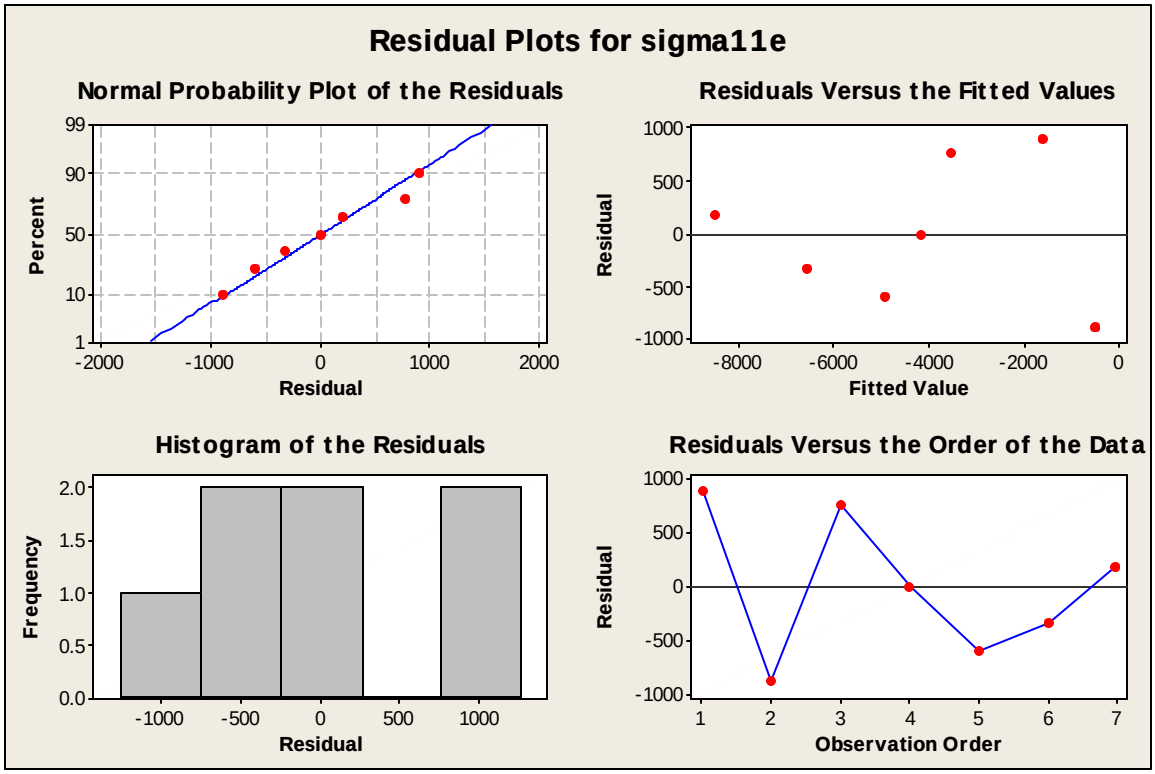

Figure 4-15 Residual plots for $s^{*}_{xx,\max}$ as a functions of $s^{r}_{xx}(z_0)$ and $s^{r}_{yy}(z_0)$

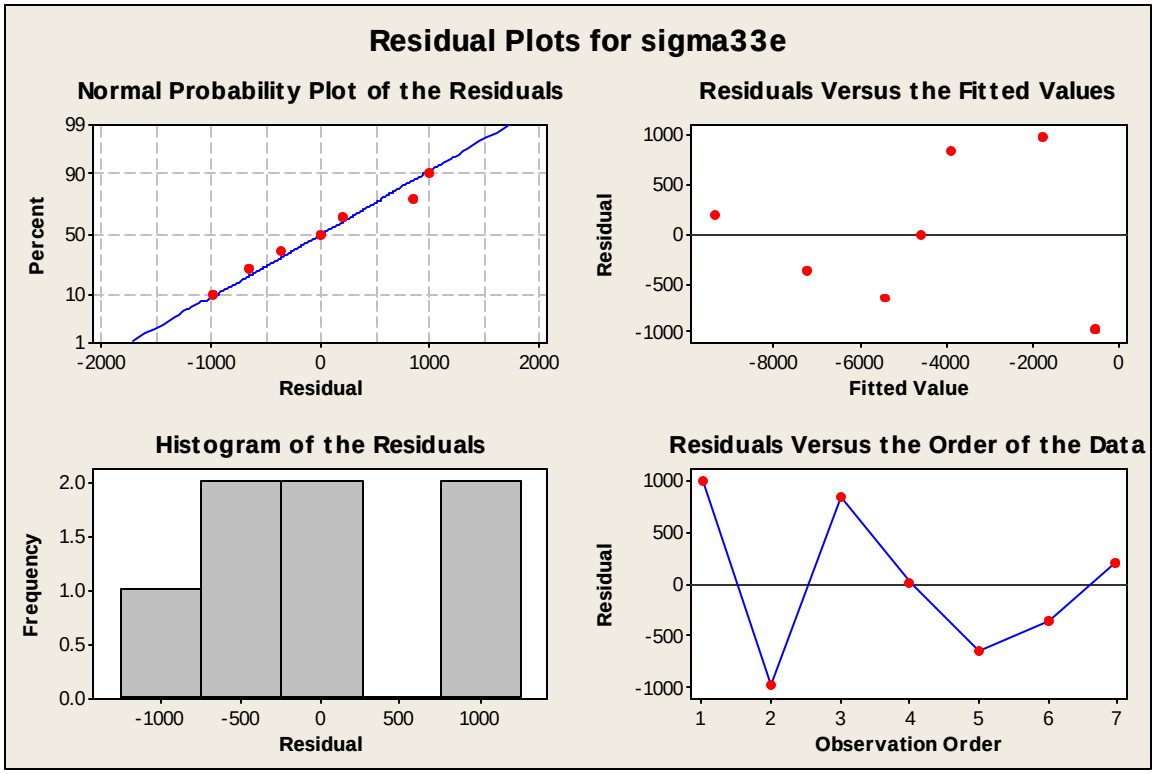

Figure 4-16 Residual plots for $s^{*}_{zz,\max}$ as a functions of $s^{r}_{xx}(z_0)$ and $s^{r}_{yy}(z_0)$

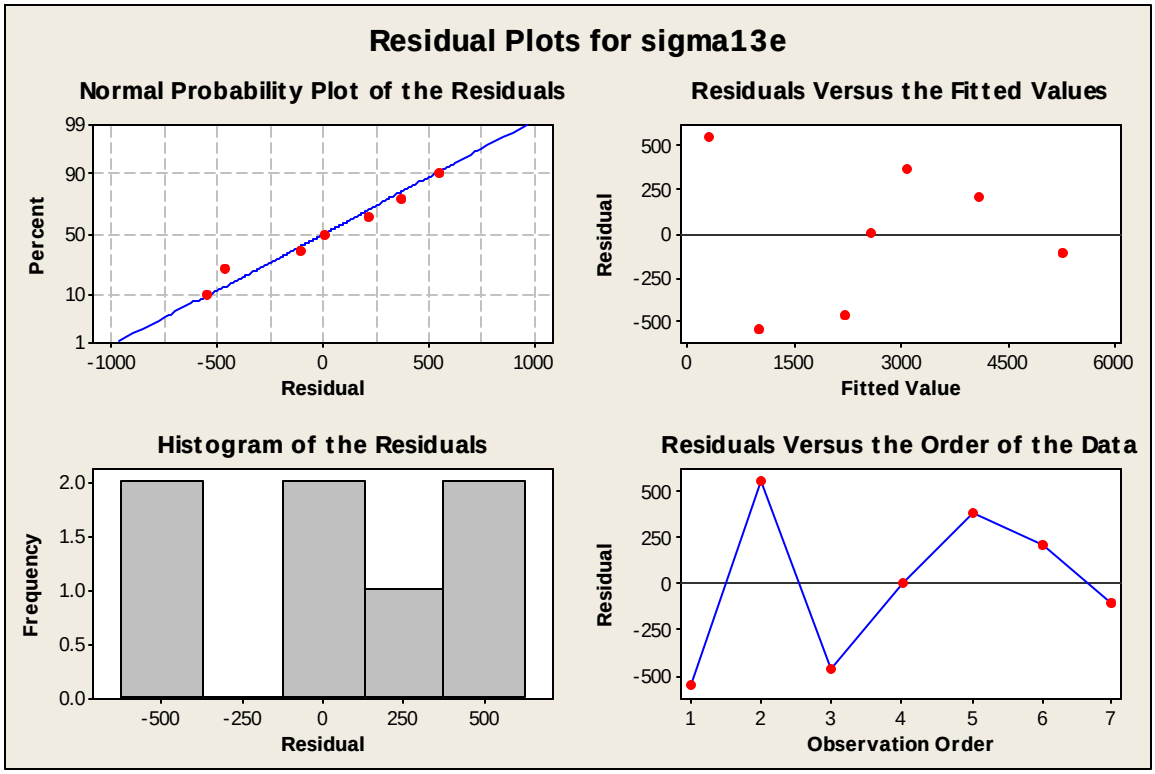

Figure 4-17 Residual plots for $t^{*}_{xz,\max}$ as a functions of $s^{r}_{xx}(z_0)$ and $s^{r}_{yy}(z_0)$

4.3 Estimating the depth of cut form specific cutting energy

Figure 4-18 shows up to now what has been determined. The stress components in the workpiece can be determined from residual stresses. However, a method has to be found in order to determine the depth of cut that would have been necessary to obtain these stresses.

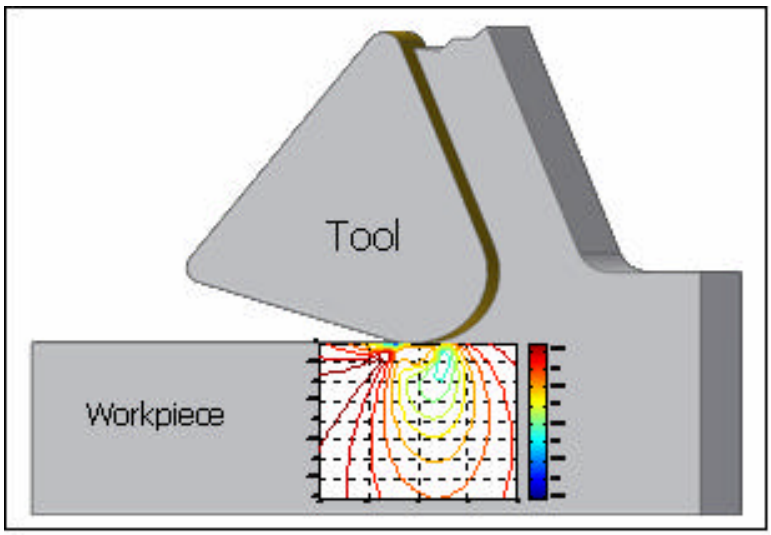

Figure 4-18 Illustration of the equivalent stress seen by the workpiece during cutting

4.3.1 Inverse Method based on specific cutting energy: Depth of cut estimation

Having determined the maximum elastic stress components, the depth cut can be estimated based on the dependency of specific cutting energy on the chip load. Figure 4-19 shows the empirical relationship between the specific cutting energy p_s and the undeformed chip thickness $a_{c_{avg}}$ for various work materials. In the case of orthogonal cutting, the depth of cut and the un-deformed chip thickness are the same parameter.

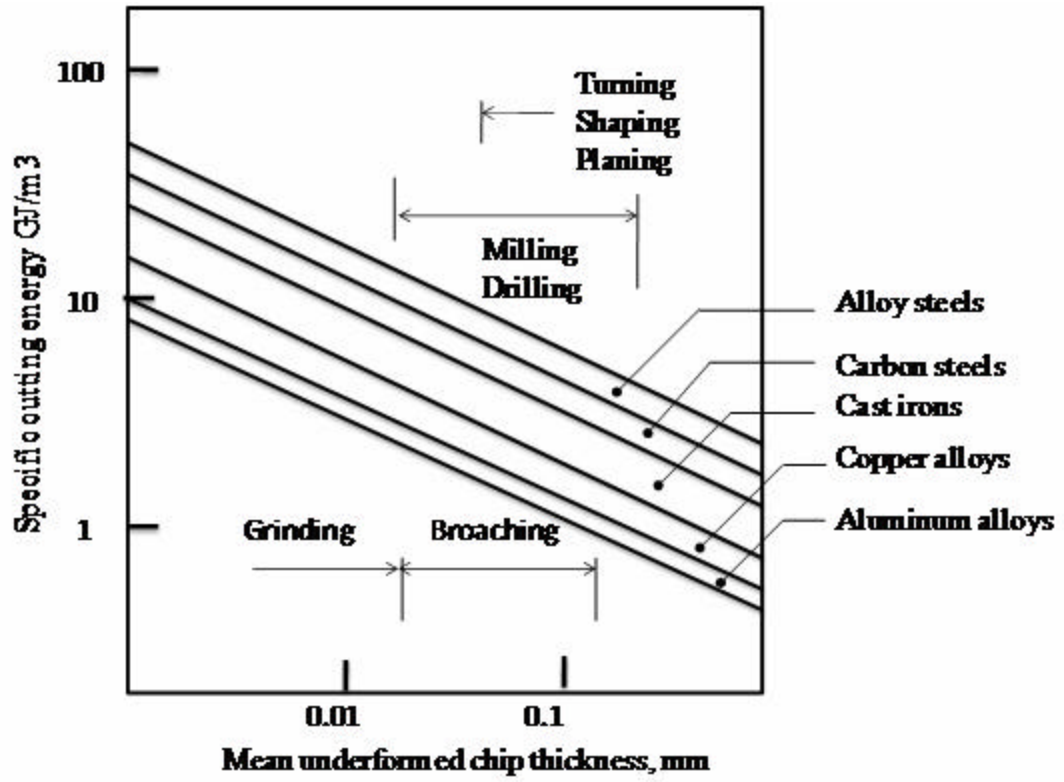

Figure 4-19 Approximate value of the specific cutting energy ps for various materials and operations[87]

The specific cutting energy is defined as the energy consumed in removing a unit volume of material. It can also be thought of as the energy required for the amount of plastic deformation needed for cutting to take place. It is expressed in GJ/m3 in SI unit. The Von Mises criterion is used to calculate the specific cutting energy as shown in equation 4-28. Using the stress components previously determined, the specific cutting energy p_s is determined using the following equation

$$p_s = \sqrt{\frac{\left(s^*_{xx,\max}(z_0) - s^*_{yy,\max}(z_0)\right)^2}{2} + \frac{\left(s^*_{xx,\max}(z_0) - s^*_{zz,\max}(z_0)\right)^2}{2} + \frac{\left(s^*_{yy,\max}(z_0) - s^*_{zz,\max}(z_0)\right)^2}{2} + \frac{6\left(t^*_{xz,\max}(z_0)\right)^2}{2}} \qquad \textbf{Eq. 4-28}$$

Each group of materials occupies a region bounded by two lines. To find the depth of cut from the specific cutting energy, the following procedure was adopted: Taking alloy steels as an example, two depth of cut given by the equation of the two lines on the boundary were calculated.

The equation of the top line is:

$$d_1 = 10^{\frac{0.3-\log(p_s)}{0.46}} \quad \textbf{Eq. 4-29}$$

The equation of the second line is:

$$d_2 = 10^{\frac{0.19-\log(p_s)}{0.46}} \quad \textbf{Eq. 4-30}$$

The average depth of cut was estimated by taking the average of d_1 and d_2 as represented in the following equation:

$$d_{c_{avg}} = \frac{d_1 + d_2}{2} \quad \textbf{Eq. 4-31}$$

4.4 Inverse method based on force equilibrium

For orthogonal cutting, the shear angle is a critical parameter that helps estimating parameters such as cutting forces. It will also help to estimate the hone radius sought after. In the following section, a method to estimate shear angle from the elastic stresses obtained from residual stresses is presented.

4.4.1 Estimation of the stress components for the cutting zone.

The maximum value of the stress components, maximum equivalent stress at a point on the surface of the workpiece, and the depth of cut can be found up to this point

using residual stresses information. For an orthogonal cutting process, the cutting zone called the shear zone can be described by the orientation of the shear plane and the traction on that plane.

As mentioned in chapter 3, the stresses generated in the workpiece are due to the tractions in the shear zone and the tractions due to the rubbing of the tool edge on the surface of the workpiece. At both the shear zone and the tool edge location, there is a normal distributed load coupled with a tangential distributed load. The normal load at the tool edge follows a Hertzian or semi elliptical distribution. However, Su showed in his work that there is no significant loss of accuracy by assuming an uniform distribution versus a semi-elliptical distribution[24]. Figure 4.20 shows these two sources.

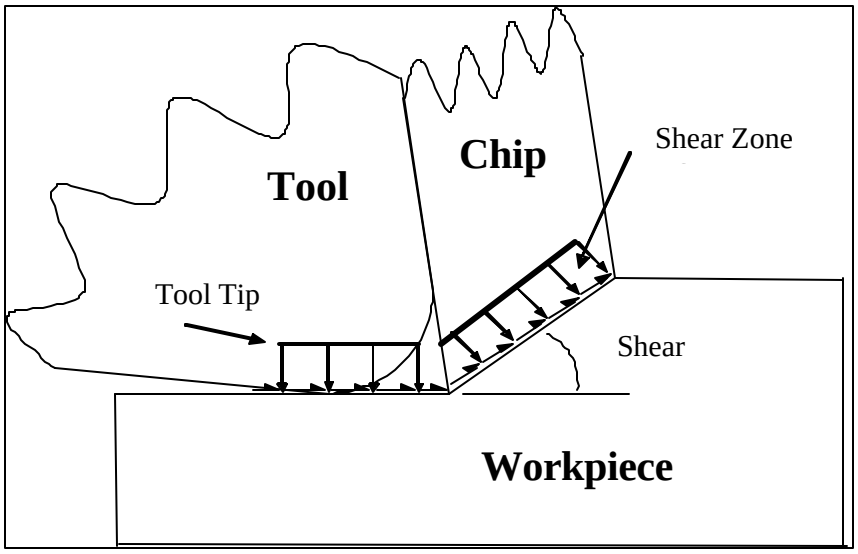

Figure 4-20. Stresses at the shear zone & Stresses due to the tool tip.

Since the stresses in the workpiece are due to two sources, the percentage contribution of each source must be identified first before developing a method to determine the shear zone characteristics. Any point at the newly generated surface of the workpiece will start experiencing stresses due to the tractions on the shear plane, then stresses due to the tractions due to the rubbing of the tool. Figure 4-21 shows a simplified

representation of the stresses to help with the understanding of the previous statement. It should be noted that this figure is not an accurate representation of the loading on the newly generated surface since the shear tractions are omitted. Nonetheless, it helps visualize the challenge in determining the contribution of the two sources to the stress at any point of the workpiece.

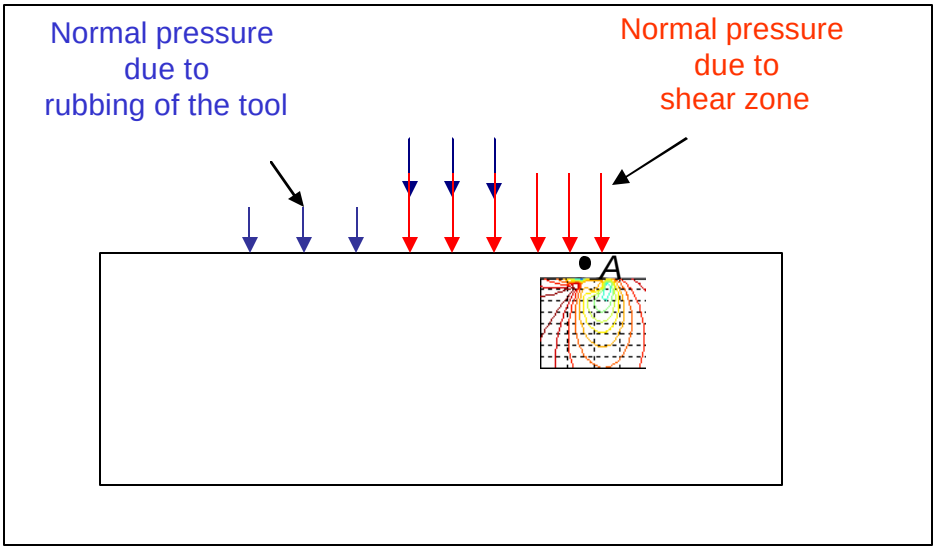

Figure 4-21 Simplified representation of the normal traction on the surface as the tool is sliding.

The following optimization scheme was employed to determine the contribution of both sources. The stress component profiles $s^*_{xx}(z_i), s^*_{zz}(z_i), t^*_{xz}(z_i)$ used in section 4.2 to determine the relations between the residual stress and the Hertzian stresses, are set to be equal to the sum of stress components from the shear zone and ploughing effect, equation 4-29. With the constraints given between the parameters, an optimal combination that gives a satisfactory residual stress profile was determined through iteration.

$$
\begin{aligned}
a s_{xx}^{*,sharp}(z_i) + b s_{xx}^{*,plow}(z_i) &= s_{xx}^{*}(z_i) \\
c s_{zz}^{*,sharp}(z_i) + d s_{zz}^{*,plow}(z_i) &= s_{zz}^{*}(z_i) \\
e t_{xz}^{*,sharp}(z_i) + f t_{xz}^{*,plow}(z_i) &= t_{xz}^{*}(z_i)
\end{aligned}
\qquad \textbf{Eq. 4-32}
$$

with $0 < a, b, d, e, f < 1$ and $b = 1 - a; d = 1 - c; f = 1 - e$

The values of a, b, c, d were found to be equal to 0.5 and the values of e and f were found to be respectively equal to 0.35 and 0.65.

4.4.2 Estimation of the cutting or shear zone characteristics

The characteristics of the shear zone can now be determined by the inverse method developed and depicted in figure 4.22. The model is based on the assumptions that the rake angle, the width of cut and the workpiece are known quantity during the cutting operation. The friction coefficient between the tool and the chip is determined using Merchant relation as expressed in the following two equations:

$$b = 45^{\circ} + a - f \qquad \textbf{Eq. 4-33}$$

$$m = \tan(b) \qquad \textbf{Eq. 4-34}$$

where b is the friction angle, m is the friction coefficient, a is the rake angle, and f is shear angle.

An initial guess of the yielding shear stress of the material is determined using the following uni-axial stress strain relationship:

$$t_{x'z'} = Ee\sqrt{3} \qquad \textbf{Eq. 4-35}$$

where E is elastic modulus, and e is elastic strain.

The elastic strain is assumed to be 0.2% which corresponds to the strain at the onset of yielding for metals.

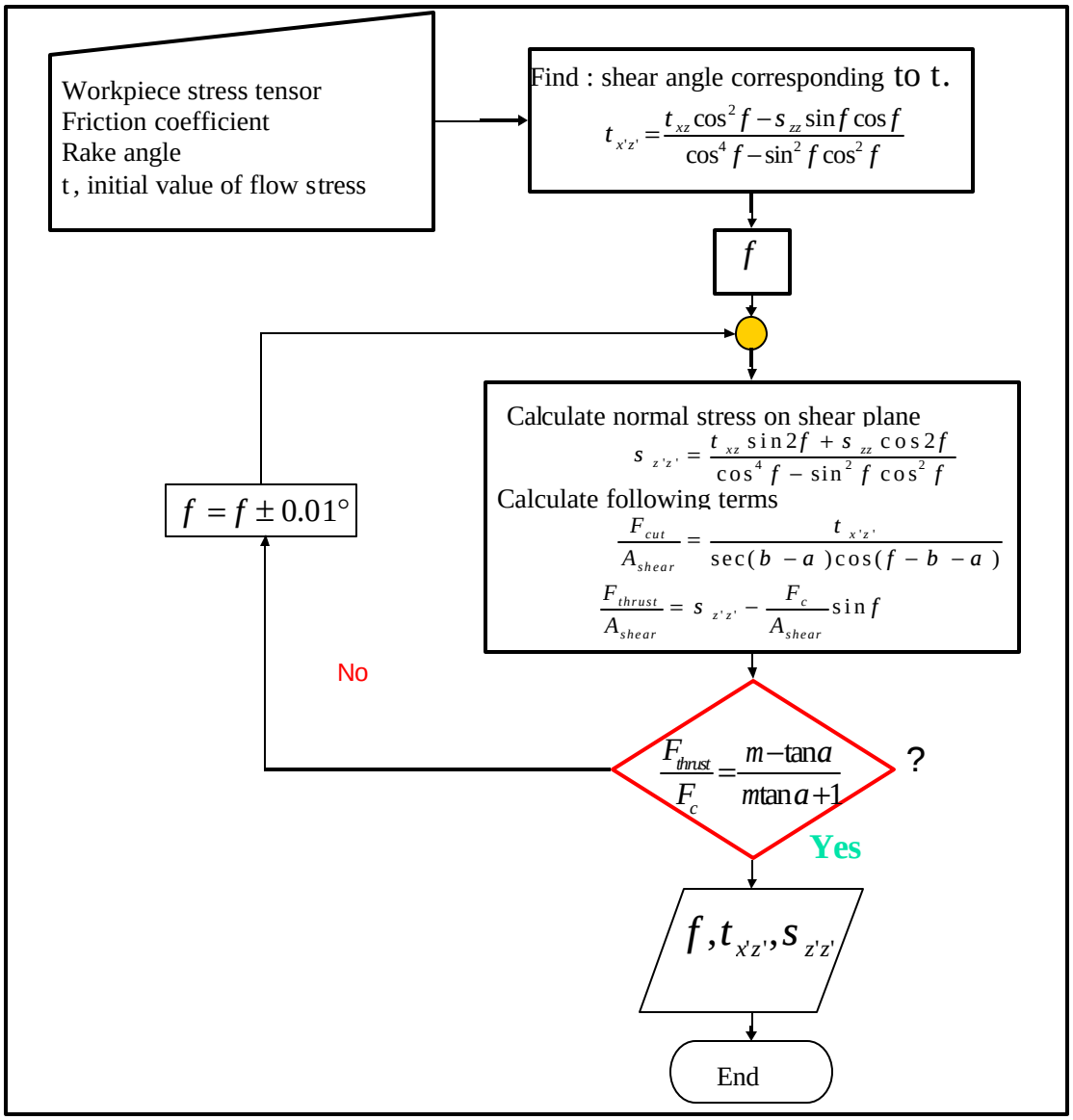

Figure 4-22. Analytical model to determine the shear zone characteristics.

Using a 2D rotation matrix Q presented in equation 4-31, the stress components in the workpiece (x,y) are transformed in to corresponding components in the shear plane (x',y'), as shown in equation 4-32. The rotation of the components is possible because of size of the cutting zone. During most cutting operations, the cutting zone is relatively

small compared to the bulk of workpiece. Thus, compared to size of the workpiece, the size of the cutting zone could be thought of being the size of a point.

$$[Q] = \begin{bmatrix} \cos f & \sin f \\ -\sin f & \cos f \end{bmatrix} \qquad \textbf{Eq. 4-36}$$

$$\begin{bmatrix} s_{x'x'} & t_{x'z'} \\ t_{x'z'} & s_{z'z'} \end{bmatrix} = [Q] \begin{bmatrix} s_{xx} & t_{xz} \\ t_{xz} & s_{zz} \end{bmatrix} [Q]^T \qquad \textbf{Eq. 4-37}$$

Using the stress components in the workpiece previously determined, and the initial guess of the shear stress in the shear zone, the shear angle is found by solving equation 4-38 obtained from 4-37.

$$t_{x'z'} = \frac{t_{xz}\cos^2 f - s_{zz}\sin f \cos f}{\cos^4 f - \sin^2 f \cos^2 f} \qquad \textbf{Eq. 4-38}$$

After obtaining the shear angle f, the friction coefficient, m, can be determined using equations 4-33 and 4-34. Also, the corresponding normal stress $s_{z'z'}$ acting on the shear plane can be found using equation 4-39.

$$s_{z'z'} = \frac{t_{xz}\sin 2f + s_{zz}\cos 2f}{\cos^4 f - \sin^2 f \cos^2 f} \qquad \textbf{Eq. 4-39}$$

The ratio of the cutting and thrust forces to the shear zone area are obtained from the following expressions:

$$\frac{F_{cut}}{A_{shear}} = \frac{t_{x'z'}}{\sec(b-a)\cos(f-b-a)} \qquad \textbf{Eq. 4-40}$$

$$\frac{F_{thrust}}{A_{shear}} = s_{z'z'} - \frac{F_{cut}}{A_{shear}}\sin f \qquad \textbf{Eq. 4-41}$$

where A_{shear} is the size of the shear plane that is given by the following:

$$A_{shear} = \frac{d_{c_{avg}}}{\sin f} w \qquad \textbf{Eq. 4-42}$$

where w is the width of cut

The shear angle, obtained from the initial guess at the value of the shear component acting on the shear plane, needs to be optimized since no effort is made in maintaining a realistic ratio of the cutting and thrust forces. This ratio is giving by the following fundamental expression[88]

$$\frac{F_{thrust}}{F_{cut}} = \frac{m - \tan a}{m \tan a + 1} \qquad \textbf{Eq. 4-43}$$

where m is equal to the coefficient of friction and a the rake angle.

The shear angle is modified until a difference less than 0.5% is achieved between the two sides of equation 4-43. After, the new f is used to re-estimate the stress components in the shear plane $t_{x'z'}, s_{z'z'}$.

4.5 Inverse Method based on Waldorf's slip line: Tool edge radius estimation

In order to instill strength and toughness in the cutting edge, a hone or chamfer is typically part of the tool geometry. As discussed previously, stresses are also generated in the workpiece due to contact between the tool and the newly generated surface. If the tool were perfectly sharp (edge radius = 0), this contact would not exist. A great deal of research has been done regarding the contribution of the hone radius to the overall force required during machining [61-66]. As mentioned in section 3.1.2, the model developed

by Waldorf [56, 66] replicates closely the effect of the edge radius on the cutting process. The geometrical representation of the cutting zone is shown again in this section :

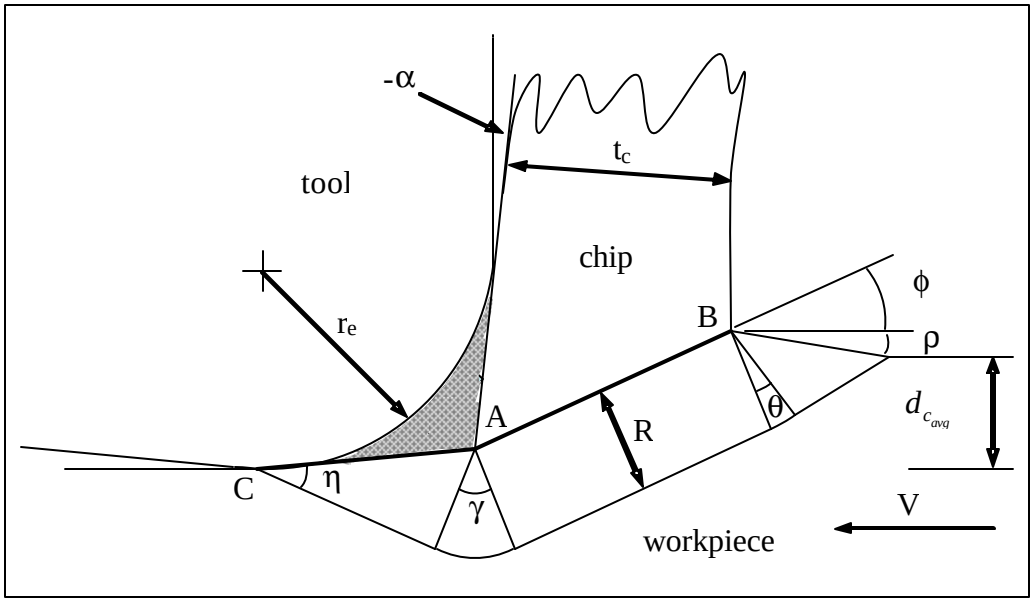

Figure 4-23. Waldorf's slipline field for ploughing[56]

r_e is the edge radius, a is the rake angle, f is the shear angle, r is the prow angle, R is the radius of the circular fan field centered at A, , $d_{c_{avq}}$ is the depth of cut. The fan field angles q , g ? and h are found from geometric and friction relationships as explained in section 3.1.2.

An inverse approach to this model is developed to recapture the radius of the tool based on the depth of cut, shear angle estimated in the previous sections. Using the depth of cut determined previously, the shear zone length AB is determined by:

$$AB = \frac{d_{c_{avg}}}{\cos(f-a)}\left[\frac{\tan(f)\sin(a)+\cos(a)}{\tan(f)}\right] \qquad \textbf{Eq. 4-44}$$

The contact length is then estimated using the following equation:

$$CA = AB\sin(q) \qquad \textbf{Eq. 4-45}$$

The radius of the circular fan field is determined using equation 4-46

$$R = CA\sin(h) \qquad \textbf{Eq. 4-46}$$

The estimation of the hone radius is done by equation 4-47

$$r_e = \frac{R}{x_1 x_2 x_3} \qquad \textbf{Eq. 4-47}$$

where x_1, x_2, x_3 are calculated using equations 4-48 to 4-50

$$x_1 = \frac{\sin(h)}{4\sin^2(h)\sin^2(r)\tan^2(a) + 4\sin^2(h)\sin^2(r) - 1} \qquad \textbf{Eq. 4-48}$$

$$x_2 = 2\sqrt{2}\tan(a)\sin(r)\sin(h) - 2\sqrt{1 - 2\sin^2(h)\sin^2(r)} \qquad \textbf{Eq. 4-49}$$

$$x_3 = \tan\left(\frac{p}{4} + \frac{a}{2}\right) \qquad \textbf{Eq. 4-50}$$

4.6 Summary

In this chapter, a novel approach in predicting process parameters from residual stress required at the surface of the workpiece is presented. The methodology is based on first principles approach to machining. The following chapter presents the validation procedure.

****

CHAPTER 5

EXPERIMENTAL VALIDATION OF MODELING RESULTS

The reverse methodology developed through a first principles approach to machining can be used to predict the depth of cut and edge radius necessary to achieve a given or desired residual stress profile. Matlab 7.1 is used to execute the necessary computer code required for a successful run of the model. The computer used was a Dell Inspiron 700m with a Pentium M 1.86 GHz processor and 512MB of memory.

This chapter presents the procedure followed to gauge the validity and capability of the methodology developed. In the section 1.1.1, the depth of cut and hone radius predicted by the reverse model are compared to experimental data obtained from the orthogonal cutting of AISI 4340 and AISI 316L. In section 2, the residual stresses used as input to the model are compared to the residual stresses obtained from using the output of the model. In section 3, the model prediction of forces is compared to data obtained from another set of experiments of orthogonal cutting of AISI 4340.

5.1 Modeling Results for Orthogonal Cutting of AISI 4340

5.1.1 Depth of cut and edge radius prediction for AISI 4340

The depth of cut and tool edge are predicted from the residual stresses obtained experimentally from orthogonal cutting of AISI 4340. The study was conducted by

Jacobus[18]. The cutting parameters and tool material used during the cutting experiments are given in the following table:

Table 5-1 Cutting conditions for Cases 1-6 [18]

Case	Tool	Material	Edge Radius (mm)	Feed (mm/rev)	Width of Cut (mm)	Speed (m/s)
1	K313	AISI 4340	0.025	0.100	3	5.00
2	K313	AISI 4340	0.075	0.100	3	5.00
3	K313	AISI 4340	0.025	0.200	3	5.00
4	K313	AISI 4340	0.075	0.200	3	5.00
5	K313	AISI 4340	0.050	0.150	3	5.00
6	K313	AISI 4340	0.050	0.125	3	5.00

The tool material (K313) utilized was an uncoated tungsten carbide tool. The cutting speed was maintained at 5m/s for all cases. Only the edge radius and feed were varied in this study. Since the orthogonal cut was achieved using an interrupted turning cut, the feed represents the depth of cut. The residual stresses in the workpiece or the depth profiles of residual stress were measured using an X-ray diffraction technique combined with an electro-polishing method. The electro-polishing method made it possible for the stresses beneath the surface to be measured by X-ray diffraction. First order corrections to the residual stress data were made due to the volume of material removed during etching.

Table 5-2 Additional material properties used in the model

Material	E (GPa)	ν	H (GPa)	ρ (kg/m^3)	k (W/m°C)	C_P (J/kg°C)	α (°C^{-1})	T_m (°C)
AISI 4340	200	0.28	70	7800	40.0	500	11.0e-6	1400

Table 5.2 shows the material properties used in the reverse model. Using the measured surface residual stress values at the surface, the depth of cut and edge radius were predicted based on the models presented in sections 4.2.2, 4.3.1, 4.4.2 and 4.5. Figure 5.1 shows a graph comparing the depth of cut predicted to the depth of cut used during the experiments. Figure 5.2 shows a graph comparing the tool edge radius predicted to edge radius using the cutting experiments.

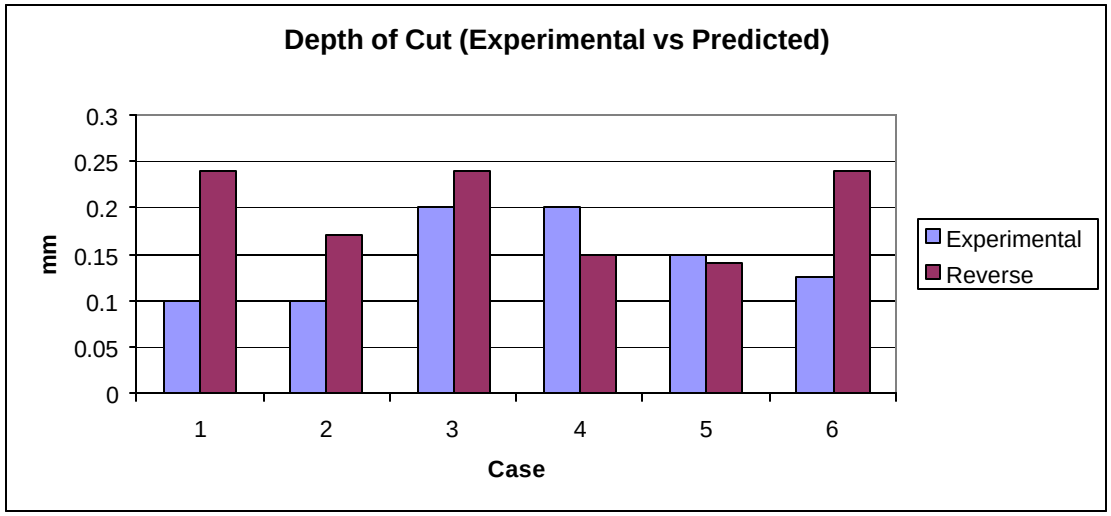

Figure 5-1 Depth of cut comparison for the orthogonal cutting of AISI 4340

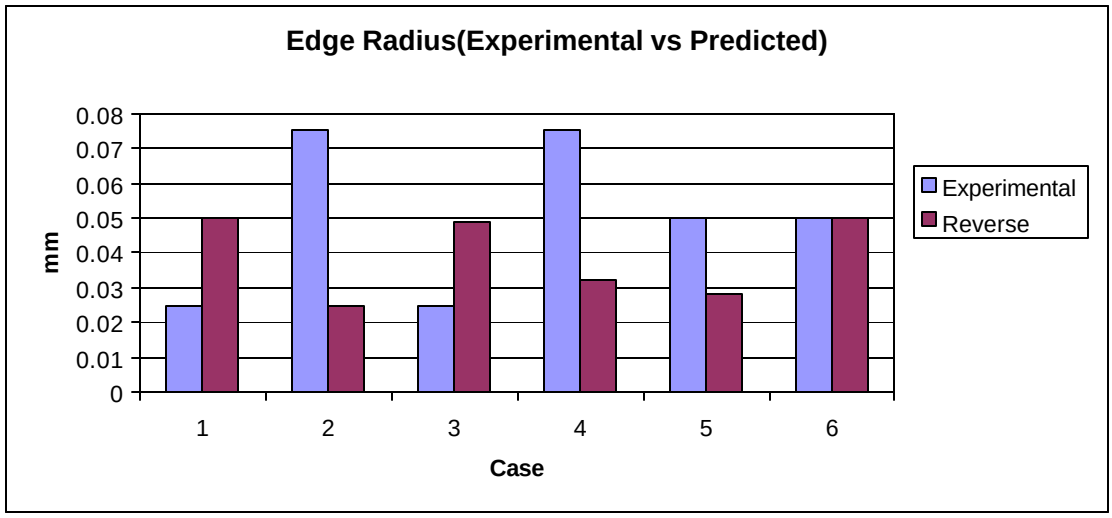

Figure 5-2 Edge radius comparison for the orthogonal cutting of AISI 4340

As seen in both figure 5.1 and 5.2, there is a noticeable difference between the values predicted and the value used for most of the cases. This difference was to be expected and it is due to the non-uniquess nature of plastic deformation. As was presented with great detail in chapter 3, different loading paths can lead to the same residual stress profile. Further, the difference is also due to the simplifying assumptions made in the model. Therefore, to understand how significant or insignificant the difference in prediction is, one extra step in the validation procedure is needed. This step consists in estimating the residual stresses using the predicted depth of cut and edge radius. The forward model developed by Su[24] will be used to predict the residual stress profile under these new set of conditions.

5.1.2 **Forward model performance**

Due to the significant cost associated with measuring residual stresses, an analytical model developed by Su[24] was utilized to estimate the residual stresses from

the predicted depth of cut and hone radius. The performance of this model or "forward" model is investigated using the orthogonal cutting conditions given in table 5-1.

The following figures shows the residual stress profiles obtained from the "forward" model with the corresponding experimental curves for each case. For each of the residual stress profiles, the residual stresses are of negligible magnitude by 0.200mm below the surface. The general trend present in the measured residual stress profiles are also captured by the "forward" model.

In case 1, using a 0.025 mm edge radius, the residual stress is approximately 0MPa beyond 0.100mm. The "forward" model was able to capture this trend. In cases 1 and 2, the model predictions agrees with the experimental data in showing an increase in the region of compressive residual stress beneath the workpiece surface for increased edge radius. In cases 3 and 4, the model captured the increase in the depth of residual stress due to machining for increasing values of the depth of cut. For cases 5 and 6, the model was able to capture the effect of the intermediate value used for the edge radius and the depth of cut. The overall effect of the edge radius and the depth of cut on the residual stress profile was captured. Further, the average difference between the measured and predicted values of the residual stresses in the x-direction and y-direction were respectively 8.5% and 29%. Therefore, the performance of this model made it suitable to generate the residual stress profile necessary to gauge the validity and performance of the model.

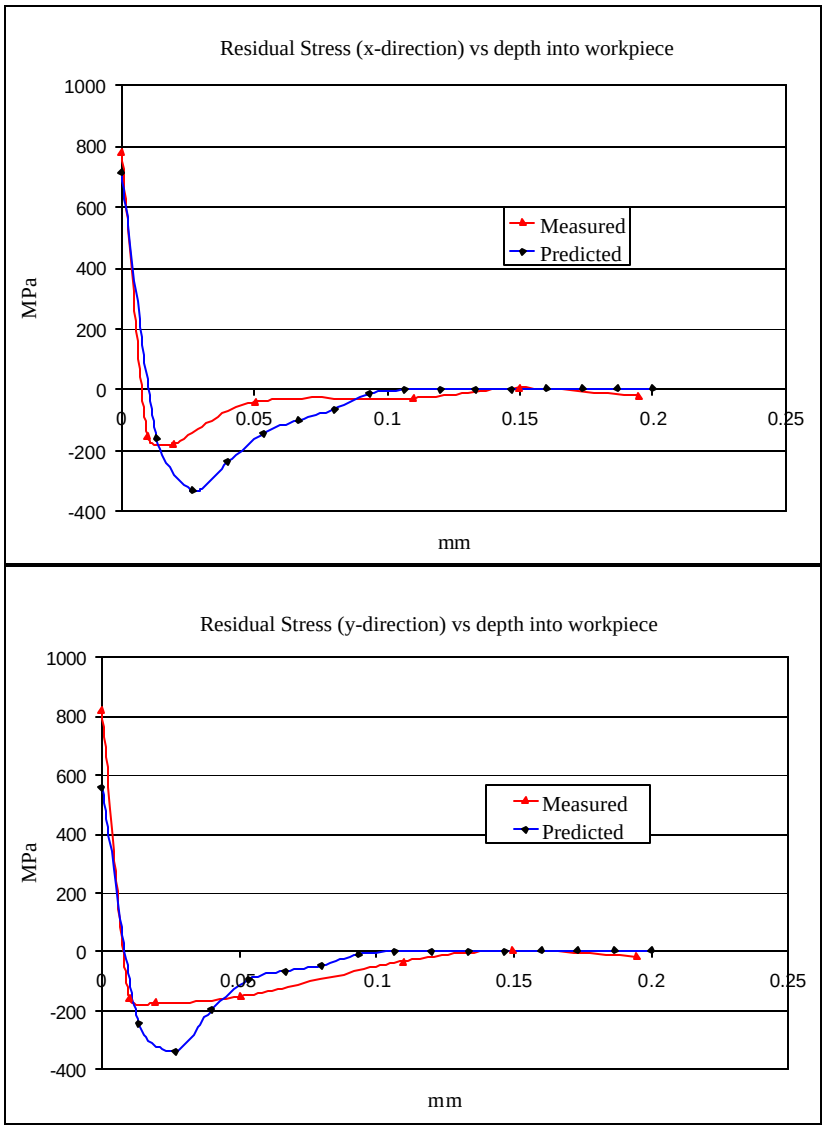

Figure 5-3. Residual stress profiles in the x-direction and y-direction for case 1 [24]

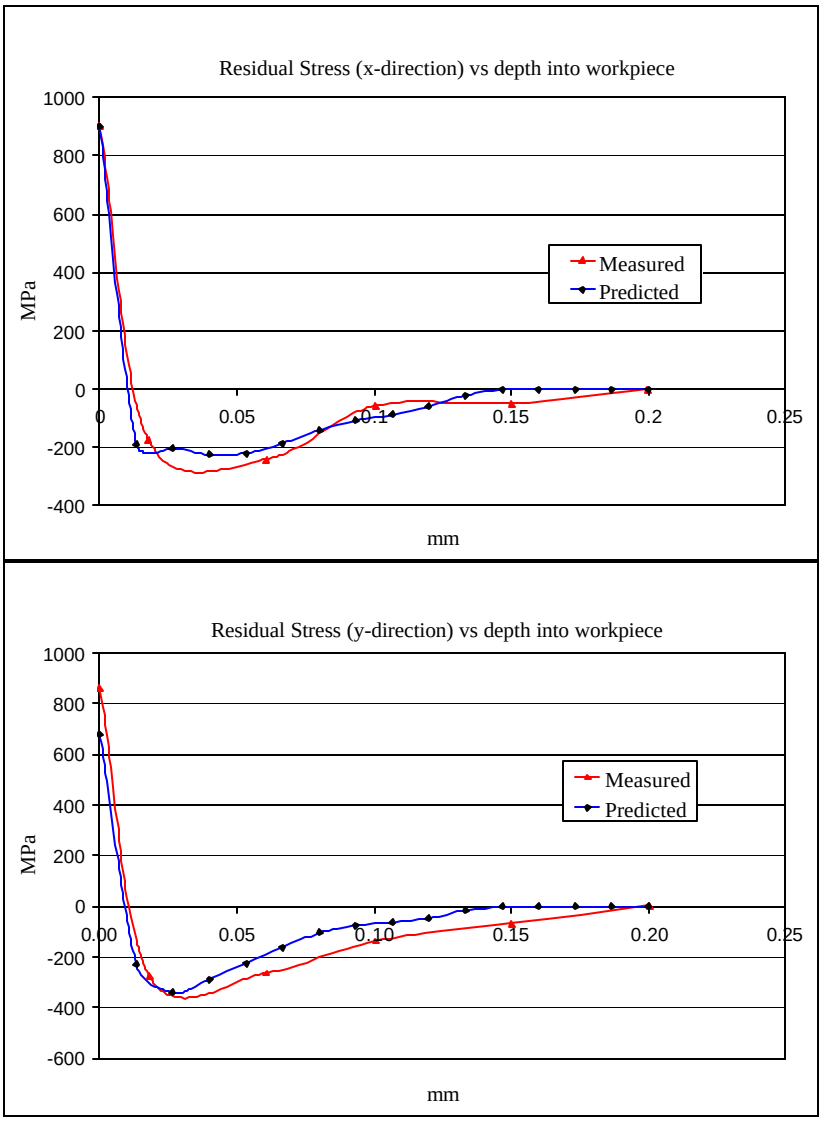

Figure 5-4 Residual stress profiles in the x-direction and y-direction for case 2 [24]

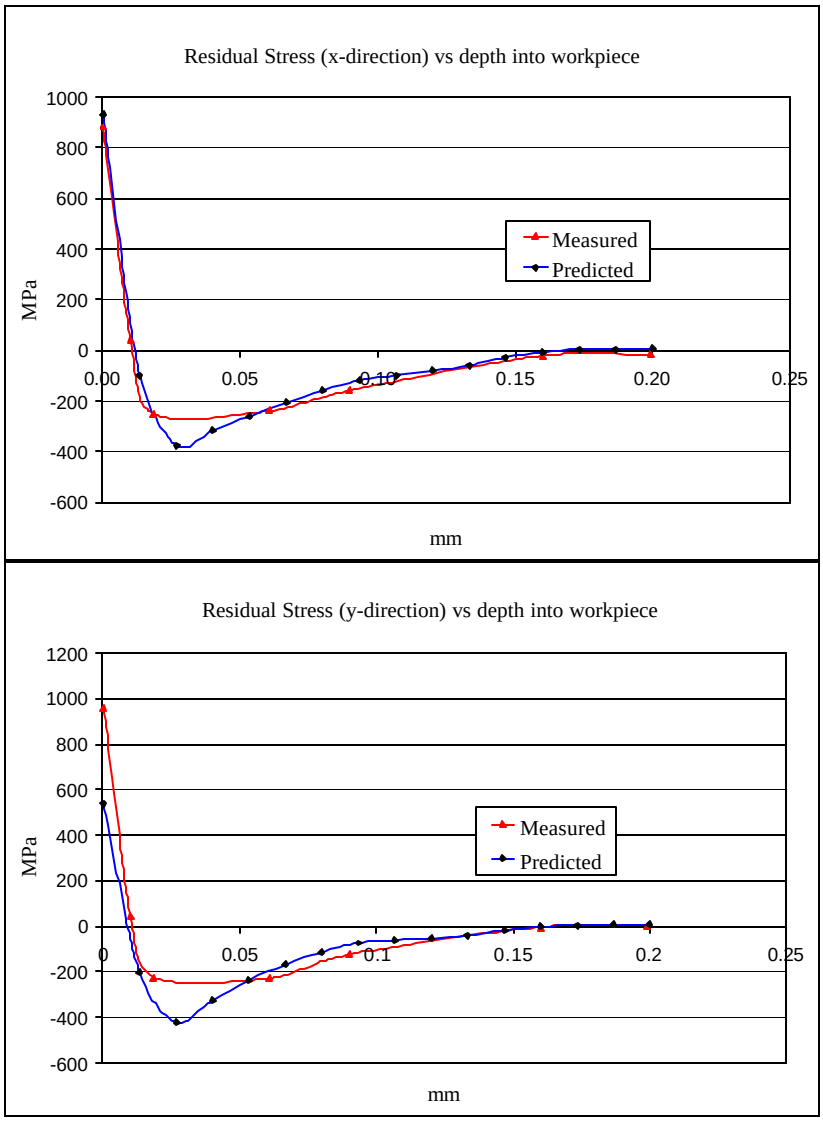

Figure 5-5 Residual stress profiles in the x-direction and y-direction for case 3 [24]

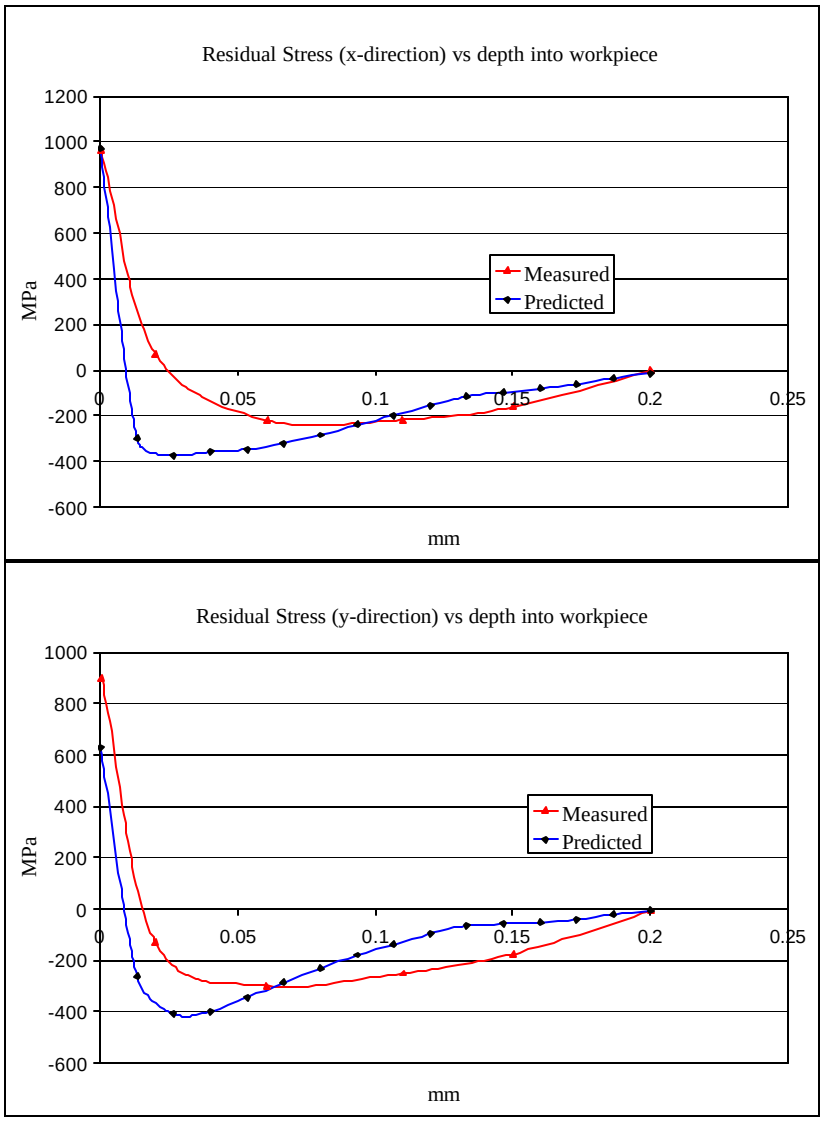

Figure 5-6 Residual stress profiles in the x-direction and y-direction for case 4 [24]

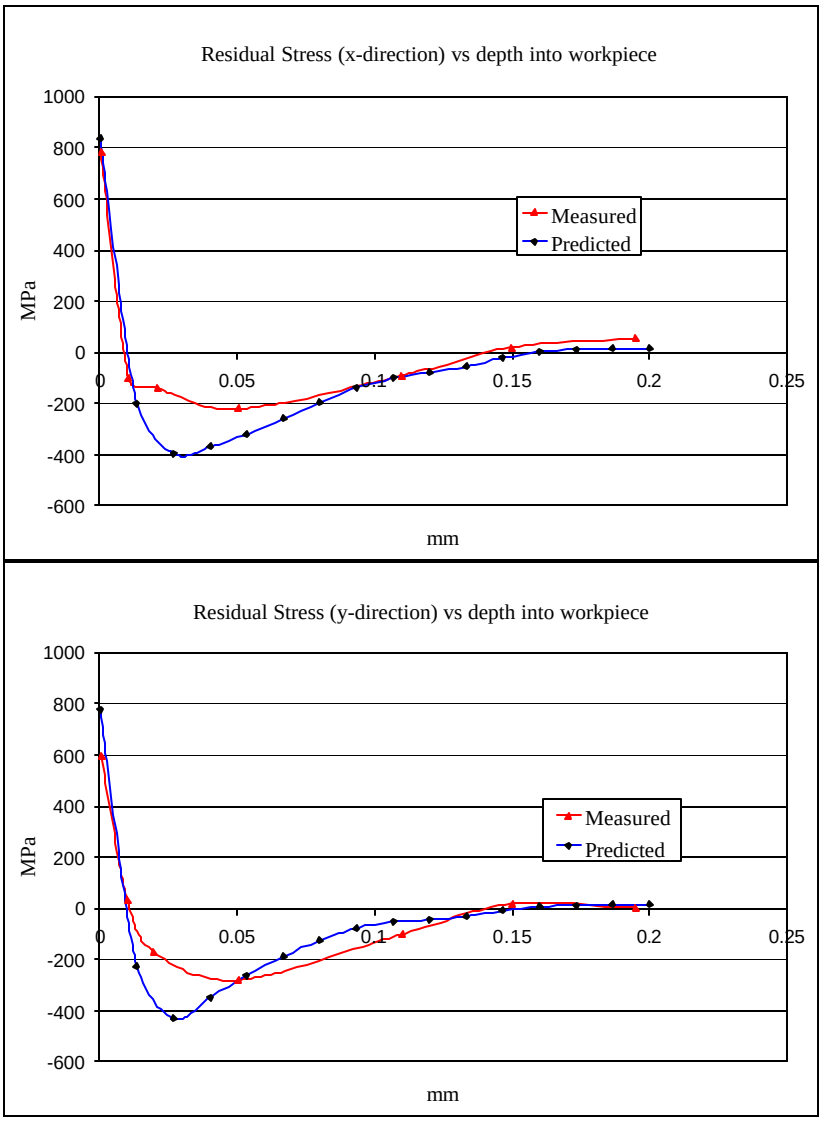

Figure 5-7 Residual stress profiles in the x-direction and y-direction for case 5 [24]

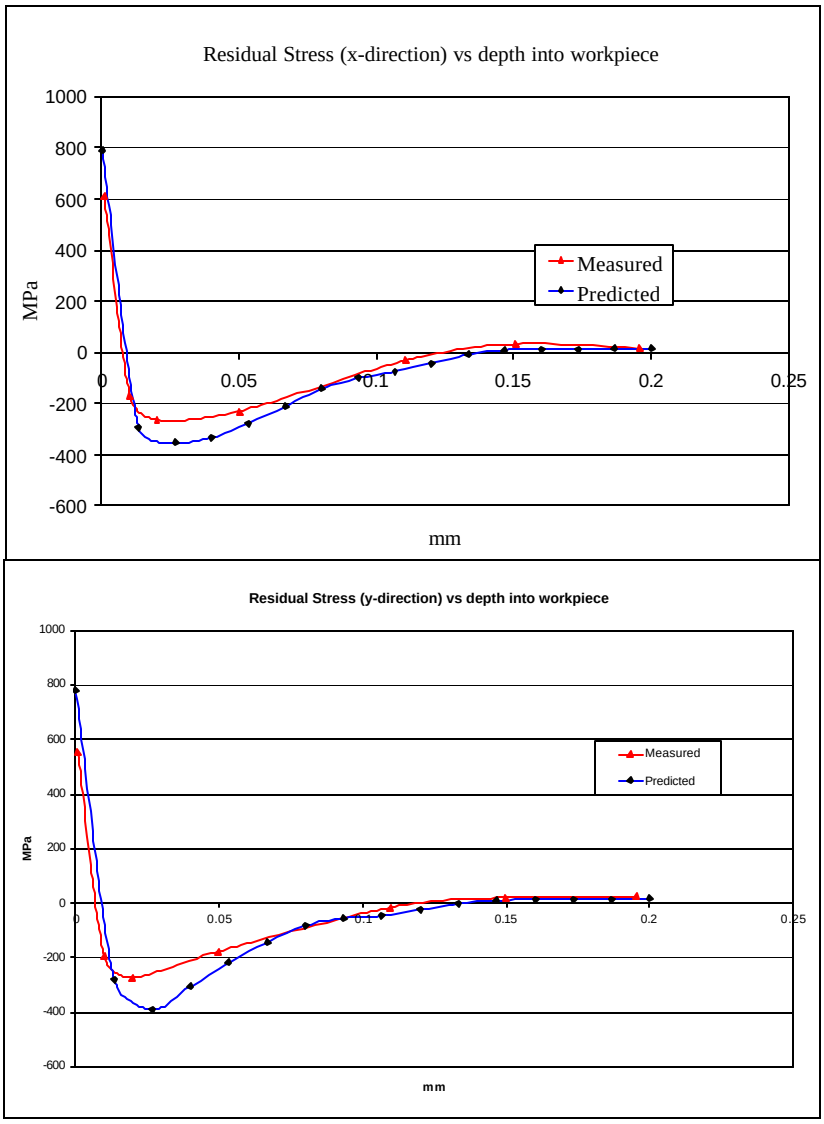

Figure 5-8 Residual stress profiles in the x-direction and y-direction for case 6 [24]

5.1.3 Reverse and forward models comparison

Now that the forward model performance is evaluated, the next step is to gauge the validity of the reverse model at predicting the depth of cut and edge radius from surface residual stresses. The following figure shows the procedure followed:

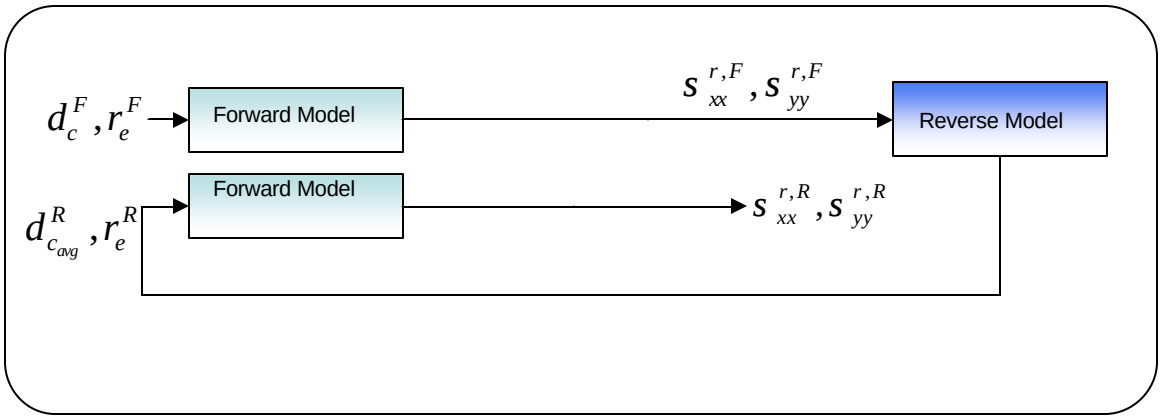

Figure 5-9 Validation scheme flowchart

The depth of cut and edge radius (d_c^F, r_c^F) used for each case are input to a "forward" model to determine the residual stress profiles in the x-direction $s_{xx}^{r,F}(z_i)$ and y-direction $s_{yy}^{r,F}(z_i)$. The surface values of the residual stresses ($s_{xx}^{r,F}(z_0), s_{yy}^{r,F}(z_0)$) are then fed to the reverse model and new depth of cut and hone radius values ($d_{c_{avg}}^R, r_e^R$) are obtained. These new parameters are used to predict a new set of residual stress profiles ($s_{xx}^{r,R}(z_i), s_{yy}^{r,R}(z_i)$). The comparison plots for the depth of cut used in the forward model and the depth of cut obtained by the reverse model are given in figure 5.10. Figure 5.11 shows the comparison plots for the edge radius for each case. Again the difference for the two parameters predicted is noticeable.

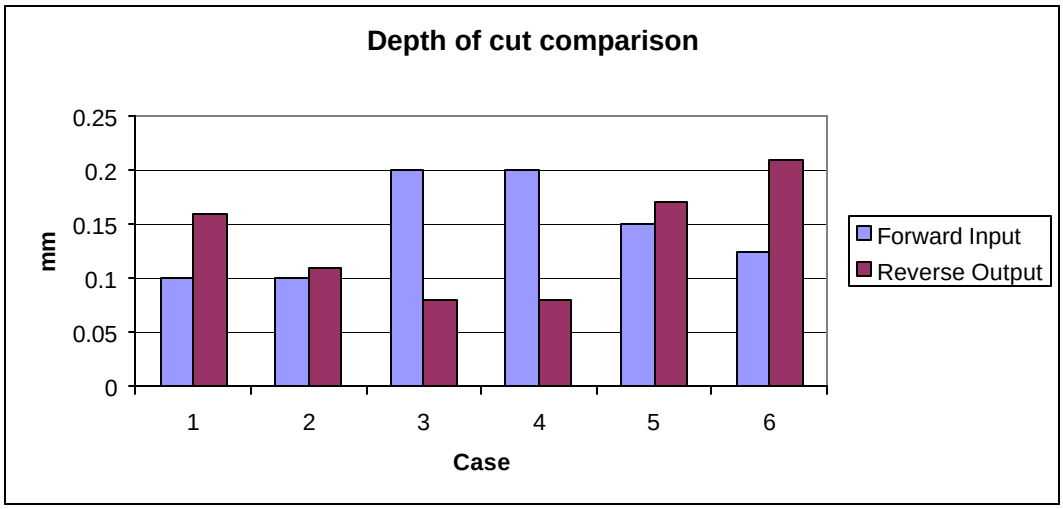

Figure 5-10 Depth of cut comparison between the forward model input and the reverse model output

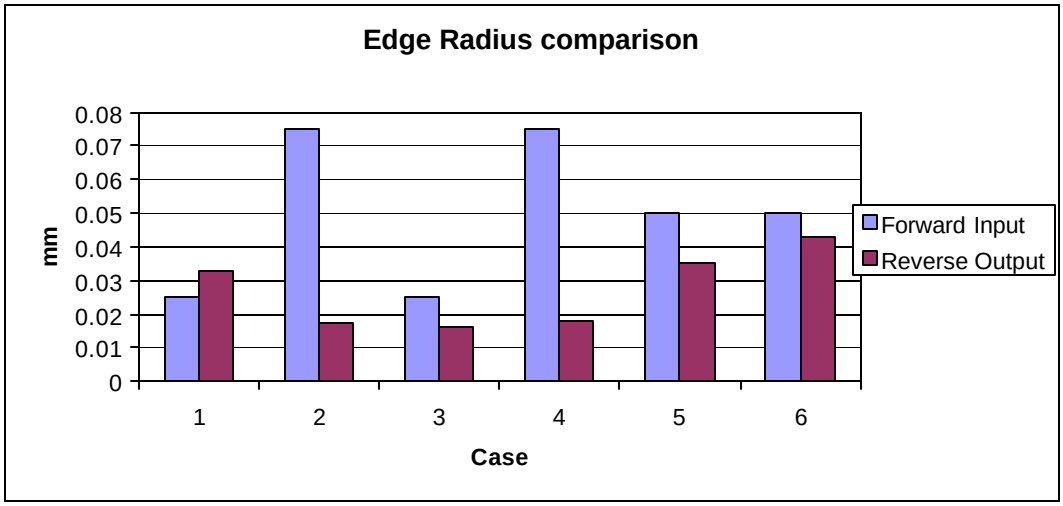

Figure 5-11 Edge radius comparison between the forward model input and the reverse model output

The two parameters predicted, based on the "forward" calculated residual stress, are used as input to the "forward" model and a new set of residual profiles is obtained. Figures 5.12 and 5.13 show the comparison between the value of the residual stresses at the surface in the x-direction $[(s_{xx}^{r,F}(z_0), s_{xx}^{r,R}(z_0)]$ and y-direction $(s_{xx}^{r,F}(z_0), s_{yy}^{r,F}(z_0))$. The average difference in the x-direction and y-direction were respectively about 19% and about 5%.

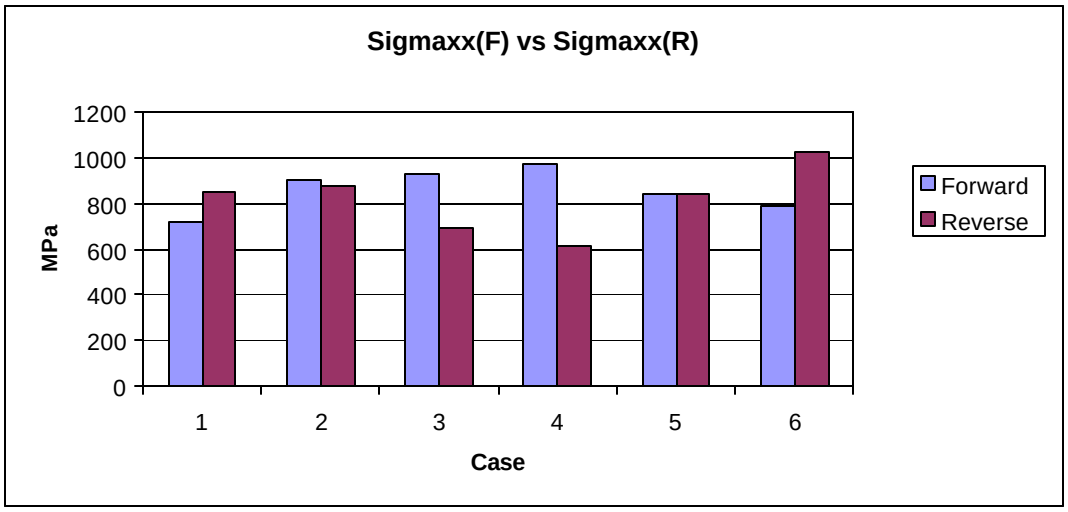

Figure 5-12 Comparison of the residual stress at the surface in the x-direction

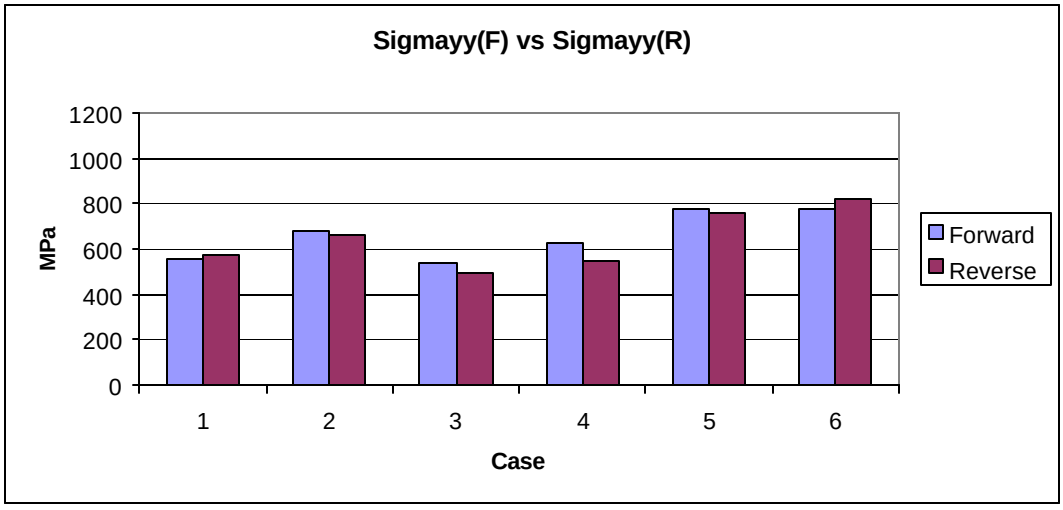

Figure 5-13 Comparison of the residual stress at the surface in the y-direction

The residual stress profiles obtained from using the predicted depth of cut and edge radius, are compared with the input residual stress profiles to the reverse model. The comparison for each case is presented in figures 5.14 to 5.19. The residual stress profiles obtained by the predicted depth of cut and edge radius are close match to the input residual stress profiles. The close match proves that the error associated with simplifying assumptions is not significant.

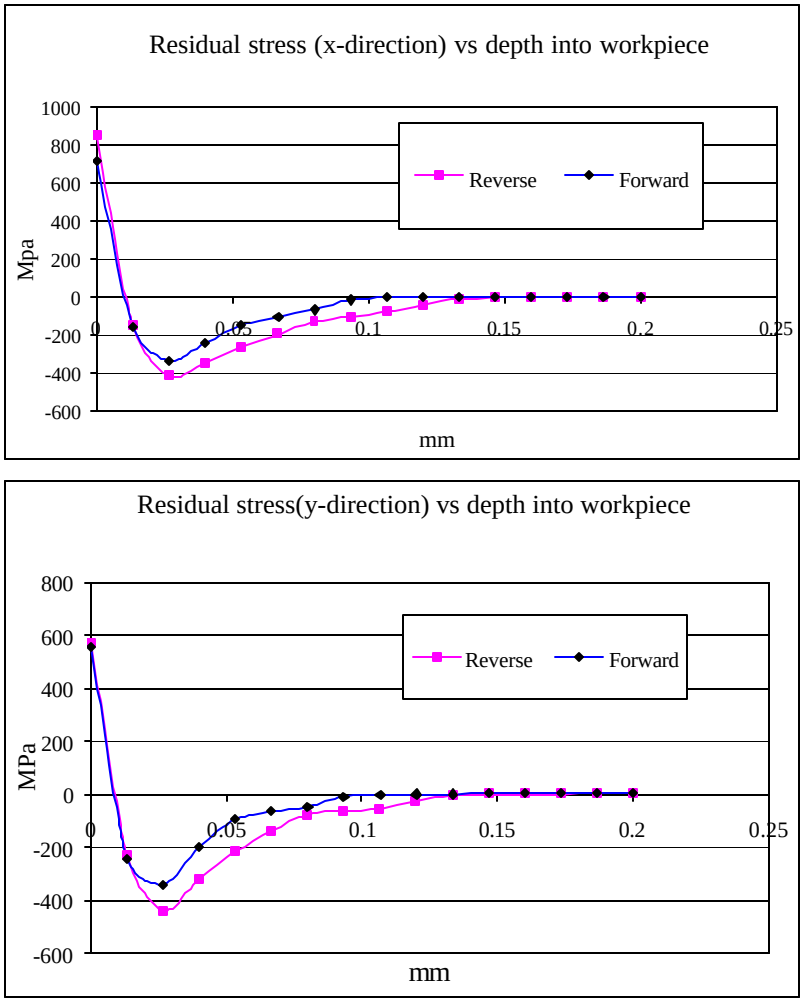

Figure 5-14. Residual stress profile in x and y direction for case 1

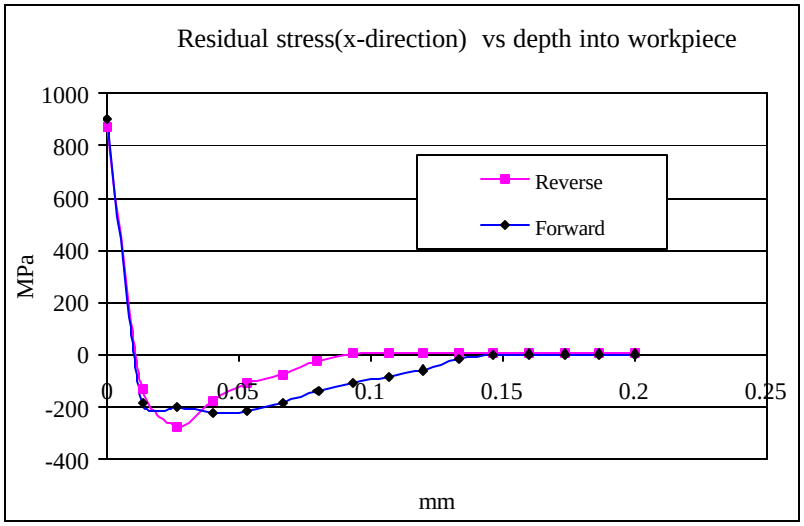

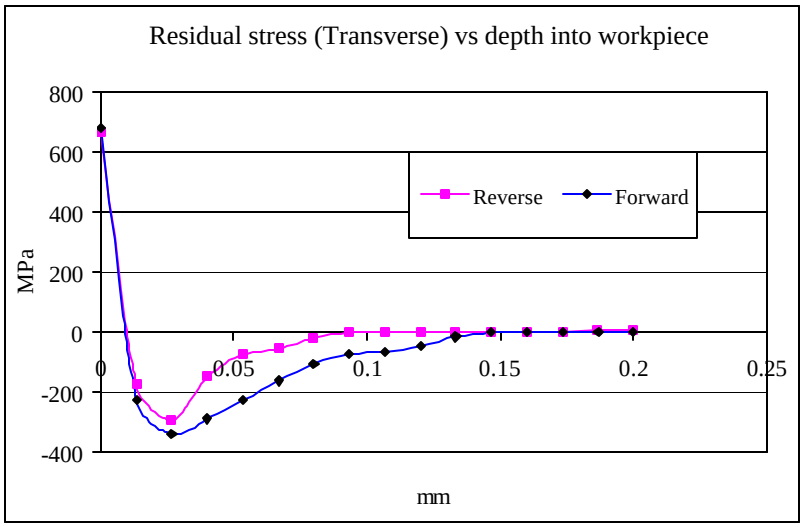

Figure 5-15. Residual stress profile in x and y direction for case 2

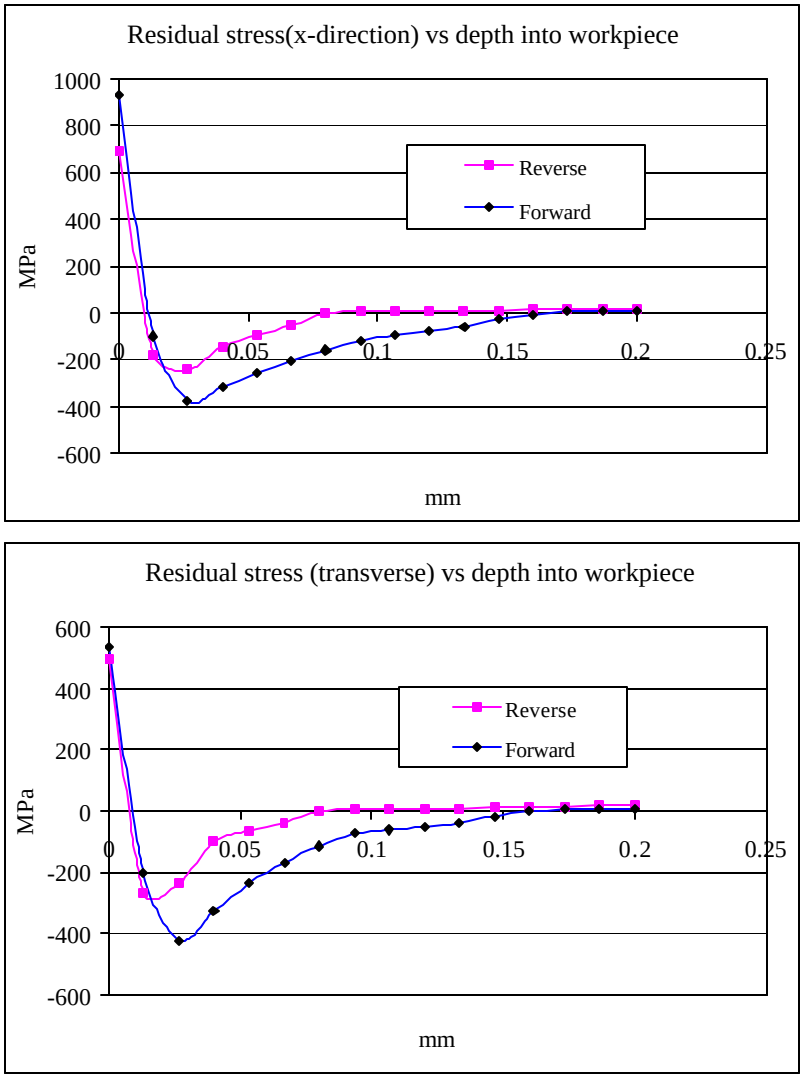

Figure 5-16. Residual stress profile in x and y direction for case 3

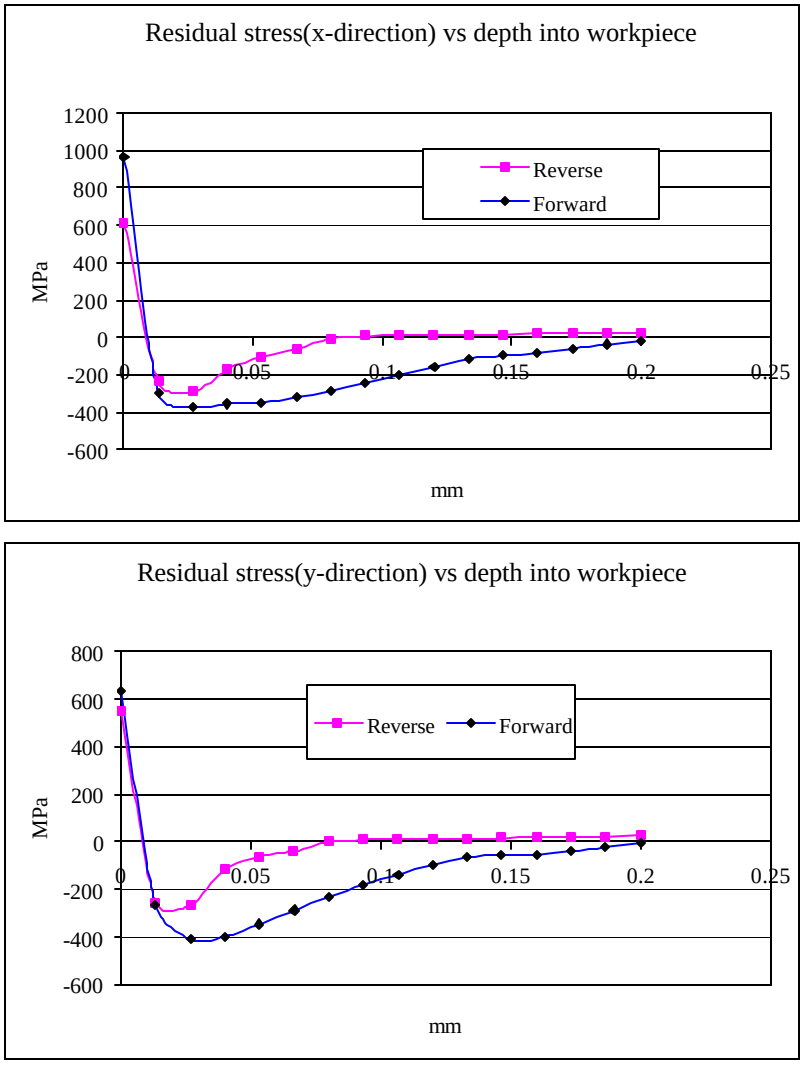

Figure 5-17. Residual stress profile in x and y direction for case 4

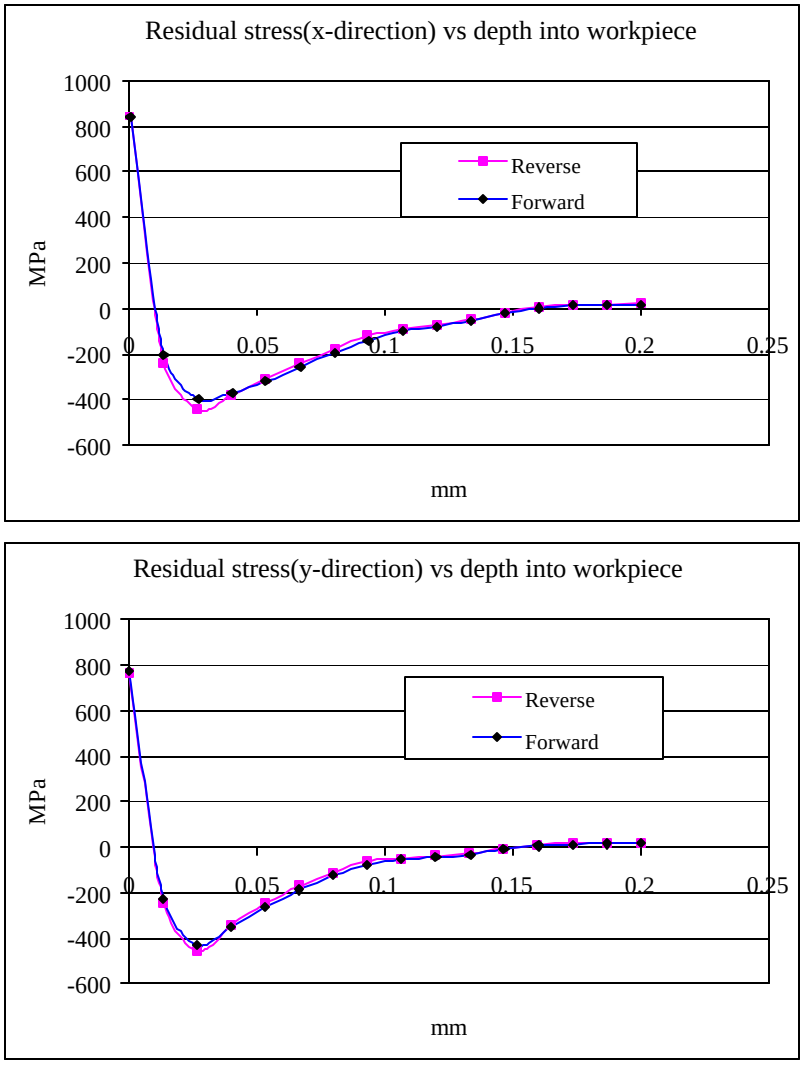

Figure 5-18. Residual stress profile in x and y directi on for case 5

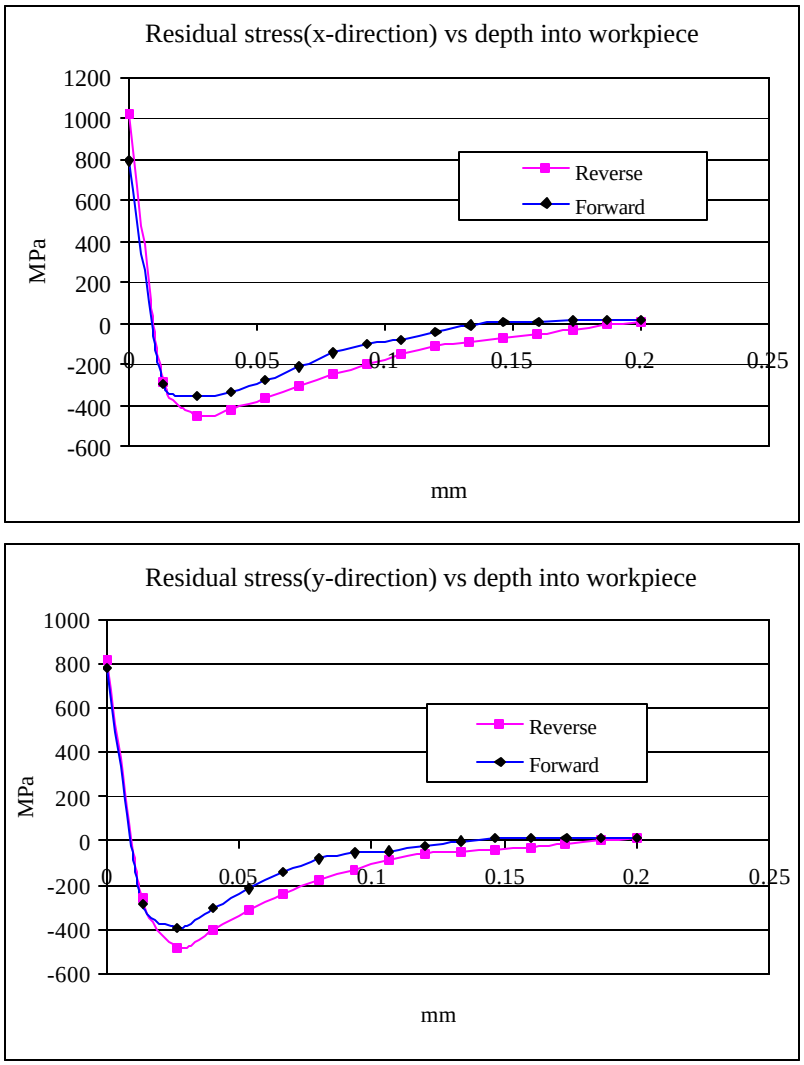

Figure 5-19. Residual stress profile in x and y direction for case 6

5.1.4 Validation using experimental data, reverse and forward models.

After showing that the error associated with the assumptions made to develop the model is not significant, figure 5-20 shows the complete validation flowchart.

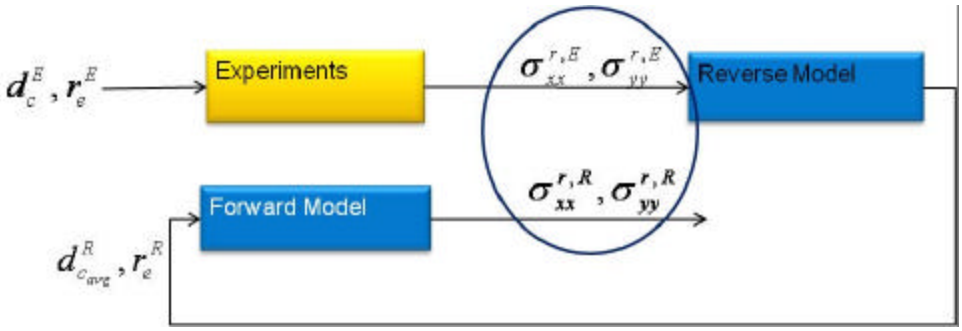

Figure 5-20 Validation Flowchart

The surface residual stresses value in the x and y directions obtained from x-ray diffraction are input to the reverse model. Then, the output of this model namely the depth of cut and edge radius are input the forward model. Finally, the predicted residual stress profiles are compared to the experimentally measured residual stress profiles for each case as shown in figure 5-21 to 5-26. The predicted residual stress profiles follow the trend of the measured profiles.

The residual stress value is positive at the surface, reaches a maximum negative (compressive) value near the sub-surface and then increases to zero value as the depth is increased. As mentioned, the experimental residual stress values at the surface are used as inputs to the reverse model. A closer look shows that the predicted residual stress values are in good agreement with the measured values. The difference in most cases is less than 30%. This error is relatively small when considering the simplifying assumption made in the model. Further, it should be mentioned that experimental measurement of residual stress is prone to large margin of error.

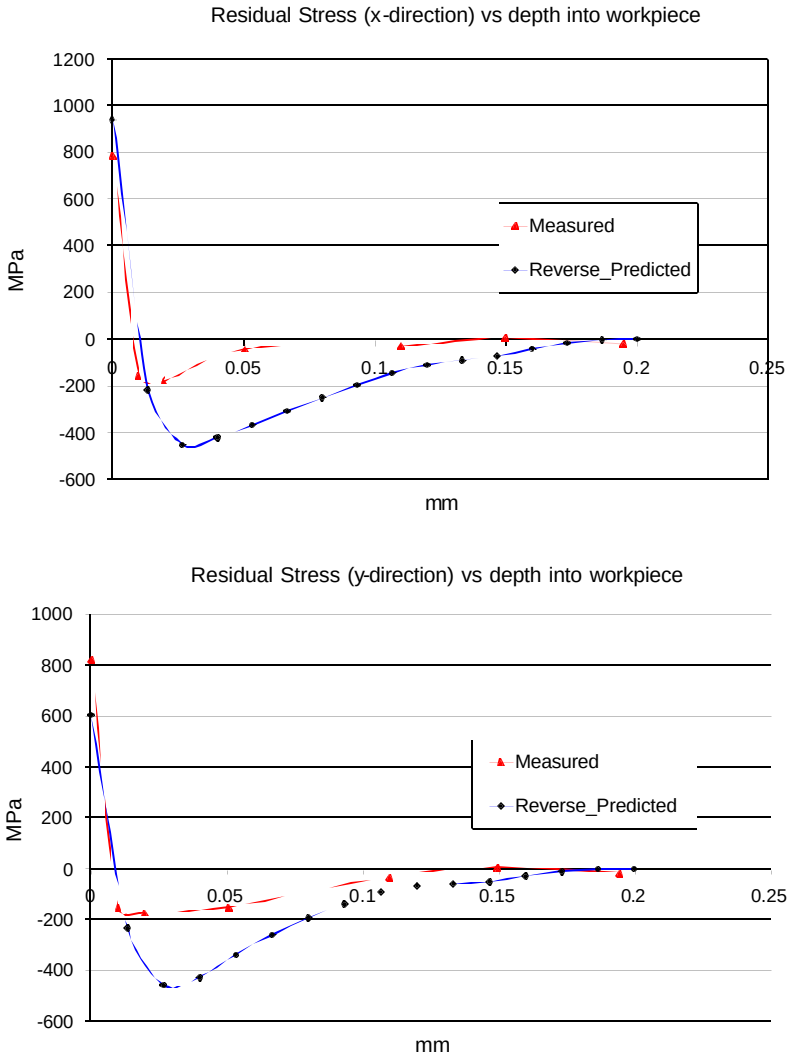

Figure 5-21. Residual stress profile in x and y direction for case 1

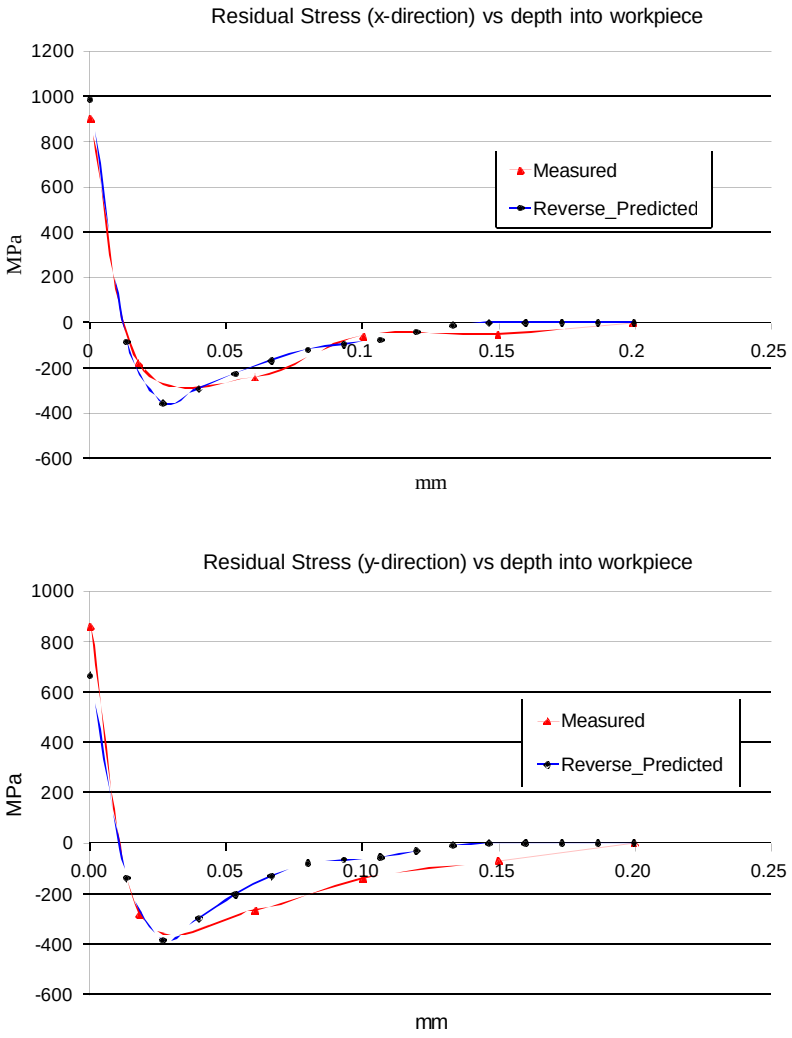

Figure 5-22. Residual stress profile in x and y direction for case 2

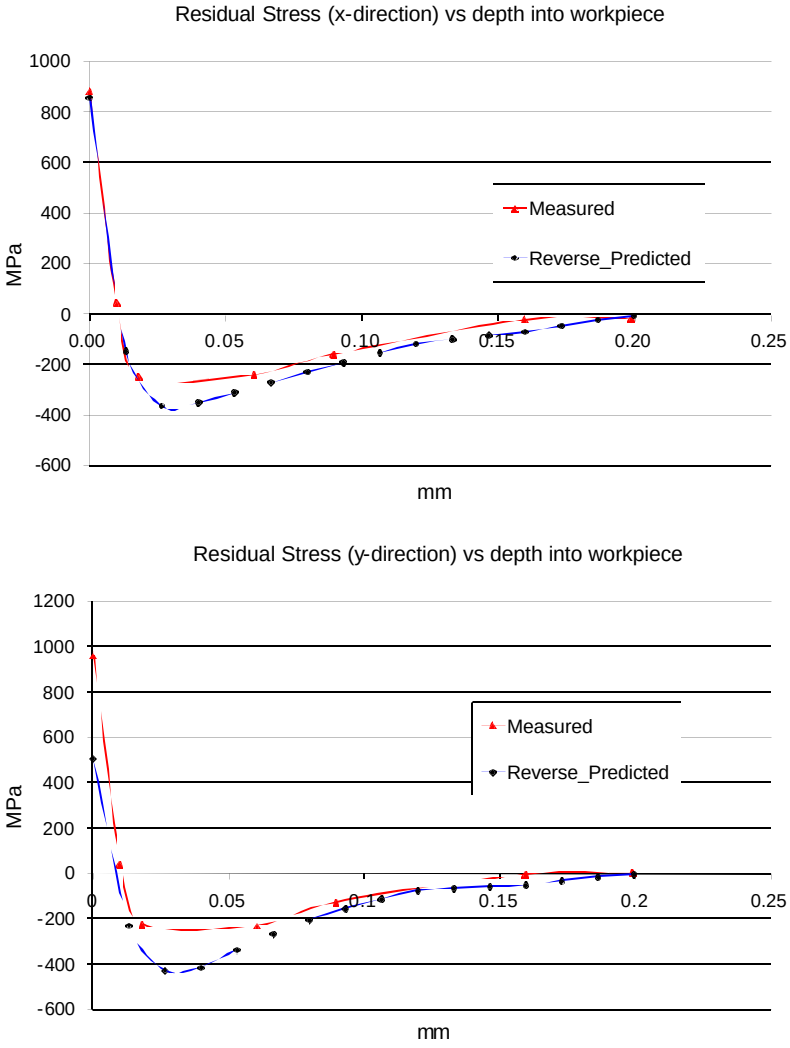

Figure 5-23. Residual stress profile in x and y direction for case 3

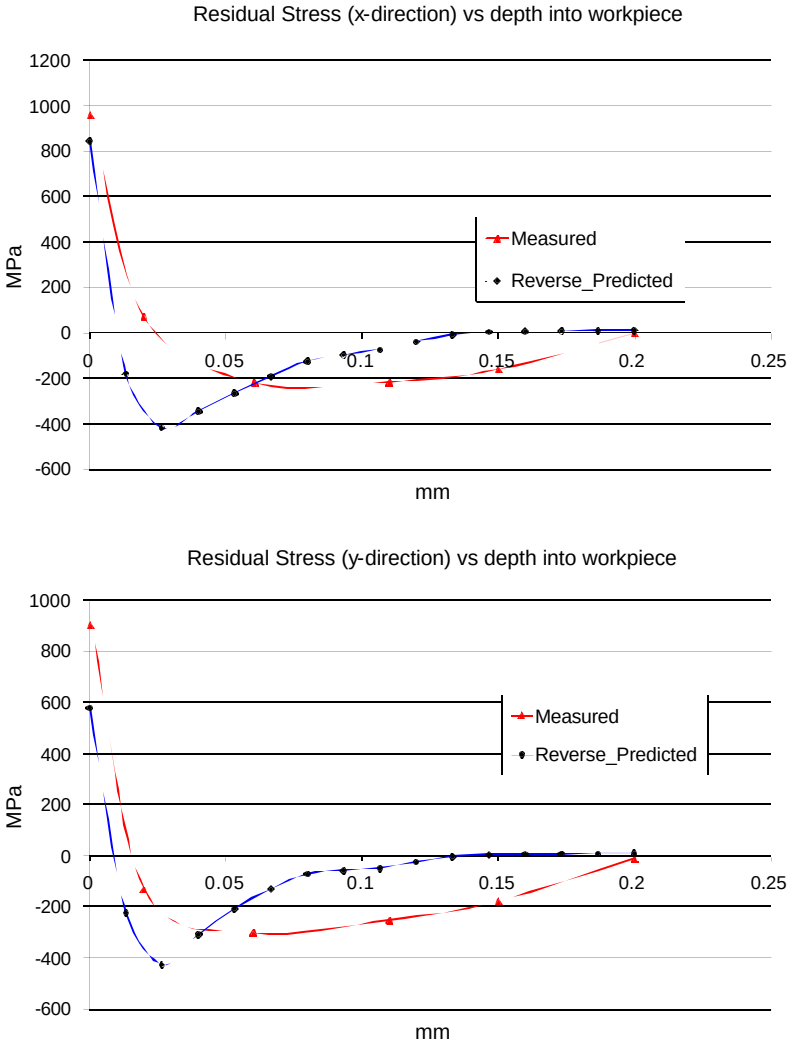

Figure 5-24. Residual stress profile in x and y direction for case 4

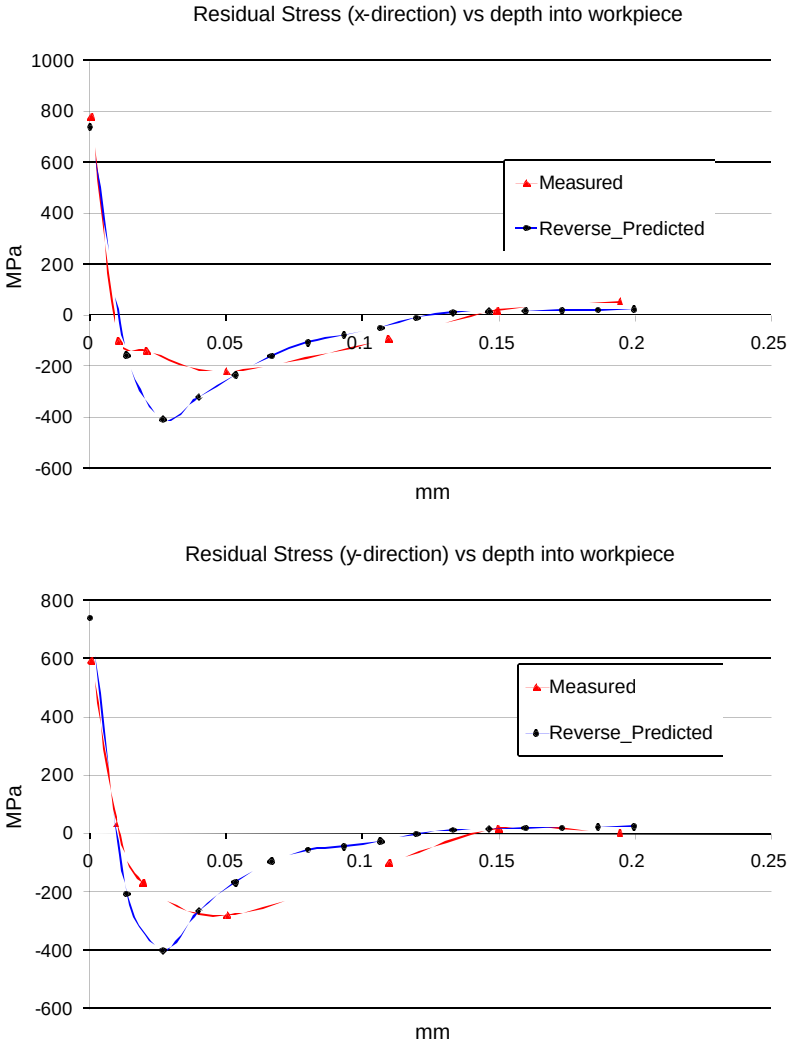

Figure 5-25. Residual stress profile in x and y direction for case 5

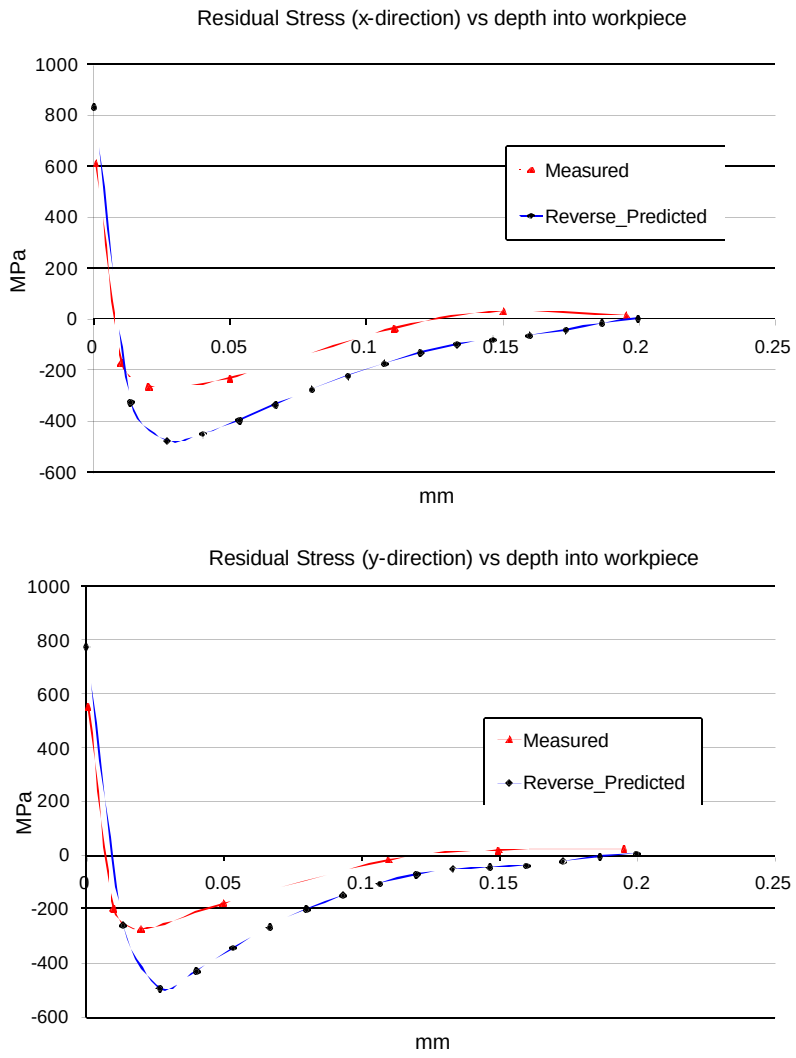

Figure 5-26. Residual stress profile in x and y direction for case 6

5.2 Modeling results for orthogonal cutting of AISI 316L

5.2.1 Depth of cut and edge radius prediction for AISI 316L

The depth of cut and edge radius were predicted for the orthogonal cutting of AISI 316L. Using this new material and a different set of depth of cut and edge radius

values, the reverse model was validated using the previous procedure. Table 5.3 shows the material properties used in the model. Table 5.4 gives experimental cutting conditions

Table 5-3 Additional material properties used in the model

Material	E (GPa)	ν	H (GPa)	ρ (kg/m^3)	k (W/m°C)	C_P (J/kg°C)	α ($°C^{-1}$)	T_m (°C)
AISI 316L	193	0.28	60	7750	16.2	500	16.2e-6	1400

Table 5-4 Cutting conditions for predicting residual stress for AISI 316L [89]

Case	Tool	Material	Edge Radius (mm)	Width of Cut (mm)	Feed (mm/rev)	Speed (m/s)
7	KC950	AISI 316L	0.050	4	0.100	1.67
8	KC950	AISI 316L	0.050	4	0.100	2.08
9	KC950	AISI 316L	0.050	4	0.250	2.08

The tool (KC950) used was tungsten carbide tool coated with a triple layer of TiC-TiN-TiN. The depth profiles of residual stress were determined using X-ray diffraction technique. For each case, the machined surfaces were "electrolytically" polished step-by-step in order to determine the evolution of the residual stresses with depth. The uncertainty on the residual stress data obtained was less than 50 MPa for depths of less than 200 mm, but reaches 150-200 MPa for greater depth values.

The comparison of the edge radius and depth of cut for case 7 is given in figures 5.20 and 5.21. The difference between the predicted values and cutting conditions is noticeable, as it should be expected.

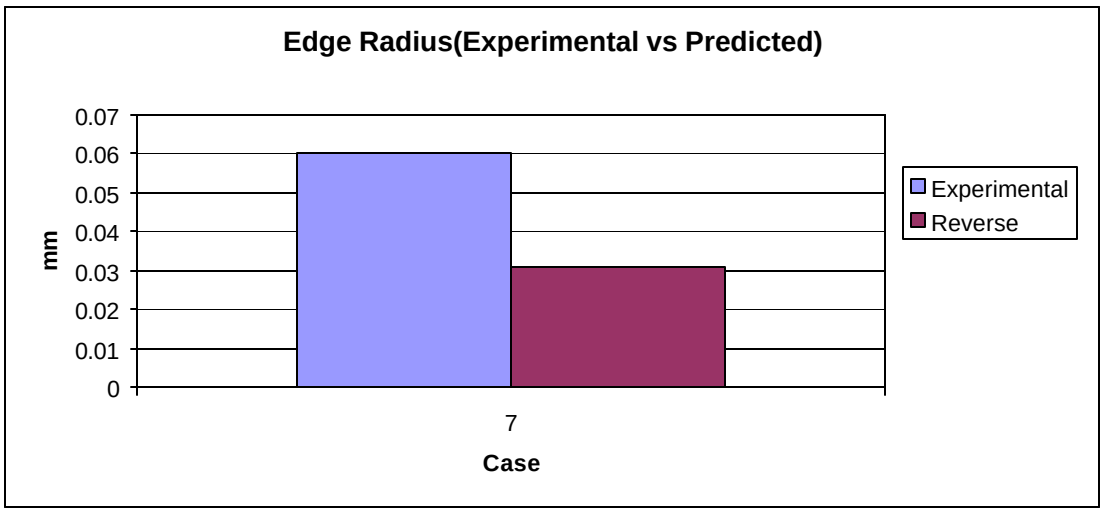

Figure 5-27 Edge radius comparison for the orthogonal cutting of AISI 316L (case 7)

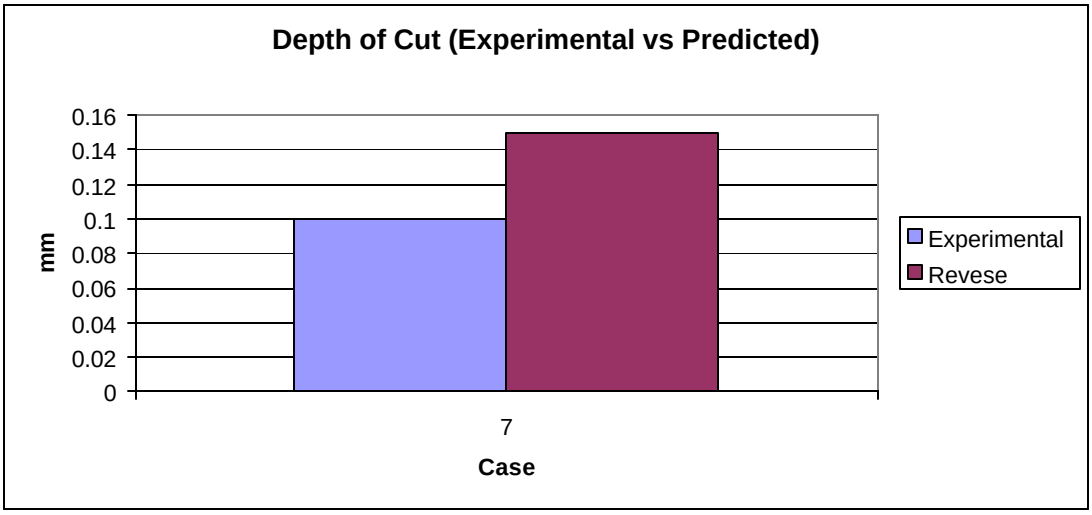

Figure 5-28 Depth of cut comparison for the orthogonal cutting of AISI 316L(case7)

5.2.2 Forward model performance

The "forward" model is then utilized to continue with the validation procedure. The performance of the aforementioned model is evaluated for cases 7-9. The residual

stress profiles in the x-direction given by the forward model and measured by X-ray diffraction are given in figures 5.22-5.24. The model was able to capture the trend of the stress profile.

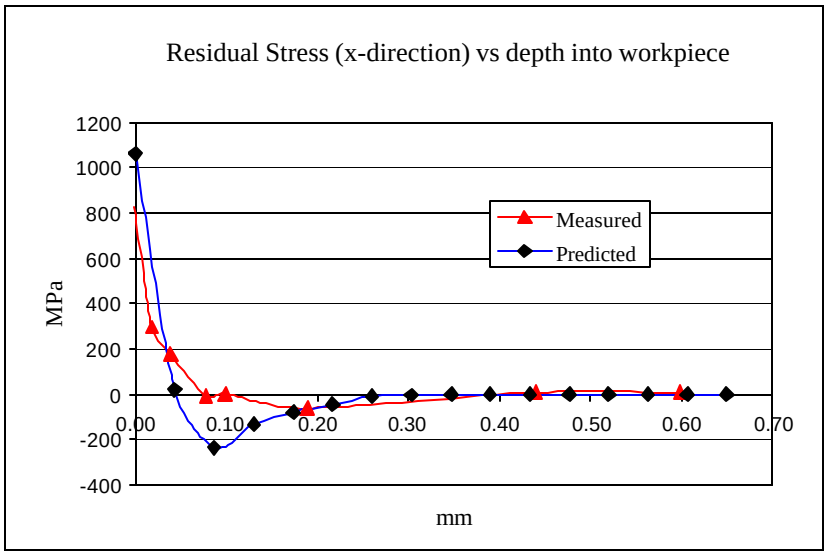

Figure 5-29 Residual stress profiles in the x-direction for case 7 [24]

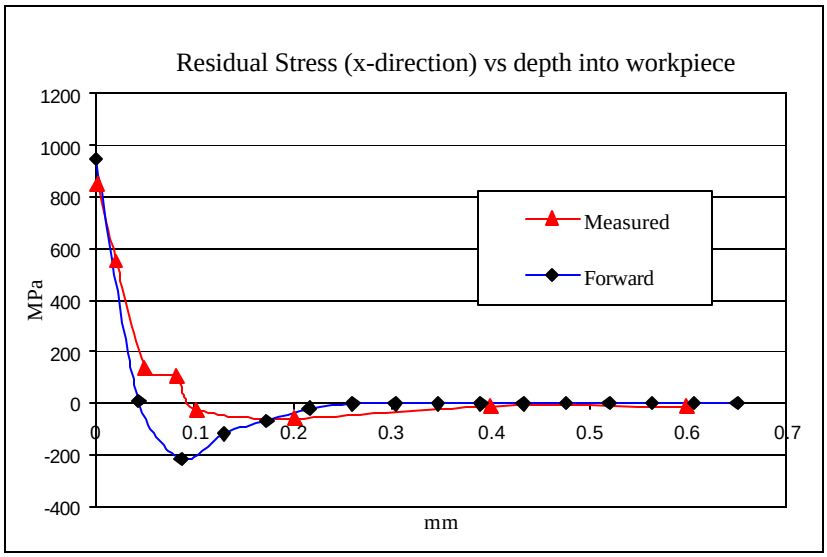

Figure 5-30 Residual stress profiles in the x-direction for case 8 [24]

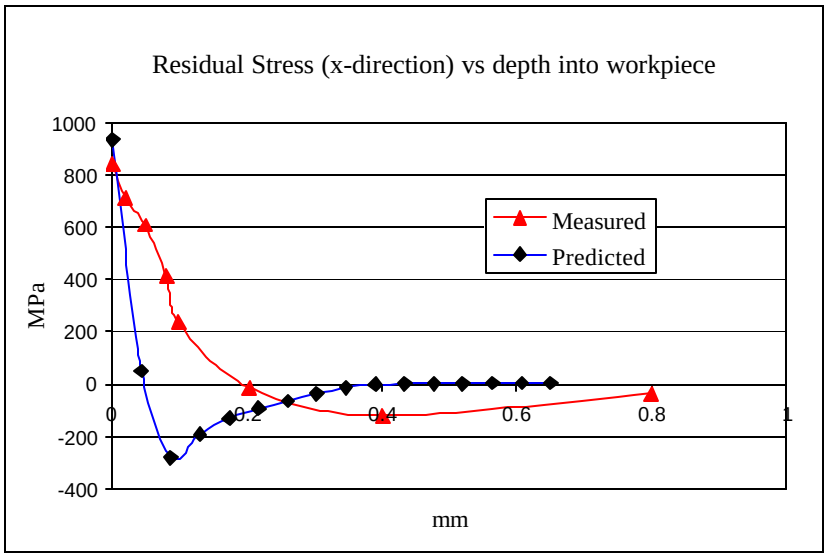

Figure 5-31 Residual stress profiles in the x-direction for case 9 [24]

5.2.3 Reverse and forward models comparison

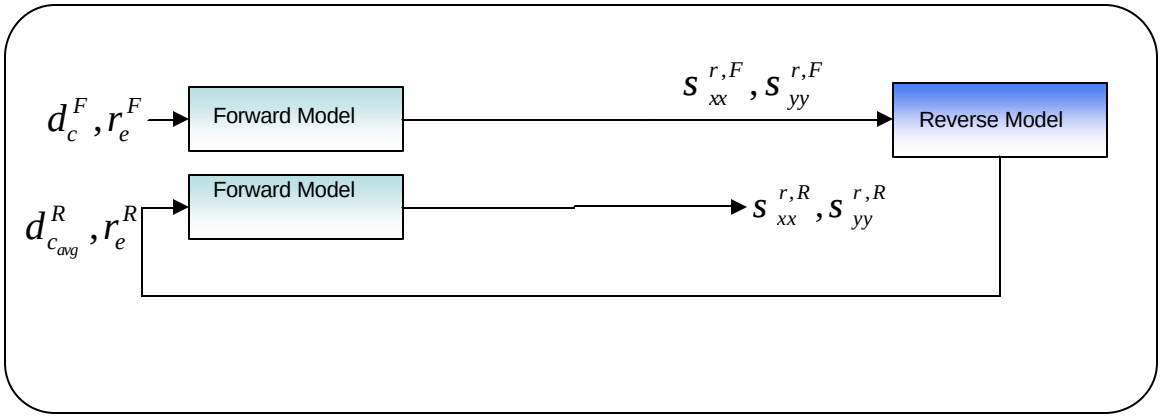

Figure 5-32 Validation scheme flowchart

The surface values of the residual stress ($s_{xx}^{r,F}(z_0), s_{yy}^{r,F}(z_0)$) are used as input to the reverse model. The comparison plots for the depth of cut used in the forward model and the depth of cut obtained by the reverse model are given in figure 5.25. Figure 5.26 shows the comparison plots for the edge radius for each case. Again the difference for the two parameters predicted is noticeable.

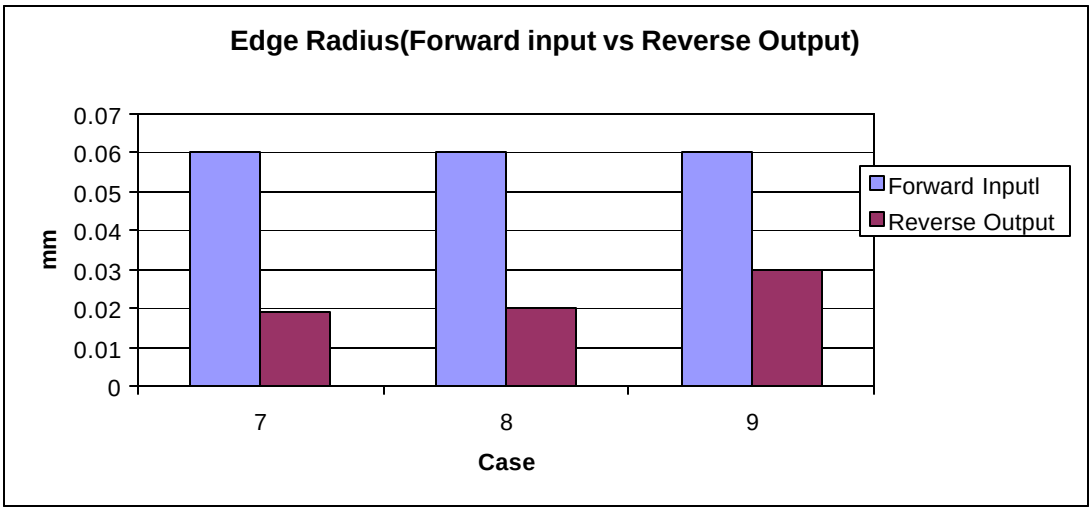

Figure 5-33 Edge radius comparison between the forward model input and the reverse model output

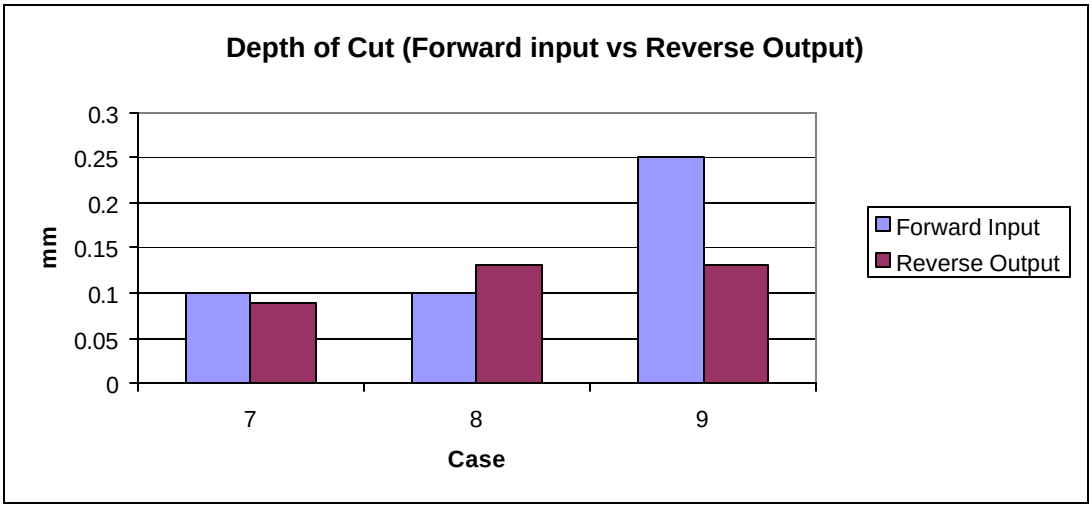

Figure 5-34 Depth of cut comparison between the forward model input and the reverse model output

The two parameters ($d_{c_{avg}}^{R}, r_e^{R}$) predicted are used as input to the "forward" model and a new set of residual profiles $s_{xx}^{r,R}(z_i), s_{yy}^{r,R}(z_i)$ is obtained. Figures 5.27 and 5.28 show the comparison between the surface residual stress $[s_{xx}^{r,F}(z_0), s_{xx}^{r,R}(z_0)]$ and $[s_{yy}^{r,F}(z_0), s_{yy}^{r,R}(z_0)]$. The average difference in the x-direction and y-direction were respectively about 19% and about 5%.

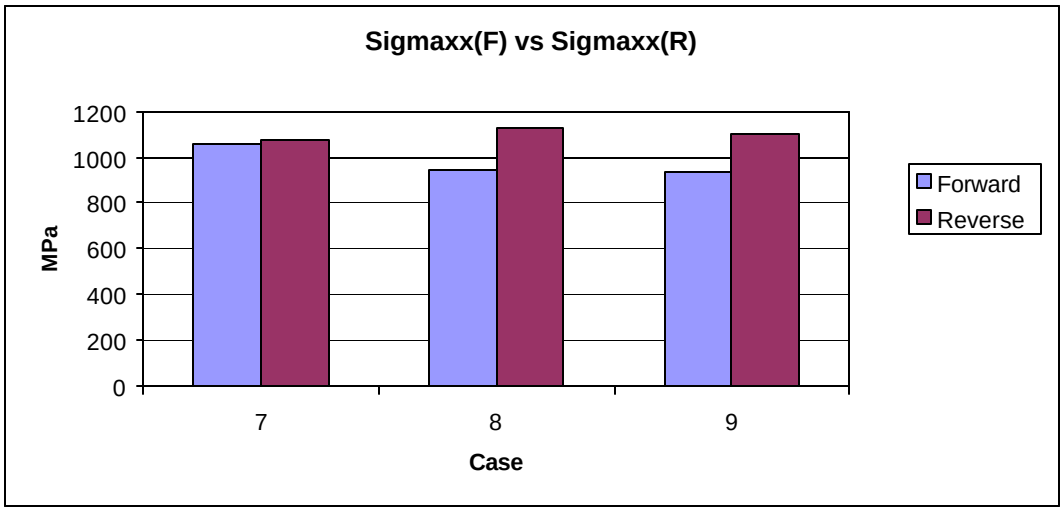

Figure 5-35 Comparison of the residual stress at the surface in the x-direction

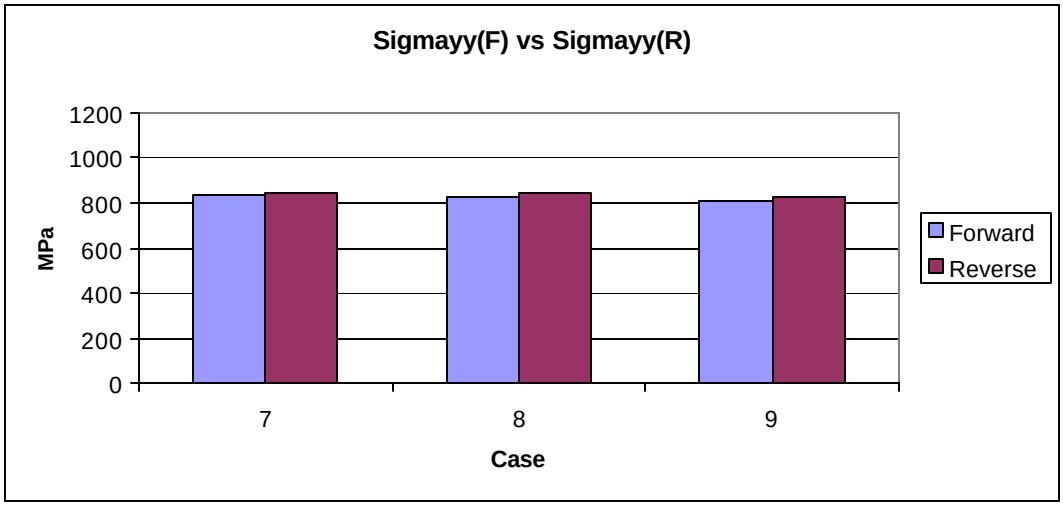

Figure 5-36 Comparison of the residual stress at the surface in the y-direction

The entire residual stress profiles obtained from using the predicted depth of cut and edge radius are compared with the input residual stress profiles to the reverse model. The comparison for each case is presented in figures 5.29 to 5.31.

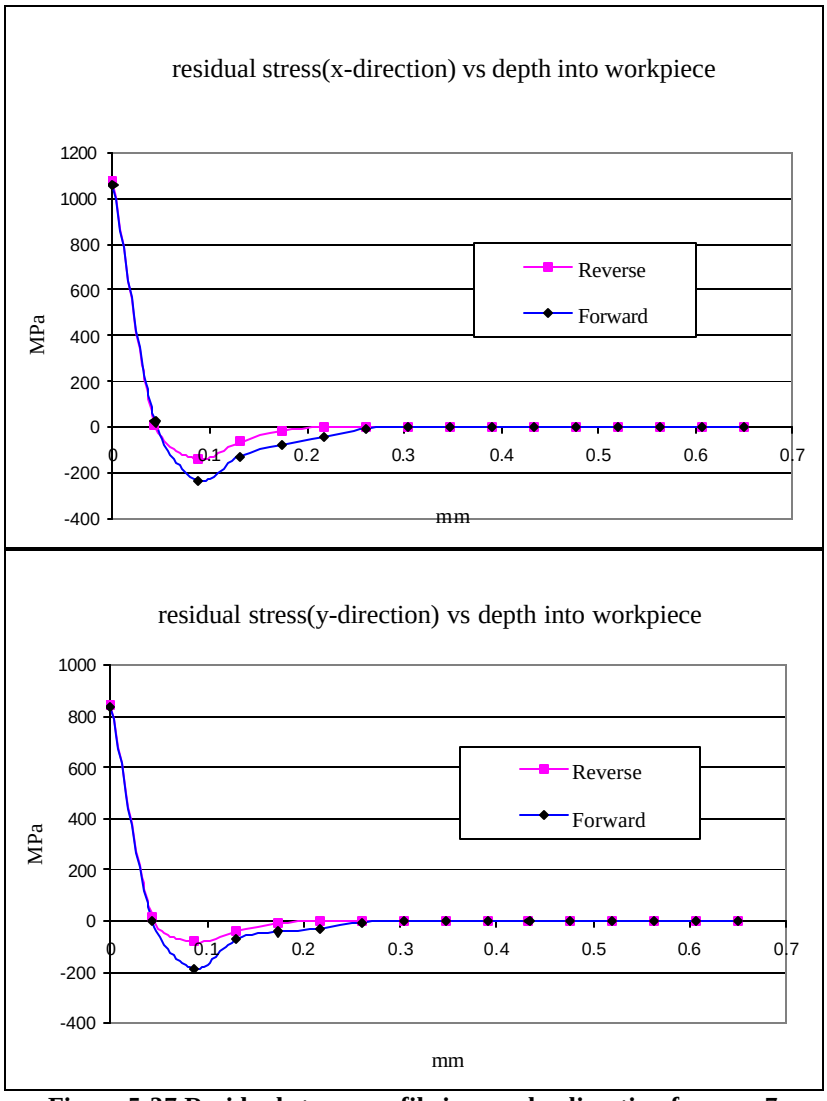

Figure 5-37 Residual stress profile in x and y direction for case 7

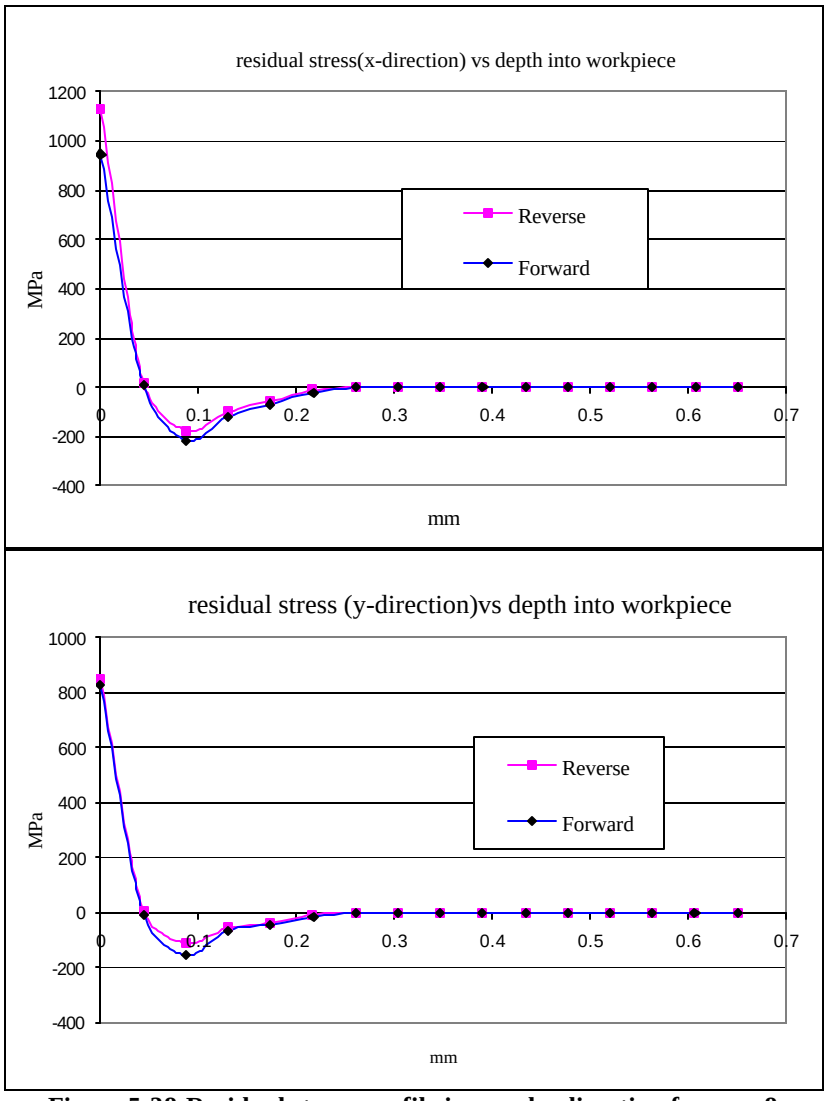

Figure 5-38 Residual stress profile in x and y direction for case 8

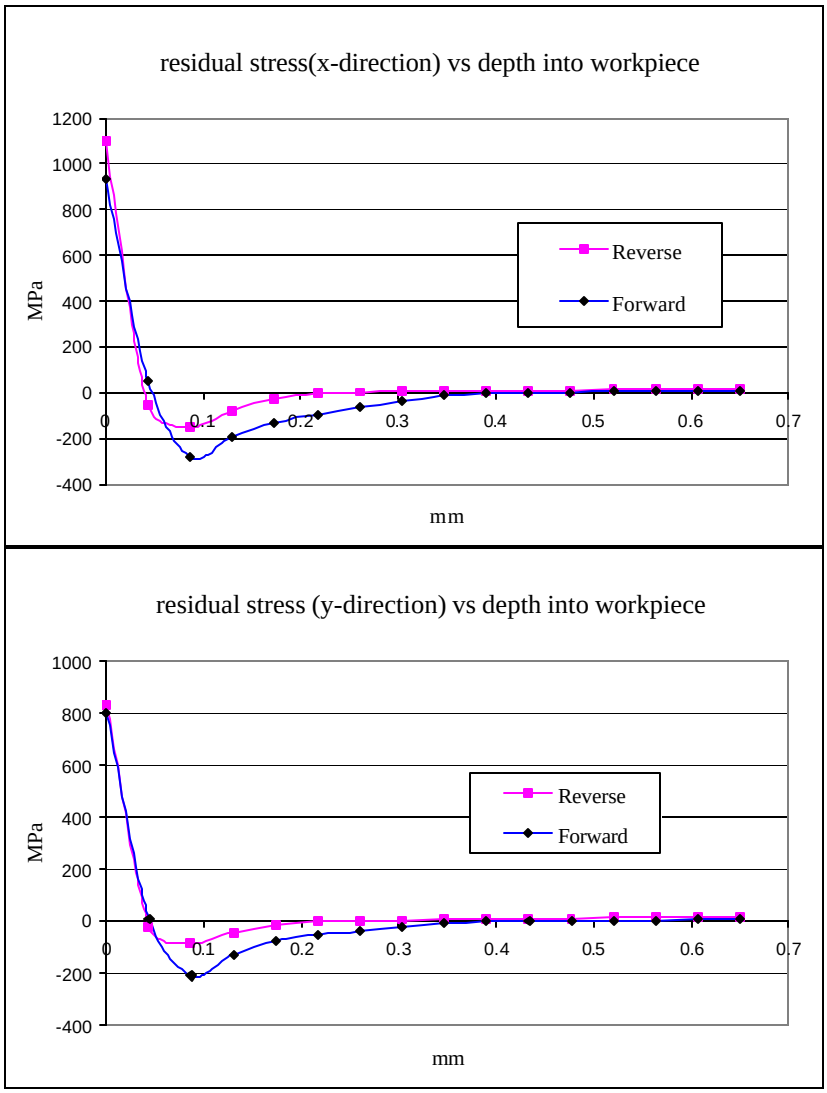

Figure 5-39 Residual stress profile in x and y direction for case 9

5.2.4 Validation using experimental data, reverse and forward model.

As in section 5.1.4, the validation procedure followed is shown in figure 5.40. The surface residual stresses value in the x and y directions obtained from x-ray diffraction are input to the reverse model. Then, the output of this model namely the depth of cut and edge radius are input the forward model. Finally, the predicted residual stress profiles are compared to the experimentally measured residual stress profiles for case 7 as shown in

figure 5-40. The predicted residual stress profile follows the trend of the measured profile.

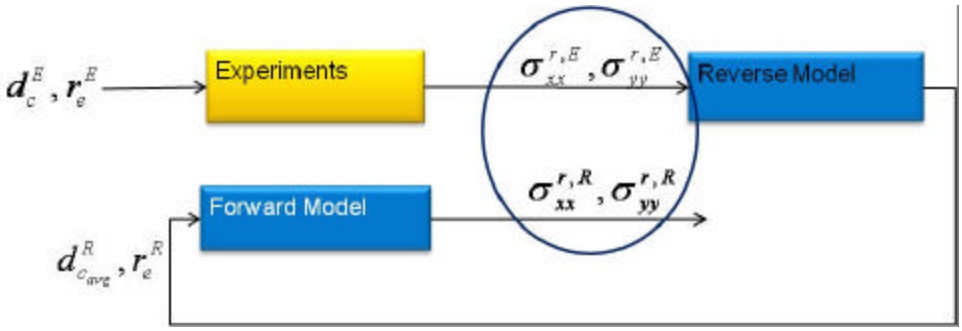

Figure 5-40 Validation Flowchart

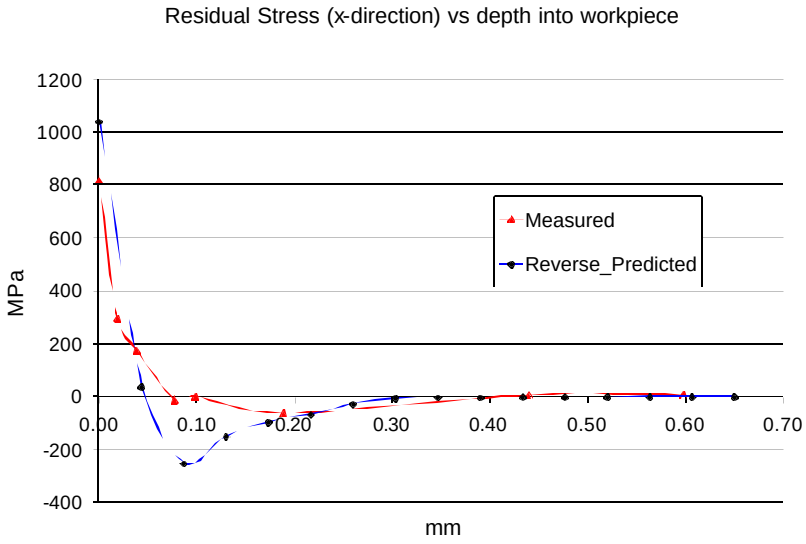

Figure 5-41 Residual stress profile in x and y direction for case 7

5.3 Force Estimation.

Using the reverse model, the cutting forces which comprise the ploughing forces and sharp cutting forces are estimated. In the following set of experiments conducted by MSaoubi (Table 5-5), the cutting speed was varied to capture the effect of the cutting speed on the cutting force required and the residual stress produced. The experimental

results show that an increase in cutting speed results in a decrease in cutting force. Higher cutting speeds produce higher temperatures in the shear zone. Consequently, the cutting force decreases due to thermal softening. Using the residual stress obtained from these experiments, the cutting forces are predicted by the reverse model. Figure 5.32 shows a comparison plot of the measured cutting forces and the predicted forces. The effect of cutting speed on the cutting force components is captured. As the cutting speed is increased, both the force components decrease. Further, the model gives a conservative prediction of the forces.

Table 5-5 Cutting conditions for predicting forces in AISI 316L

Case	Tool	Material	Edge Radius (mm)	Width of Cut (mm)	Feed (mm/rev)	Speed (m/s)
10	KC950	AISI 316L	0.050	4	0.100	1.67
11	KC950	AISI 316L	0.050	4	0.100	2.08
12	KC950	AISI 316L	0.050	4	0.100	2.50
13	KC950	AISI 316L	0.050	4	0.100	3.33

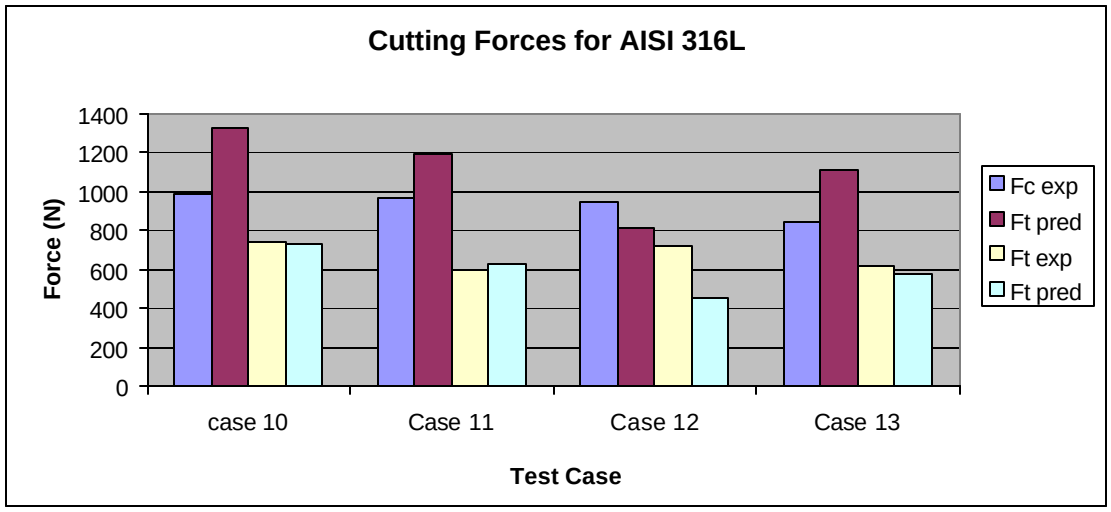

Figure 5-42 Cutting forces comparisons for AISI 316L

5.4 Compressive Surface Residual Stress

For all the experimental cases in this study, the residual stress values at the surface of the workpiece were tensile (positive). Although, compressive (negative) values of surface residual stress can be input to the reverse model, it will not be possible to obtain such surface residual stress values after an actual dry orthogonal cutting operation.

In the work of Okushima and Kakino [5], they studied the residual stresses caused by the mechanical effect of the ploughing force which exists at the tool edge and by thermal effect of the temperature distribution produced in orthogonal cutting. The model was validated using residual stresses data obtained from X-ray diffraction experiment. Their findings showed:

- Thermal effects lead to tensile residual stresses,
- Mechanical effects produced compressive residual stresses.

- Most importantly, it was found also that in most cases of practical cutting, tensile residual stresses are produced on the machined surface.

In section 4.1, an interpretation of the residual stress profile in the workpiece is given. It was mentioned that when the thermal strain e_S^T in the surface region S, are greater than plastic strain e_D^P in the sub-surface region D, the residual stress at the surface has to be tensile or positive. Thermal expansion strain is directly related to the temperature gradient as given by the following equation:

$$e_S^T = a\Delta T \qquad \textbf{Eq. 5-1}$$

During an orthogonal cutting operation, the maximum workpiece temperature occurs at the surface near the tool tip, and the temperature drops quickly behind the tool tip. Although, the exact temperature profile depends on the cutting parameters and the thermal properties of the workpiece material, a typical profile is shown in figure 5-43. With the high temperature at the surface, the thermal strain, at the surface, is greater than the plastic strain in the subsurface. Thus, tensile residual stress values should be expected at the surface.

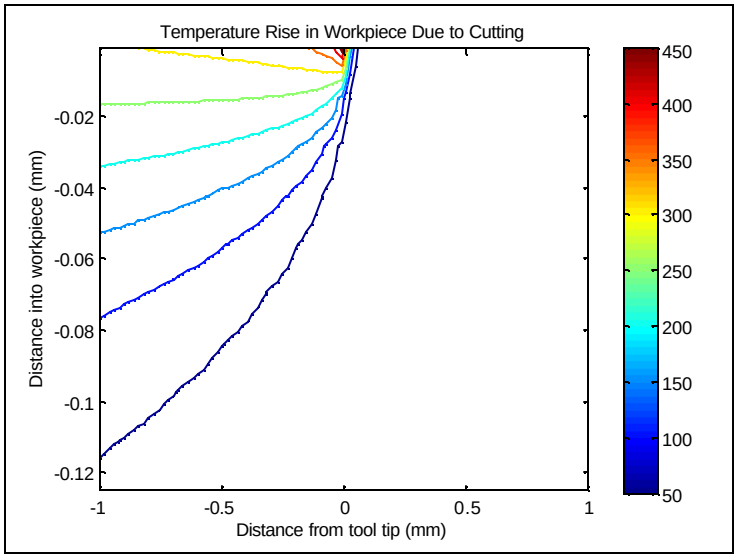

Figure 5-43 Temperature profiles beneath tool due to cutting[24]

A set of surface residual stress values are input to the reverse model in order to predict the depth of cut and edge radius. The depth of cut and edge radius predicted are indeed not practical.

Table 5-6 Depth of cut and Edge radius predictions using compressive surface residual stresses

$s_{cut}^{surfaceresidual}$	$s_{transverse}^{surfaceresidual}$	Depth of cut (mm)	Edge radius (mm)
-50	-50	1.53	0.23
-100	-100	1.86	0.28
-200	-200	2.94	0.5
-400	-400	11.59	1.78
-600	-600	1177.97	180.53

If the temperature in the cutting region was not significant, which could be achieved possibly using coolant, the thermal strain at the surface will be less than the plastic strain at the sub-surface $e_D^P > e_S^T \geq 0$ [18]. Thus, the compressive surface residual stress could be obtained under practical cutting conditions.

5.5 Quick Method to predict cutting process parameters

The methodology developed could seem a bit tedious for a machinist wanting a quick estimate of the depth of cut and tool edge radius before starting an orthogonal cutting process. A simpler method is necessary if such a quick estimation is needed. This method is developed, using the following assumptions:

- The shear angle during an orthogonal cutting process remains at 25º,

- The poisson's ratio is equal to 0.3
- The Hertzian stress components in the cut direction and in the direction normal to the cutting plane have the same magnitude.

For alloy steels, and given the surface value of the residual stress in the cut and transverse direction ($s_{xx}^{residual}(z_0), s_{yy}^{residual}(z_0)$) in MPa, the following steps can followed to estimate the depth of cut and edge radius:

1. Determine **A**

$$\mathbf{A} = -1504 - 6.76 s_{cut}^{surfaceresidual} + 4.37 s_{transverse}^{surfaceresidual} \quad \textbf{Eq. 5-2}$$

2. Determine **B**

$$\mathbf{B} = 846 + 3.81 s_{cut}^{surfaceresidual} - 2.46 s_{transverse}^{surfaceresidual} \quad \textbf{Eq. 5-3}$$

3. Determine **C**

$$\mathbf{C} = 0.001\sqrt{0.4\mathbf{A}^2 + 3\mathbf{B}^2} \quad \textbf{Eq. 5-4}$$

4. Finally the depth of cut and edge radius are obtained by the following:

$$d = \frac{10^{\frac{0.3-\log(C)}{0.46}} + 10^{\frac{0.19-\log(C)}{0.46}}}{2}$$
$$h = 0.2d \quad \textbf{Eq. 5-5}$$

Equations 5-1 and 5-2 are respectively equations 4-23 and 4-24. Section 4.2.2 should be revisited if the more information regarding the derivation is needed. Equation 5.3 is a simplified version of equation 4-26 where the Hertzian stress components in the cut direction and in the direction normal to the cutting plane have the same magnitude and the poisson's ratio is equal to 0.3. The terms given by equation 5-4 are derived from

the equations presented in section 4.4 and 4.5. using the assumption that the shear and prow angle are equal to 25 º

The residual stress surface values, given by the "forward" model for case 1 through case 6 in section 5.1.2, are used to determine the difference in depth of cut and edge radius that would be obtained from the model and the quick method presented in this section. As shown in table 5.6, the difference in depth of cut remained under 3% and the difference in edge radius shows a difference of less than 1% for 4 of the cases. For case 2 and case 4, the difference was respectively equal to 33.7% and 6.7%. Although the difference shown is minimal, this quick method is limited to tensile surface residual stress values, and to the orthogonal cutting process. Using the forward method, residual profiles using the depth of cut and edge radius given by both methods generated. Table 5.7 gives the surface residual stress values difference from both methods, and figures 5.33-5.38 shows the entire residual stress profile obtained for each case.

Table 5-7 % difference between the depth of cut and edge radius given by both methods

	% difference [Depth of cut]	% difference [Edge radius]
Case 1	1.9	0.6
Case 2	1.8	33.7
Case 3	2.6	0.6
Case 4	2.4	6.7
Case 5	1.7	0.6
Case 6	2.4	0.9

Table 5-8 % difference between the surface value using the parameters predicted by both methods

	% difference [residual stress (cut-direction)]	% difference [residual stress (transverse-direction)]
Case 1	0.0	0.0
Case 2	8.1	2.8
Case 3	0.0	0.0
Case 4	7.7	2.6
Case 5	6.6	2.3
Case 6	0.0	0.0

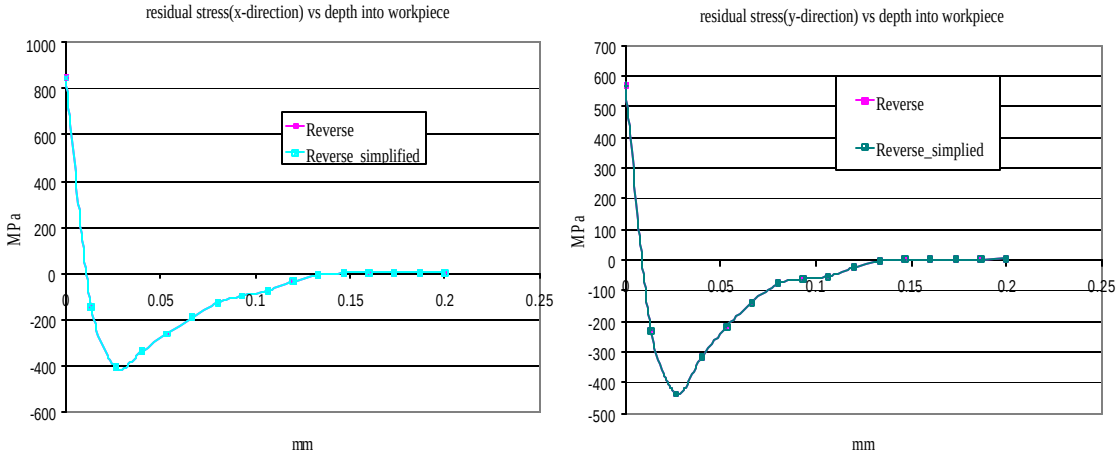

Figure 5-44 Residual stresses estimation in the x and y directions based on the predicted parameters given by both methods case 1

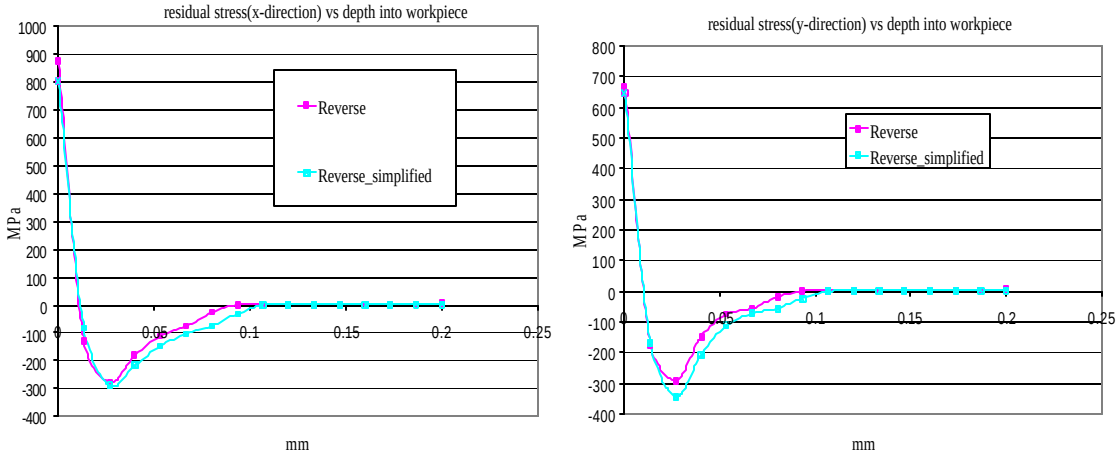

Figure 5-45 Residual stresses estimation in the x and y directions based on the predicted parameters given by both methods case 2

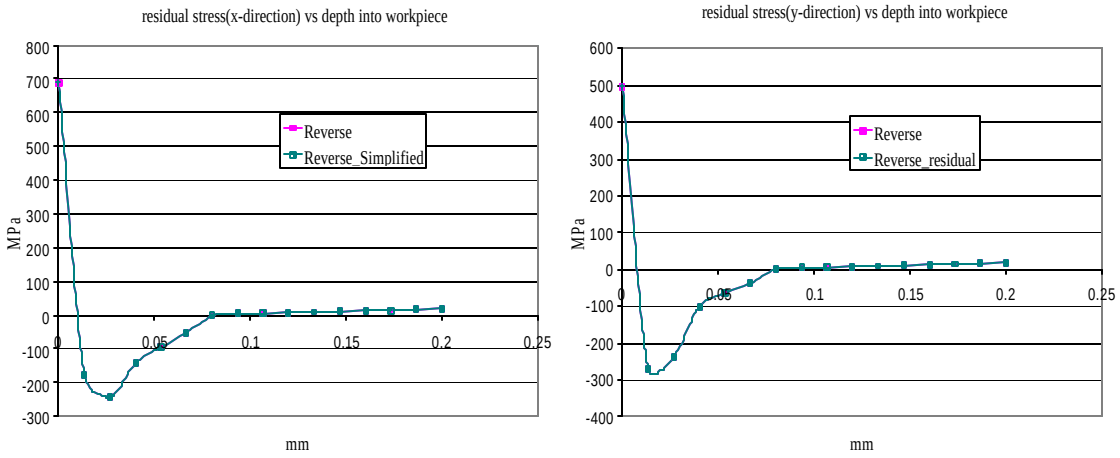

Figure 5-46 Residual stresses estimation in the x and y directions based on the predicted parameters given by both methods case 3

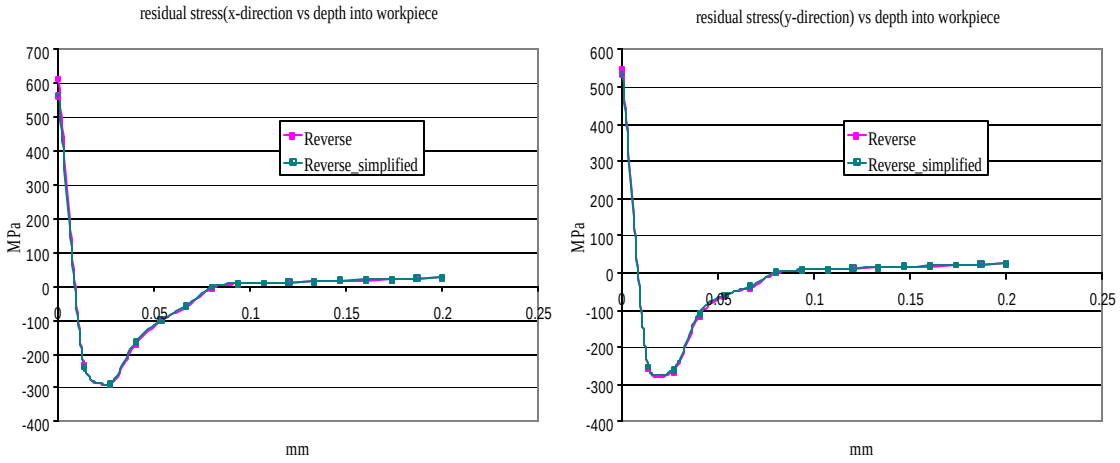

Figure 5-47 Residual stresses estimation in the x and y directions based on the predicted parameters given by both methods case 4

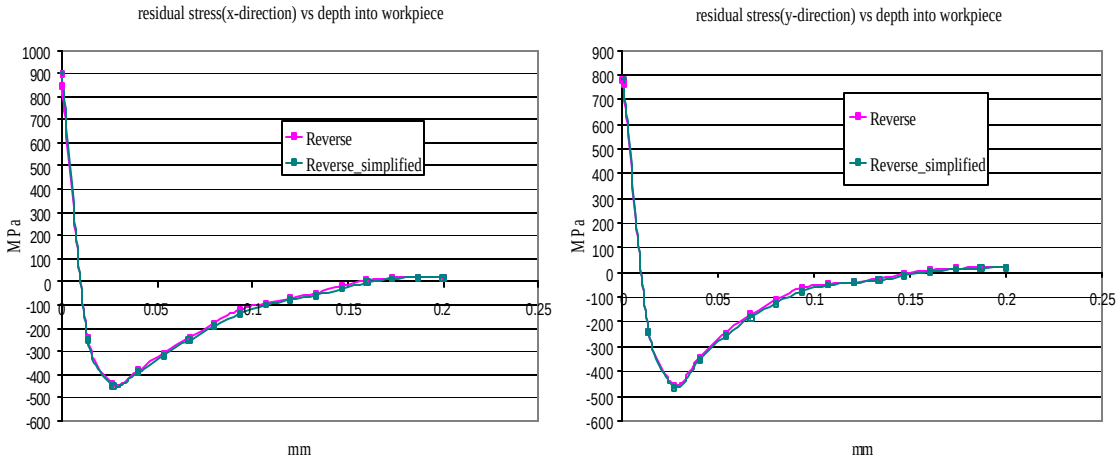

Figure 5-48 Residual stresses estimation in the x and y directions based on the predicted parameters given by both methods case 5

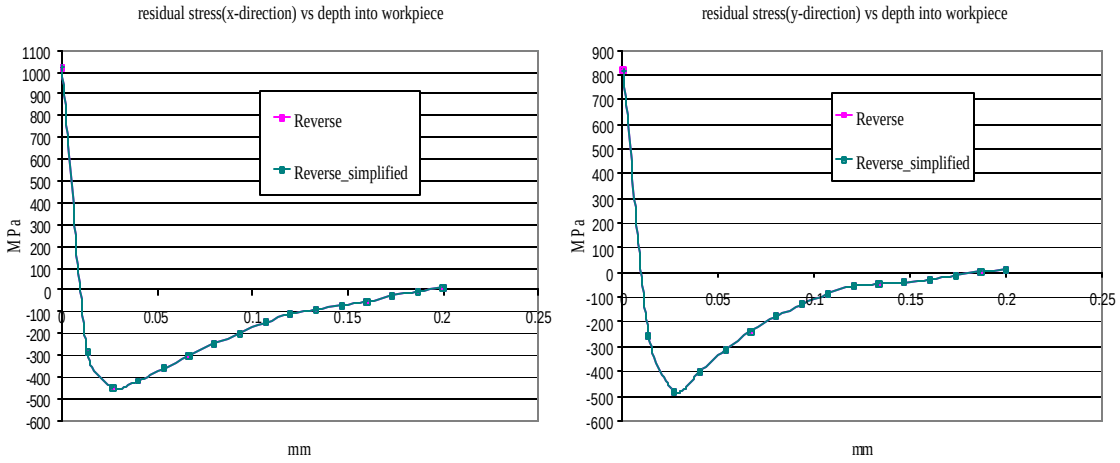

Figure 5-49 Residual stresses estimation in the x and y directions based on the predicted parameters given by both methods case 6

5.6 Summary

In this chapter, the modeling approach proposed in chapter 4 is applied to orthogonal cutting. Depth of cut and edge radius predictions were made for orthogonal cutting of AISI 4340 and AISI 316L. Even though there was a noticeable difference between the predicted values and the experimental values used, the residual stresses produced using these values are comparable to the measured residual stresses. These results shows that the right combinations of depth of cut and edge radius can be predicted using surface residual stress information. Further the model was able to capture the cutting force required for a successful machining operation. An analysis was presented to discuss that how compressive surface residual stresses, which can be input to the reverse model, will not lead to practical cutting conditions. In section 5.5, a quick method was presented to allow for a quick estimate of the depth of cut and the edge radius from residual stresses.

****

CHAPTER 6

CONCLUSIONS

6.1 Summary

This dissertation presents a method of predicting depth of cut, tool edge radius and cutting forces from residual stresses required in machined part. The inverse modeling techniques are derived from a physics-based modeling approach to the machining process and analytical modeling of residual stress prediction. In chapter 3, the physics based modeling approach and the analytical modeling of residual stress prediction are presented. In chapter 4, the different inverse modeling techniques constituting the reverse methodology are presented. In chapter 5, the model predictions are validated using experimental data. The results proved that the methodology can be adopted to give realistic recommendations on the depth of cut, the tool edge radius and the cutting force required to achieve a desired residual stresses at the surface.

6.2 Conclusions

The research presented in this dissertation was driven by the need for a methodology to allow manufacturers to design around the residual stress required or desired in a machined component for a specific application.

Currently, the process planning methods do not address directly the issues of part performance and functionality. Tremendous improvement of the overall manufacturing

process of precision products could be achieved if the parts performance and functionality could be at the center of the planning process. Although, a tremendous amount of work has been done to characterize the effect of cutting parameters such as width and depth of cut, speed, and tool geometry (i.e. edge radius) on the residual stress that is produced during cutting, these models do not provide a methodology to specify either machining process or tool geometry parameters from a desired residual stress profile into the workpiece. The methodology, developed in this research, allows residual stress to be truly engineered in a workpiece by enabling the prediction of an optimal set of cutting process and tool geometry parameters from a given residual stress profile. The main objectives were to (1) develop a methodology to predict the depth of cut, the tool edge radius, and the cutting forces required from the surface residual stress needed in a machined component and (2) validate the methodology with experimental data. The methodology was based on developing inverse solutions to different methods (residual stresses from Hertzian stresses, shear angle estimation from process parameters, cutting forces from process parameters, etc..) that when combined gave an analytical description of the cutting process.

The depth of cut and edge radius prediction were made for orthogonal cutting of AISI 4340 and AISI 316L. Even though there was a noticeable difference between the predicted values and the experimental values used, the residual stresses produced using these values are comparable to the measured residual stresses. These results shows that the right combinations of depth of cut and edge radius can be predicted using surface residual stress information. Further, the model was able to capture the cutting force required for a successful machining operation. The influence of cutting speed on the

cutting forces was also captured by the model. In addition, a simple method was also presented which allows for a quick estimate of the depth of cut and the edge radius from surface residual stress values.

The research has shown that it is possible to extract the cutting process parameters and also cutting forces from residual stresses. The modeling techniques developed are well suited for an accurate estimate of these parameters.

6.3 Contributions

The modeling techniques presented in this dissertation provided a new method in engineering residual stress by predicting the depth of cut, the tool edge radius and the cuuting forces required to achieve the stress state needed. The intellectual contributions of the research presented are as follows:

- Developed an analytical model to predict the depth of cut, the tool edge radius and the cutting force required based on residual stress requirement.
- Developed a quick and effective method to estimate these aforementioned parameters for alloys steels.
- Validated the model with:
    - experimental data for AISI 4340 and AISI 316L
    - analytical predictive residual stress modeling results
- Proved the possibility to extract cutting process information from the workpiece post process stress profile.

Many other benefits could be derived from such methodology:

- Achievement of a better control over the surface integrity of a part.

- Improvement of Hard Turning competitiveness in replacing multiple grinding processing steps.
- Reduction of trial-and-error tooling design cycle time since a tool geometry information can be extracted from residual stress profile requirement

6.4 Future work

The current model provides a method extracting cutting process parameters from surface residual stress requirement. If offers a quick and effective method to predict these parameters. Nonetheless, there are opportunities of improving the predictive capability of the model.

In the model, a linear relationship between the residual stress and the Hertzian stress per unit depth into the workpiece is used. A neural network could be used to establish a more robust relationship between these two stress parameters. Further, a relationship between the entire residual stress profile and Herztian stress profile could be established. Such improvement could provide a way in extracting the rest of the cutting process parameters such as the cutting speed, the width of cut, and the rake angle.

Since the model is based on finding the inverse of relationship among the critical parameters in the machining process, its limitation is partly based on how well the analytical description of the machining process was done in the past. Needless to say that improvement is needed in this area. The friction coefficient is treated as a constant in this work. However, this coefficient does affect the residual stress profile obtained after machining. A more analytical approach is necessary to quantify the effect of friction. A

physics-based model for determining the friction coefficient can be used to determine a range of friction values consistent with the machining process being studied.

Improvement in residual stresses measurement is also needed. Measuring residual stresses is still a laborious task with error ranging from 50 MPa to 200Mpa for a good measurement. Developing alternatives techniques to measure sub-surface stresses such as the magnetoelastic Barkhausen noise method or ultrasonic sensing will ease the tremendous experimental efforts necessary to acquire residual stress data. These advancements in measuring capabilities may help greatly the general modeling capabilities.

****

REFERENCES

1. Toenshoff, H.K., C. Arendt, and R.B. Amor, *Cutting of hardened steel.* CIRP Annals - Manufacturing Technology, 2000. **49**(2): p. 547-566.

2. Jang, D.Y., et al., *Surface residual stresses in machined austenitic stainless steel.* Wear, 1996. **194**(1-2): p. 168-173.

3. Wu, D.W. and Y. Matsumoto, *Effect of hardness on residual stresses in orthogonal machining of AISI 4340 steel.* Journal of Engineering for Industry, Transactions of the ASME, 1990. **112**(3): p. 245-252.

4. Henriksen, E.K., *Residual stresses in machined surfaces.* American Society of Mechanical Engineers -- Transactions, 1951. **73**(1): p. 69-76.

5. Okushima, K. and Y. Kakino, *Residual stress produced by metal cutting.* 1971. **20**(1): p. 13-14.

6. Tsuchida, K., Y. Kawada, and S. Kodama, *Study on the residual stress distributions by turning.* 1975. **18**(116): p. 123-130.

7. Liu, C.R. and M.M. Barash, *Variables Governing Patterns of Mechanical Residual Stress in a Machined Surface.* 1982. **104**(3): p. 257-264.

8. Sadat, A.B. and J.A. Bailey, *Residual stresses in turned AISI 4340 steel.* Experimental Mechanics, 1987. **27**(1): p. 80-5.

9. Sadat, A.B. and M.Y. Reddy, *Surface Integrity of Inconel-718 Nickel-Base Superalloy using Controlled and Natural Contact Length Tools. Part II: Unlubricated.* Experimental Mechanics, 1993. **33**(4): p. 343-348.

10. Schlauer, C., R.L. Peng, and M. Oden, *Residual stresses in a nickel-based superalloy introduced by turning.* Materials Science Forum, 2002. **404-407**: p. 173-8.

11. Agha, S.R. and C.R. Liu, *Experimental study on the performance of superfinish hard turned surfaces in rolling contact.* Wear, 2000. **244**(1-2): p. 52-59.

12. Jacobson, M., *Surface integrity of hard-turned M50 steel.* Proceedings of the Institution of Mechanical Engineers, Part B: Journal of Engineering Manufacture, 2002. **216**(1): p. 47-54.

13. Huddle, D., *Turning to Hard Turning.* Tooling and Production, 2001.

14. Matsumoto, Y., M.M. Barash, and C.R. Liu, *Effect of Hardness on the Surface integrity of AISI 4340 Steel.* Journal of Engineering for Industry, Transactions ASME, 1986. **108**(3): p. 169-175.

15. Thiele, J.D. and S.N. Melkote, *Effect of tool edge geometry on workpiece sub-surface deformation and through-thickness residual stresses for hard-turning of AISI 52100 steel.* Technical Paper - Society of Manufacturing Engineers. MR, 1999(MR99-167): p. 1-6.

16. Thiele, J.D. and S.N. Melkote, *Effect of cutting edge geometry and workpiece hardness on surface generation in the finish hard turning of AISI 52100 steel.* Journal of Materials Processing Technology, 1999. **94**(2): p. 216-226.

17. Fuh, K.-H. and C.-F. Wu, *Residual-stress model for the milling of aluminum alloy (2014-T6).* Journal of Materials Processing Technology, 1995. **51**(1-4): p. 87-105.

18. Jacobus, J.K., R.E. DeVor, and S.G. Kapoor, *Machining-induced residual stress: experimentation and modeling.* Journal of Manufacturing Science and Engineering, 2000. **122**: p. 20-31.

19. Enahoro, H.E. and P.L.B. Oxley, *Flow along tool-chip interface in orthogonal metal cutting.* Journal of Mechanical Science, 1966. **8**(1): p. 36-41.

20. Merwin, J.E., Johnson, K.L., *An Analysis of Plastic Deformation in Rolling Contact*. Proeedings, Institution of Mechanical Engineers, London, 1963. **177**(25): p. 676-685.

21. El-Axir, M.H., *A method of modeling residual stress distribution in turning for different materials.* International Journal of Machine Tools and Manufacture, 2002. **42**(9): p. 1055-1063.

22. Mittal, S. and C.R. Liu, *A method of modeling residual stresses in superfinish hard turning.* Wear, 1998. **218**(1): p. 21-33.

23. Capello, E., *Residual stresses in turning Part 1: Influence of process parameters.* Journal of Materials Processing Technology, 2005. **160**(2): p. 221-8.

24. Su, J.-C., *Residual stress modeling in machining processes*. 2006, Georgia Institute of Technology: Atlanta.

25. Mishra, A. and T. Prasad, *Residual stresses due to a moving heat source.* International Journal of Mechanical Sciences, 1985. **27**(9): p. 571-581.

26. Lin, Z.-C., Y.-Y. Lin, and C.R. Liu, *Effect of thermal load and mechanical load on the residual stress of a machined workpiece.* International Journal of Mechanical Sciences, 1991. **33**(4): p. 263-278.

27. Shih, A.J., *Finite element analysis of the rake angle effects in orthogonal metal cutting.* International Journal of Mechanical Sciences, 1996. **38**(1): p. 1-17.

28. Hua, J., et al., *Effect of feed rate, workpiece hardness and cutting edge on subsurface residual stress in the hard turning of bearing steel using chamfer + hone cutting edge geometry.* Materials Science and Engineering A, 2005. **394**(1-2): p. 238-248.

29. Liu, C.R. and Y.B. Guo, *Finite element analysis of the effect of sequential cuts and tool-chip friction on residual stresses in a machined layer.* International Journal of Mechanical Sciences, 2000. **42**(6): p. 1069-1086.

30. Guo, Y. and C. Liu, *FEM Analysis of Mechanical State on Sequentially Machined Surfaces.* Machining Science & Technology, 2002. **6**(1): p. 21.

31. Salio, M., T. Berruti, and G. De Poli, *Prediction of residual stress distribution after turning in turbine disks.* International Journal of Mechanical Sciences, 2006. **48**(9): p. 976-984.

32. Nasr, M.N.A., E.G. Ng, and M.A. Elbestawi, *Modelling the effects of tool-edge radius on residual stresses when orthogonal cutting AISI 316L.* International Journal of Machine Tools and Manufacture, 2007. **47**(2): p. 401-411.

33. Guo, Y.B. and C.R. Liu, *3D FEA Modeling of Hard Turning.* Journal of Manufacturing Science and Engineering, 2002. **124**(2): p. 189-199.

34. Liu, T.I., W.Y. Chen, and K.S. Anatharaman, *Intelligent Detection of Drill Wear.* Mechanical Systems and Signal Processing, 1998. **12**(6): p. 863-873.

35. Dimla, D.E. and P.M. Lister, *On-line metal cutting tool condition monitoring.: II: tool-state classification using multi-layer perceptron neural networks.* International Journal of Machine Tools and Manufacture, 2000. **40**(5): p. 769-781.

36. Zuperl, U., et al., *A hybrid analytical-neural network approach to the determination of optimal cutting conditions.* Journal of Materials Processing Technology, 2004. **157-158**: p. 82-90.

37. Umbrello, D., et al., *An ANN approach for predicting subsurface residual stresses and the desired cutting conditions during hard turning.* Journal of Materials Processing Technology, 2007. **189**(1-3): p. 143-152.

38. Sick, B., *On-line and Indirect Tool Wear Monitoring in Turning with Artificial Neural Networks: A Review of More than a Decade of Research.* Mechanical Systems and Signal Processing, 2002. **16**(4): p. 487-546.

39. Leem, C.S. and D.A. Dornfeld, *Design and Implementation of Sensor-Based Tool Wear Monitoring Systems.* Mechanical Systems and Signal Processing, 1996. **10**(4): p. 439-458.

40. Silva, R.G., et al., *The Adaptability of a Tool Wear Monitoring System under Changing Cutting Conditions.* Mechanical Systems and Signal Processing, 2000. **14**(2): p. 287-298.

41. Gao, Z. and T. Mura, *On the inversion of residual stresses from surface displacements.* Journal of Applied Mechanics, Transactions ASME, 1989. **56**(3): p. 508-513.

42. Lin, Z.-C. and C.-k. Chen, *Inverse calculation of the friction coefficient during the warm upsetting of molybdenum.* International Journal of Mechanical Sciences, 2005. **47**(7): p. 1059-1078.

43. Tikhonov, A.N.A., V.Y., ed. *Solutions of ill-posed problems.* Scripta series in mathematics. Vol. 1. 1977, Winston ; distributed solely by Halsted Press,: Washington : New York :. xiii, 258 p. :.

44. Sparrow, E.M., A. Haji-Sheikh, and T.S. Lundgren. *Inverse problem in transient heat conduction*. 1964: American Society of Mechanical Engineers (ASME), New York, NY, United States.

45. Trujillo, D.M., *Application of dynamic programming to the general inverse problem.* International Journal for Numerical Methods in Engineering, 1978. **12**(4): p. 613-24.

46. Beck, J.V., B. Blackwell, and A. Haji-Sheikh, *Comparison of some inverse heat conduction methods using experimental data.* International Journal of Heat and Mass Transfer, 1996. **39**(17): p. 3649-3657.

47. Yeih, W.K., T.; Mura, T. , *An inverse problem in elasticity with partially over-prescribed boundary conditions, Part I: Theoretical approach.* Journal of Applied Mechanics, Transactions ASME, 1993. **60**: p. 595-600.

48. Yeih, W.K., T.; Mura, T., *An inverse problem in elasticity with partially over-prescribed boundary conditions, part II: Numerical details.* Journal of Applied Mechanics, Transactions ASME, 1993. **60**.

49. Ru-Min, C., C. Yen-Ji, and F.C. Lin, *Determining the unknown traction of a cracked elastic body using the inverse technique with the dual boundary element method*. Computer Modeling in Engineering & Sciences, 2001. **2**(1): p. 73-85.

50. Huang, C.H., M.N. Ozisik, and B. Sawaf, *Conjugate gradient method for determining unknown contact conductance during metal casting.* International Journal of Heat and Mass Transfer, 1992. **35**(7): p. 1779-86.

51. Lin, Z.-C. and C.-k. Chen, *Inverse calculation of the friction coefficient for upsetting a cylindrical mild steel by the experimental load.* Journal of Materials Processing Technology, 2006. **178**(1-3): p. 297-306.

52. J. Yvonnet, D.U., F. Chinesta, F. Micari, *A simple inverse procedure to determine heat flux on the tool in orthogonal cutting.* International Journal of Machine Tools and Manufacture, 2005.

53. Merchant, M.E., *Mechanics of the metal cutting process. II. Plasticity conditions in orthogonal cutting.* Journal of Applied Physics, 1945. **16**: p. 318-324.

54. Oxley, P.L.B., *The mechanics of machining : an analytical approach to assessing machinability.* 1989, New York: E. Horwood; Halsted Press. 242 p.

55. Fang, N., I.S. Jawahir, and P.L.B. Oxley, *Universal slip-line model with non-unique solutions for machining with curled chip formation and a restricted contact tool.* International Journal of Mechanical Sciences, 2001. **43**(2): p. 557-580.

56. Waldorf, D.J., R.E. DeVor, and S.G. Kapoor, *Slip-line field for ploughing during orthogonal cutting.* Journal of Manufacturing Science and Engineering, Transactions of the ASME, 1998. **120**(4): p. 693-698.

57. Johnson, G.R. and W.H. Cook, *Fracture Characteristics of Three Metals Subjected to Various Strains, Strains Rates, Temperatures and Pressures.* Engineering Fracture Mechanics, 1985. **21**(1): p. 31-48.

58. Wang, Z.G., et al., *A hybrid cutting force model for high-speed milling of titanium alloys.* CIRP Annals - Manufacturing Technology, 2005. **54**(1): p. 71-74.

59. Adibi-Sedeh, A.H., V. Madhavan, and B. Bahr, *Extension of Oxley's Analysis of Machining to Use Different Material Models.* Journal of Manufacturing Science and Engineering, 2003. **125**(4): p. 656-666.

60. Albrecht, P., *New developments in theory of metal-cutting process -- 1. Ploughing process in metal cutting.* American Society of Mechanical Engineers -- Transactions -- Journal of Engineering for Industry Series B, 1960. **82**(4): p. 348-358.

61. Basuray, P.K., B.K. Misra, G.K. Lal, *Transition from Ploughing to Cutting During Machining with Blunt Tools.* Wear, 1977. **43**: p. 341-349.

62. Arsecularatne, J.A., *On tool-chip interface stress distributions, ploughing force and size effect in machining.* International Journal of Machine Tools & Manufacture, 1997. **37**(7): p. 885-899.

63. Manjunathaiah, J. and W.J. Endres, *A New Model and Analysis of Orthogonal Machining With an Edge-Radiused Tool.* Journal of Manufacturing Science and Engineering, 2000. **122**(3): p. 384-390.

64. Ren, H. and Y. Altintas, *Mechanics of Machining with Chamfered Tools.* Journal of Manufacturing Science and Engineering, 2000. **122**: p. 650-659.

65. Schimmel, R.J., W.J. Endres, and R. Stevenson, *Application of an Internally Consistent Material Model to Determine the Effect of Tool Edge Geometry in Orthogonal Machining.* Journal of Manufacturing Science and Engineering, 2002. **124**(3): p. 536-543.

66. Waldorf, D.J. *A simplified model for ploughing forces in turning*. 2004. Charlotte, NC, United States: Society of Manufacturing Engineers, Dearborn, 48121-0930, United States.

67. Palmer, W.B. and R.C.K. Yeo. *Metal Flow Near the Tool Point During Orthgonal Cutting with a Blunt Tool*. in *Advances in Machine Tool Design and Research 4th International M.T.D.R. Conference*. 1963. The Manchester College of Science & Technology.

68. Zhang, H.T., P.D. Liu, and R.S. Hu, *A three-zone model and solution of shear angle in orthogonal machining.* Wear, 1991. **143**(1): p. 29-43.

69. Abdel Moneim, M.E., *Tool edge roundness in finish machining at high cutting speeds.* Wear, 1980. **58**(1): p. 173-192.

70. Dewhurst, P. and I.F. Collins, *Matrix Technique for Constructing Slip-Line Field Solutions to a Class of Plane Strain Plasticity Problems.* 1973. **7**(3): p. 357-378.

71. Manjunathaiah, J., *Analysis and a new model for the orthogonal machining process in the presence of edge-radiused (non-sharp) tools*, in *Mechanical Engineering*. 1998, University of Michigan: United States -- Michigan.

72. Kragel'skii, I.V. and S.L. Rybalov, *Temperature dependence of specific wear for sliding of rubber (resin) on metals.* Doklady Akademii Nauk SSSR, 1965. **164**(5): p. 1035-1036.

73. Venkatesh, V.C. and R. Ramaswami, *Secondary Shear Zone and the Negative Wedge on H.S.S. Tools.* 1970. **18**(3): p. 513-19.

74. Jaeger, J.C., *Moving sources of heat and temperature at sliding contacts.* Royal Society of New South Wales -- Journal and Proceedings, 1942. **76**(Part 3): p. 203-224.

75. Komanduri, R. and Z.B. Hou, *Thermal modeling of the metal cutting process Part I - temperature rise distribution due to shear plane heat source.* International Journal of Mechanical Sciences, 2000. **42**(9): p. 1715-1752.

76. Komanduri, R. and Z.B. Hou, *Analysis of heat partition and temperature distribution in sliding systems.* Wear, 2001. **250-251**(PART 2): p. 925-938.

77. Trigger, K.J. and B.T. Chao, *Analytical evaluation of metal-cutting temperatures.* American Society of Mechanical Engineers -- Transactions, 1951. **73**(1): p. 57-60.

78. Huang, Y., *Predictive modeling of tool wear rate with application to CBN hard turning*, in *George W. Woodruff School of Mechanical Engineering*. 2002, Georgia Institute of Technology: Atlanta, GA. p. xxxii, 213 leaves.

79. Sekhon, G.S. and J.L. Chenot, *Numerical simulation of continuous chip formation during non-steady orthogonal cutting.* Engineering Computations (Swansea, Wales), 1993. **10**(1): p. 31-48.

80. Johnson, K.L., *Contact Mechanics*. 1985: Cambridge [Cambridgeshire]; New York: Cambridge, Univerisity Press, 1985. 452.

81. Smith, J.O., Liu C.K., *Stresses due to tangential and normal loads on an elastic solid with applications to some contact stress problems.* ASME Journal of Applied Mechanics, 1953: p. 157-165.

82. Khan, A.H., S., *Continuum theory of plasticity.* 1995, New York: Wiley.

83. McDowell, D.L., *Approximate algorithm for elastic-plastic two-dimensional rolling/sliding contact.* Wear, 1997. **211**(2): p. 237-246.

84. Jiang, Y. and H. Sehitoglu, *Analytical approach to elastic-plastic stress analysis of rolling contact.* Journal of Tribology, Transactions of the ASME, 1994. **116**(3): p. 577-587.

85. McDowell, D.L. and G.J. Moyar, *Effects of non-linear kinematic hardening on plastic deformation and residual stresses in rolling line contact.* Wear, 1991. **144**(1-2): p. 19-37.

86. McDowell, D.L., Moyar, G.J. *A more realistic model of nonlinear material response: appilcation to elastic-plastic rolling contact*. in *Proceedings of the 2nd International Symposium on Contact Mechancis and Wear of Rail/Wheel Systems.* 1986. Kingston, RI.

87. Boothroyd, G.K., A. Winston, *Fundamentals of machining and machine tools*. Third ed. 2006: Taylor & Francis. 573.

88. Kalpakjian, S., *Manufacturing processes for engineering materials*. 3rd ed. Vol. 1. 1928, Menlo Park, Calif: Addison-Wesley. 950.

89. M'Saoubi, R., et al., *Residual stress analysis in orthogonal machining of standard and resulfurized AISI 316L steels.* Journal of Materials Processing Technology, 1999. **96**(1-3): p. 225-233.